RICE UNIVERSITY

Plasmonic Manipulation of Light for Sensing and Photovoltaic Applications

by

Heidar Sobhani Khakestar

A THESIS SUBMITTED
IN PARTIAL FULFILLMENT OF THE
REQUIREMENTS FOR THE DEGREE

DOCTOR OF PHILOSOPHY

APPROVED, THESIS COMMITTEE

Peter Nordlander, Chair
Professor of Physics and Astronomy;
Professor of Electrical and Computer Engineering

Naomi J. Halas
Stanley C. Moore Professor of Electrical and Computer Engineering;
Professor of Biomedical Engineering, Chemistry, Physics and Astronomy

Jason H. Hafner
Associate Professor of Chemistry
Associate Professor of Physics and Astronomy

HOUSTON, TEXAS
May, 2012

ABSTRACT

Plasmonic Manipulation of Light for Sensing and Photovoltaic Applications

by

Heidar Sobhani Khakestar

Plasmonics is a successful new field of science and technology that exploits the exclusive optical properties of metallic nanostructures to manipulate and concentrate light at nano-meter length scales. When light hits the surface of gold or silver nanoparticles it can excite collective oscillations of the conduction electrons called surface plasmons. This surface plasmon undergoes two damping processes; it can decay into photon and reemit the plasmon energy as scattered energy or decay into electron-hole pair with the excitation energy equal to the energy of the plasmon resonance, known as absorption. This high energy electron subsequently undergoes into the carrier multiplication and eventually scatters into the electrons with lower energy. We used Finite-Difference Time-Domain (FDTD) and Finite-Element Method (Comsol) to design nanoscale structures to act as nanoantenna for light harvesting and consequently manipulating radiative and absorption properties of them for Sensing and Photovoltaic applications.

To manipulate near and far field we designed our structures in a way that the bright and dark plasmon modes overlap and couple to each other. This process is called Fano resonance and introduces a transparency window in the far-field spectra. At the same time it increases the near-field enhancement. We applied the changes in near-field and far-field to SERS (Surface Enhanced Raman Spectroscopy) and LSPR (Localized

Surface plasmon Resonance) shift for sensing purposes. We modeled Fano resonances with classical harmonic oscillator and reproduced the same feature with a simple equation of motion. We used this model to replicate scattering spectra from different geometries and explain the cathodoluminescence results obtained from nanoscale gold clusters structure. All of these nanoantenna optical properties and applications are due to the reemission ability of the plasmon energy to the vacuum and confining optical field, but the plasmon energy can decay into a high energy carrier rather than radiation.

Photons coupled into metallic nanoantenna excite resonant plasmons, which can decay into energetic, hot electrons injected over a potential barrier at the nanoantenna-semiconductor interface, resulting in a photocurrent. We design a device which the range of its potential applications is extremely diverse. As silicon based detector capable of detecting sub-band gap photons, this device could be used in photovoltaic devices to harvest solar energy. Plasmon generated hot electrons can be used in photocatalytic dissociation of H2 molecules at the room temperature as well. The hot electrons in their higher energy states can populate the antibonding orbital of H2 molecules adsorbed on the metal surface and thus trigger the H2 molecule dissociation. The goal is to demonstrate the high efficiency of metallic photocatalytic systems by detecting the formation of HD molecules from the individual dissociation of two isotopes, H2 and D2.

At the end we introduce lightning rod effect in metallic nanostructures and investigated the relation between the geometry properties of micrometer rod antennas and the electromagnetic field enhancement induced due to the lightning rod effect. At long wavelength, metals behave like perfect equipotential conductors and all the field enhancement results from the drop of potentials across the junctions between individual

nanoparticles. This phenomenon is called lightning rod effect. By designing proper geometry we were able to utilize this effect to obtain enough electromagnetic enhancements in MIR region of spectrum to observe SEIRA signals from few hemoglobin molecules. Our simulation shows that the field enhancement obtained from this antenna does not depend sensitively on wavelength which is another advantage for SEIRA spectroscopy. We offered an analytical model to explore the coupling between the hemoglobin molecules and the Efield. We used this model to study the location effect of the molecule on the reflection signal. This technique allows us to detect the vibrational mode of molecules such as Hemoglobin in the real time and study their changes when the molecules are exposed to different environmental circumstances.

Acknowledgments

I would like to express my gratitude to all of those who have helped and inspired me during my five year doctoral study. My utmost thankfulness goes to my advisor, Prof. Peter Nordlander for his patient guidance and selfless encouragement in my research and study at Rice University. His exceptional intuition in physics and persistent desire for high quality research has motivated all his advisees, including me. I would like to thank my thesis committee, Prof. Naomi Halas and Prof. Jason Hafner for taking their precious time attending my thesis defense. My thanks also go to my previous and current lab mates, Dr. Chizuko Dutta, Dr. Manvir Singh, Dr. Daniel Brandl, Dr. Fei Le, Dr. Taeho Park, Dr. Yanpeng Wu, Dr. Tamer Ali, Dr. Jorge Zuloaga, Dr. Kui Bao, Mr. Vikram Kulkarni, Mr. Yang Li, Mr. Yumin Wang, Mr. Yourong Zhen, Dr. Ke Zhao, Dr. Nicolas Large, Mr. Yang Cao, Miss. Lifei Liu and Mr. Britain Willingham for the valuable discussions. The Laboratory of Nanophotonics (LANP) also deserves great thanks from me. This cross disciplinary platform has greatly helped me in broadening my horizon and deepening my understandings in the field. Especially I would like to thank Prof. Naomi Halas group, Mr. Mark Knight, Mr. Britt Lassiter, Mr. Shaunak Murkherjee, Mr. Jared Day, Oara Neumann, Miss Lisa Brown, Mrs. Surbhi Lale, and Mr. Jian Ye for the pleasant and fruitful collaboration. In addition, I want to thank my other collaborators, Prof. Stefan Maier, and Prof. Rainer Hillenbrand for the pleasant cooperation and discussions. My deepest gratitude goes to my family for their unflagging love and support throughout my life, especially my wife, Michelle, whose fully support enables me to complete the work.

In the last, I would like to thank all the funding agencies. This work is supported by the National Science Foundation Major Research Instrumentation (MRI) Grant ECCS-1040478, the Defense Threat Reduction Agency (DTRA) HDTRA1-11-1-0040, the National Security Science and Engineering Faculty Fellowship (NSSEFF) N00244-09-1-0067, the Air Force Office of Scientific Research, and the Robert A. Welch Foundation under Grants C-1220 and C-1222.

Contents

List of Figures

List of Tables

List of Equations

Nomenclature

CNP	Carbon Nano Particle
CRDC	Concentric Ring/Disk Cavities
DM	Drude Model
EBID	Electron Beam Induced Deposition
EF	Electromagnetic Field
FD	Fermi Dirac
FDTD	Finite Difference Time Domain
FEM	Finite Element Method
FOM	Figure of Merit
FR	Fano Resonance
FTIR	Fourier Transform Infrared Spectroscopy
FWHM	Full Width Half Maximum
HO	Harmonic Oscillator
IR	Infrared
LDOS	Local Density of States
LSPR	Local Surface Plasmon Resonance
MEG	Multi Exciton Generation
MIM	Metal-Insulator-Metal
MIR	Mid-Infrared
MNP	Metal Nano Particle
NIR	Near-Infrared

SEIRA	Surface Enhanced Infrared Absorption spectroscopy
SEM	Scanning Electron Microscope
SERS	Surface Enhanced Raman Spectroscopy
SES	Surface Enhanced Spectroscopy
SFC	Surface Femto Chemistry
SNOM	Scanning Near-field Optical Microscopy
SPASER	Surface Plasmon Amplification by Simulated Emission
STEM	Scanning Tunneling Electron Microscope
TDLDA	Time Dependent Local Density Approximation

Chapter 1

Introduction

Plasmons are a quasi-particle description of the collective oscillations of free electron density in metals. In free electron jellium model, the plasmon is oscillating in a frequency determined by the electron density n_0, which is also known as the bulk plasmon frequency $\omega_B = \sqrt{4\pi n_0 e^2/m_e}$ [1]. Surface Plasmons (SPs) are those confined at the interfaces between metals and dielectrics or vacuum, which normally oscillate in a lower frequency. For an infinite planar surface, the SP frequency is $\omega_s = {}^{\omega_B}/_{\sqrt{2}}$. In 1957, Ritchie theoretically examined the energy loss of fast electrons passing through a thin metallic film [2], where he predicted the existence of SPs, which is proved later by Powell and Swan's experiments [3-4].

In addition of using the fast electrons, illuminating metallic nanostructure with external light can be used to excite the surface plasmons. At the resonance frequency of the SPs associated to the structure, the electromagnetic waves of light will be strongly

scattered and absorbed by the metallic structure. By varying the size and geometry of the nanostructure, the plasmon resonances are highly tunable in a wide spectrum from visible light regime to the middle infrared regime. This high tenability of localized plasmon resonances in small metallic nanostructures have attracted large interest in the scientific community for over a century, because of their strong interaction with visible light [5-6]. Noble metal nanoparticles possess a range of interesting optical properties due to localized electromagnetic resonances, known as surface plasmons. The dependence of nanoparticle plasmon resonances on geometry and local dielectric environment [7-8] has led to a variety of strategies for the systematic design of optical properties into nanoparticles and nanostructures. Initially, studies focused mainly on colloidal particles but more recently, along with the development of the field of Plasmonics, more insight and control has been gained on localized plasmon resonances in well-controlled structures fabricated using top-down nanotechnology [9-10].

It is well-known that the electromagnetic field in the vicinity of a nanoparticle is confined and enhanced at the plasmon resonance due to the surface plasmon polaritons (SPPs). This confinement electromagnetic field led to a number of important advances towards the goal of Nanophotonics infrastructure for confining and guiding electromagnetic radiation such as creation of metal nanoparticle plasmon waveguide and using plasmon to increase the sensitivity of various spectroscopic techniques, such as Raman scattering or infrared absorption spectroscopy [11-13]. Moreover, the scattering and absorption cross sections of nanoparticles are enhanced at the plasmon resonance, which can be used to increase the efficiency of solar cells[14], or possibly cure cancer utilizing thermal effects[15]. As the spectral position of the plasmon resonance depends

on the refractive index of the medium surrounding the nanoparticle, plasmonic structures can also be utilized as highly integrated optical sensors[16].

All the above-mentioned applications use the fact that the plasmon resonance depends directly on the morphology and size of the nanoparticle. Various geometries have been proposed and fabricated to match the requirements of the application, ranging from spheres[17-18], rods [18] or rings[19-20] to more complex structures such as nanoeggs or nanostars[21-22]. Control over the spectral position of the plasmon resonance in such single nanostructures is generally very good. However, control over the line shape of the resonance has not yet received as much attention, although many applications would benefit from for example nanostructures with sharp plasmon resonances – i.e. a higher quality factor. For instance, Sherry and coworkers have introduced the concept of a figure of merit (FOM) to characterize the sensitivity of a plasmonic sensor [23]: this FOM is inversely proportional to the width of the resonance. Another example is the "(lasing) Spaser"[24]: the production of a coherent output of surface plasmons or photons in plasmonic nanocavities, which will also require a high quality factor.

The main decay channels contributing to the line width of a plasmon resonance are: non-radiative decay of the coherent electron oscillations in internal channels (inter-/intra-band transitions of the electrons, interaction with phonons etc...) in which resonant plasmons decay into energetic, "hot" electrons, and radiative decay which is known as scattering as well [25-26]. For small particles (diameter$< \lambda_{res}$), non-radiative processes are dominating [18, 26]. For larger particles (diameter$> \lambda_{res}$), radiative damping dominates [27]. One of the important properties of optical antennas is their propensity for

generating energetic or "hot" electron-hole pairs by plasmon decay [28-29]. Light not redirected by the antenna is absorbed, forming an energetic electron-hole pair. This process is an additional contribution to plasmon damping, broadening the intrinsic linewidth, and is typically considered deleterious to antenna performance. This process of hot electron generation has been shown to participate in photochemical reactions at noble metal nanoparticle surfaces [30-31], but it has remained largely unexploited in solid-state devices.

The other important property of optical antenna is their radiative damping. To manipulate the radiative damping, one can exploit the concept of plasmon hybridization [32] to study coherent coupling between closely spaced nanostructures. For example, it has been predicted theoretically that concentric ring/disk cavities (CRDC) will exhibit sub and superradiant modes due to hybridization of the fundamental dipolar modes of the two constituents[33] and that Fano resonances can arise due to the interaction with higher order modes, when the structural symmetry is broken[34]. Coherent effects in plasmonic nanocavities and particularly Fano resonances have recently received a large amount of attention [34-43]. The Fano resonance can evolve into a classical analogue of electromagnetically induced transparency (EIT) when the energy levels of the interacting resonances coincide [41, 44-45].

In Chapter 2, we focused on the coupling between sub and superradiant plasmonic modes, which induce Fano resonances, in different structures such as gold/silica/gold multilayer particles called Fanoshell, different arrangements of gold clusters such as heptamer and nanomer, and ring/disk cavity. Using darkfield spectroscopy of single structure here at Rice University, Naomi Halas graduate students Britt Lassiter, Shaunak

Mukherjee and Lisa Brown demonstrate that destructive coupling between sub and super-radiant modes induce strong transparency windows in the scattering spectra [46-49]. We start this chapter with a brief introduction to the Fano resonances and thereafter introduce the experimental attempts to map the electromagnetic field at the Fano resonance. In this chapter it has been demonstrated that the enhanced electromagnetic field induced due to the high density of surface plasmon polaritons at the fano resonance can be used to increase Raman Spectroscopy signal for PMMA molecule and carbon dots. This is a strong confirmation of our argument about the application of Fano resonance for Raman spectroscopy and single molecule detection. In addition to what has been said, this strong field enhancement and the narrow line width of fano resonance made this spectral feature an excellent candidate for Local Surface Plasmon Resonance (LSPR) shift since it is strongly sensitive to the environment dielectric. We are going to demonstrate two geometries that have been used for this purpose. And at the end of this chapter we are going to conclude our discussion about the fano resonance by discussing about the application potential of this scattering phenomenon.

In 2002 Alzar developed a simple harmonic oscillator model to imitate the Electromagnetically Induced Transparency (EIT) in populated medium which are usually taken place in vapors of three-level atoms. Their model involves only two oscillators with linear coupling. Chapter 3 gives an introduction to this modeling method and how it can be used in the plasmonic field to simulate Fano resonances and to extract their coupling parameters which can be a new tool to measure and compare the quality of different Fano effect. Moreover, to improve spring model we introduce scattering term which represent the radiative damping and coupling between hybridized plasmons and it has been shown

that this model can be used to recreate Fano resonances in different plasmonic structures and give us a good counterintuitive insight that can help us to understand this phenomenon. Further, this model has been applied to cathodoluminescence measurements and examining the selection rules for plasmon excitation in the context of a coupled oscillator picture, we provide an intuitive explanation of this behavior based on the plasmon modes observed for optical and electron-beam excitation in the cluster nanostructures. Using nanoantennas to manipulate the illumination light is not just explicit to the scattering properties of the metallic nanostructures; absorption cross section of these antennas represents the efficiency of the hot electron production due to the plasmon decay in these metallic nanoscale devices.

Plasmon resonance of metallic nanoparticle decays to the photons as scattering cross section or it decays into the hot electron as absorption cross section with a lifetime of 1-20 fs [50]. Chapter 4 has been dedicated to the hot carrier production in the metallic particles at the plasmon resonance energy due to the plasmon decay, which is a boson, to electron-hole pair. The excited electron undergoes carrier multiplication through electron-electron scattering processes such as Auger transitions and result in a distribution of many lower energy electrons. Eventually the lower energy electrons interact with phonons and return to the Fermi level energy with the decay rate of about 1-4 ps. However via introducing a barrier to separate these high energy carriers from the Fermi level electrons it is possible to harvest these high energy electrons [51]. This active optical antenna can be used to detect the photons well below the band gap of the semiconductor at room temperature. Although using a barrier is a legitimate idea to collect the high energy electron produced by plasmon decay, but it is not the only method

to harvest them. Hot electron generated at the plasmon frequency can be used to derive catalytic reaction between H_2 and D_2 in the gas state to produce 2HD at room temperature. These examples shows how we can use nanoantenna to harvest the energy packages of light and produce current or start chemical reaction.

Chemists found plasmonics interesting because of its prosperous applications in sensing. As plasmons are resonating with incoming electromagnetic waves, the localized charges on metal surface will dramatically enhance the electric field nearby. The amplitude of E field can be amplified more than 100-fold in some cases, which makes them efficient platforms for Surface-Enhanced Spectroscopies (SES), such as Surface Enhanced Raman Spectroscopy (SERS), where the electromagnetic enhancement factor is proportional to the fourth power of the field incident on the molecule [52-54]. Recently there has been a resurgence of interest in another type of SES, surface enhanced infrared absorption (SEIRA) [13, 55-58]. Even though the signal in SEIRA is only proportional to the square of the electromagnetic field, SEIRA is likely to play an increasingly important role in the field of chemical and biological sensing since it probes dipole-active vibrational modes in infrared range, providing a complementary analysis of molecules orbital where is out of SERS detection. One primary reason why SEIRA has received so much less attention than SERS has been the limitations in designing and fabricating nanostructures with tunable plasmons across the broad infrared (IR) region of the spectrum utilized in this spectroscopy.

In Chapter 5 we design and initiate an alternative way to reach the high electromagnetic field enhancement in the IR range that we need to do SEIRA for single molecule via introducing lightening rod effect in the gold nanoantennas. This occurs

when metals act as perfect conductors and expel the electric field from the interior of the metals into the vacuum. This high focused E field is the results of using two long rods with a small gap between them to compress the E field along the rods into the gap. We show that how this effect can be applied to the hemoglobin molecules and detect their vibrational modes and we conclude our discussion with some theoretical models at the end. A brief chapter at the end of this thesis overviews through the goals, the achievements and further works in Plasmonics field.

Chapter 2

Fano Resonance

2.1. Introduction to the Fano Resonance

Complex plasmonic nanostructures can serve as model systems for a variety of fascinating coherent phenomena arising from the physics of coupled oscillators. Symmetry breaking provides a crucial mechanism for enhancing the coupling of plasmon modes, allowing modes that only couple weakly to the radiation continuum to couple directly to incident electromagnetic radiation [21]. Recently, subradiant modes and higher order resonances have attracted significant attention, particularly in the context of generating plasmon modes with reduced radiative damping, which might facilitate the

development of plasmonic nanolasers [24, 59]. These concepts have been recently exploited for creating Metamaterials with high-quality-factor resonances [36-37, 60].

In structures with broken symmetry, Fano resonances can arise due to the interaction of narrow dark modes with broad bright modes. This phenomenon has been theoretically investigated for a variety of structures ranging from particle lattices and split-ring type structures to nanowire arrays and particle dimers [13, 37, 60-61]. Nonconcentric ring/disk cavities have been identified as a system with a highly tunable Fano resonance, exceptionally large refractive index sensitivity, and localized surface plasmon resonance figure of merit [34, 41, 62]. Using numerical electromagnetic simulations, Zhang and coworkers have shown that for a strongly coupled system with near-degenerate levels consisting of a side-by-side arrangement of a slab dimer and a slab monomer, the asymmetric Fano line shape can evolve into a full plasmonic-induced optical transparency for optimized geometries [44]. This constitutes a classical analogue [63-64] to the well-known phenomenon of electromagnetically induced transparency (EIT) of atomic physics. In plasmonics, plasmon-induced transparency over a short-range of frequencies has great potential for the design of low-loss Metamaterials and subwavelength waveguides with low radiative losses.

2.1.1. Fanoshells

A simple multilayered plasmonic nanoparticle consisting of an Au nano-crystalline core, a silica spacer layer, and a metallic shell, has recently been fabricated and analyzed within the plasmon hybridization picture [65]. The hybridized plasmonic response of this nanoparticle, originating from the coupling between the primitive dipolar Au sphere and shell plasmons, gives rise to three hybridized plasmon modes: in increasing energy, an antisymmetric bonding mode, a symmetric antibonding mode, and a nonbonding mode. The lowest energy antisymmetric bonding mode is a subradiant, dark mode, where the individual dipole moments of the Au core and the Au shell are out of phase. The higher-energy symmetric antibonding mode is a superradiant mode, where the dipole modes of the Au core and the Au shell oscillate in phase. In a recent paper [66], it was shown that for a nonconcentric alignment of the metallic core relative to the shell, higher multipolar modes may become visible in the optical spectrum due to additional interactions caused by symmetry breaking. Here we report the controlled synthesis and observation of the optical properties of such nanoparticles at the individual particle level using dark field micro-spectroscopy. The geometry of the particle is chosen so that the sub- and superradiant modes overlap in energy. The inherent asymmetry of this nanoparticle enhances the coherent coupling between the plasmon modes of different multipolar symmetry, resulting in multiple, tunable, nearly isotropic Fano resonances in the optical response. A Fano resonance caused by the interaction of the sub- and superradiant modes is present also for the symmetric (concentric) particle. The higher multipolar Fano resonances are due to symmetry breaking.

$Au/SiO_2/Au$ nanoshells were synthesized and a dark field microscope was used by a graduate student, Shaunak Murkherjee, at Professor Naomi Halas lab to obtain single particle scattering spectra from individual nanoparticles. White light was obliquely incident on the nanoparticle at an angle of 75° while the backscattered spectra from the nanoparticles were collected in a cone having a solid angle of 64° as defined by the numerical aperture of the reflection dark field objective (Zeiss, 100×, NA 0.9) used. In this geometry, s-polarized light excitation corresponds to the electric field of the incident illumination being parallel to the substrate, while for p-polarized excitation, the electric field vector of the incident light contains a mixture of parallel and perpendicular components with respect to the substrate. More information related to synthesizing, characterizing and darkfield measurement could be found in the original paper published in Nanoletter [48].

Scanning electron microscopy (SEM) images of three synthesized nanoparticles studied are shown in Figure 2.1.1A. It is quite evident that each of these individual Fanoshells (i–iii) has a distinct, asymmetric morphology obtained by the growth of SiO_2 and Au layers on a faceted Au nanoparticle core. Irregularities in SiO_2 and Au layer thicknesses, and an overall nonspherical geometry, are characteristic of this nanoparticle. These morphologies deviate from the idealized symmetric geometry comprised of perfectly concentric metal and dielectric layers (Figure 2.1.1B). In reality, the experimentally fabricated individual structures closely resemble the more realistic schematic depicted in Figure 2.1.1C, where the faceted, nano-crystalline Au core affects the morphology of the subsequent SiO_2 and Au layer growth. Furthermore, thin SiO_2 layers ($\leq$20 nm) on nanoparticle surfaces are typically non-uniform in thickness. The

intermediate SiO_2 layer of the Fanoshells is on the order of 15–20 nm and therefore likely to be somewhat nonuniform, introducing additional asymmetry into the nanoparticle. The plasmonic properties of this complex can be modeled quite accurately, however, by a much simpler structure with uniform, symmetric core and shell layers and an offset Au core (Figure 2.1.1D).

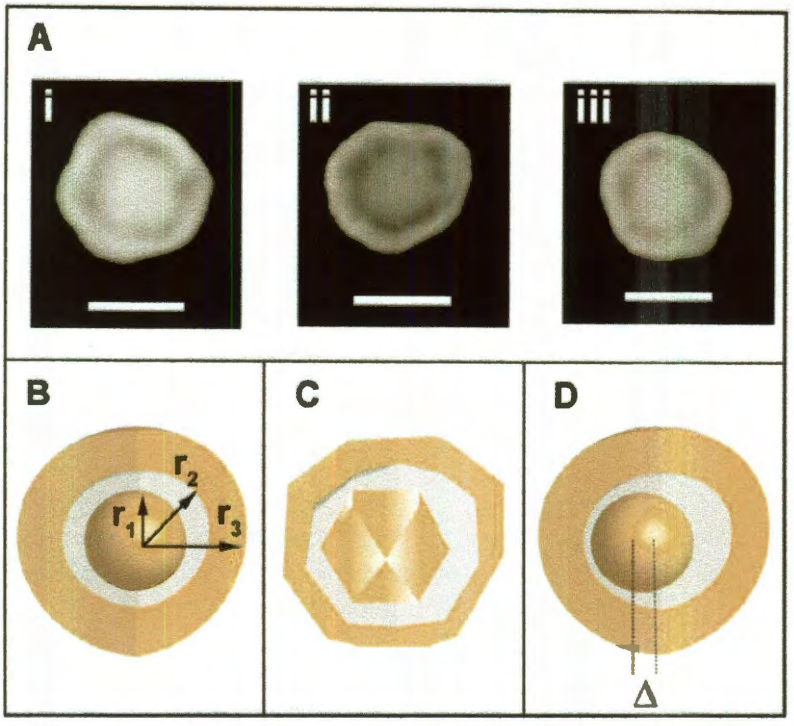

Figure 2.1.1. Au/SiO2/Au nanoparticles. (A) SEM images of three individual representative Au/SiO2/Au nanoparticles (i–iii) with overall diameters of 150 ± 25 nm on glass substrate. Scale bar = 100 nm. (B) Schematic of ideal concentric Au/SiO2/Au nanoparticle geometry, where r_1 is the core radius, r_2 is the radius of the silica coated core, and r_3 is the radius of the nanoparticle. (C) A more realistic nanoparticle schematic representing the irregular morphologies shown in (A). (D) Theoretical model of Fanoshell, where a displaced spherical nanoparticle core (by Δ nm) within a spherical core–shell nanoparticle represents the nanoparticle irregularities.

The dark field scattering spectra of the three nanoparticles (i–iii) in Figure 2.1.1A were obtained for unpolarized illumination (black), and s (green) and p (red) polarized illumination (Figure 2.1.2A–C). A very similar optical response was observed in both the s- and p-polarized cases. The optical spectrum is clearly strongly modulated, with two prominent Fano resonances occurring at nominally 650 and 800 nm, respectively. The individual nanoparticle-to-nanoparticle variations in the shape and location of these features are pronounced and clearly evident in these spectra. This sensitivity appears to be related to the size and shape inhomogeneities characteristic of this nanostructure. The Fano resonances clearly observed in the spectra of individual nanoparticles cannot be observed in the ensemble nanoparticle spectrum [65] due to the inherent averaging of the spectra from many slightly different nanoparticles. Because these irregularities arise mostly from the faceted shape of the inner Au core, it is unlikely that there is a suitable size regime for the present $Au/SiO_2/Au$ Fanoshells where this inhomogeneous broadening could be sufficiently suppressed. Single crystalline Au nanoparticles are faceted for all sizes and tend to become less spherical for larger diameters. However, the related geometry of $SiO_2/Au/SiO_2/Au$ nano-matryushkas [32, 67] is typically more homogeneous and symmetric because the nanoparticles are fabricated around a spherical SiO_2 nanoparticle core, and the intermediate SiO_2 layer is typically thicker and therefore more uniform. It is likely that such structures also support Fano resonances, which may be observable in ensemble, solution-based measurements.

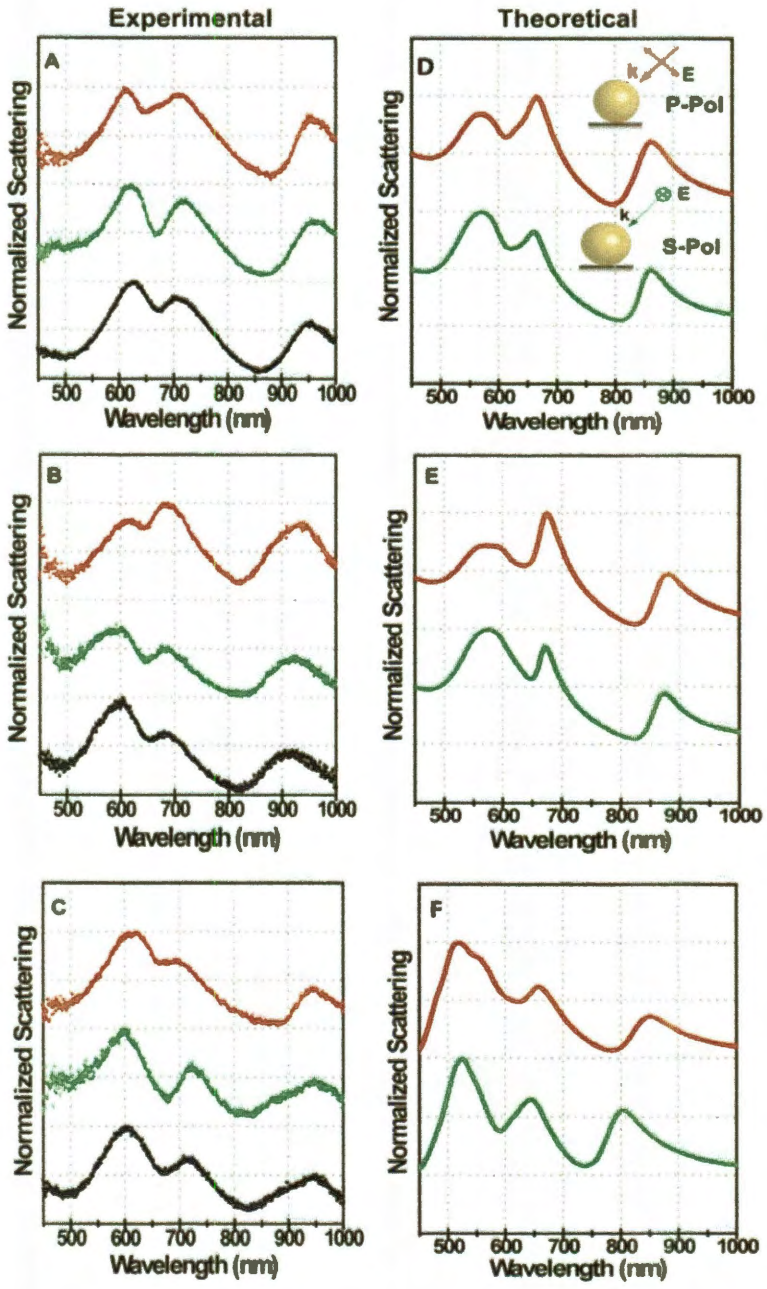

Figure 2.1.2. Experimental and theoretical spectra of Fanoshells. (A–C) Dark field scattering spectra obtained from the nanoparticles shown in Figure 2.1.1A (i–iii), respectively. (D–F) theoretical simulations of the Fanoshell spectra shown in (A–C), respectively, obtained using the FDTD method and JC dielectric data. Unpolarized (black), s-polarized (green), and p-polarized (red) spectra are shown.

Scattering spectra of individual Fanoshells were modeled using the finite-difference time-domain (FDTD) method. An empirical dielectric function (JC) for was used for Au [68]. An infinite dielectric substrate ($\varepsilon = 2.25$) was incorporated to simulate the experimental conditions as accurately as possible [69]. To obtain good agreement with the experimental geometry, the Fanoshells were modeled as slightly oblate spheroids with a major axis of 150 nm and a minor axis of 130 nm. A shell thickness of 25 nm and a core radius of 35 nm with different offsets (Δ) were used. The SiO_2 dielectric spacer layer was calculated using a dielectric of $\varepsilon = 2.25$.

The two Fano resonances can be understood as interactions between the subradiant and superradiant plasmon modes of the nanoparticle. The dipolar plasmon modes of the inner Au core and the outer Au shell hybridize, forming a lower energy narrow subradiant bonding and a higher energy broad superradiant antibonding plasmon mode that spectrally overlaps the subradiant mode. The superradiant and the subradiant mode interfere and induce a Fano resonance, which we denote as the dipole–dipole Fano resonance (900 nm) due to the dipolar nature of the two interfering modes. The dipole–dipole Fano resonance can exist in a perfectly symmetric Fanoshell because of the near field coupling between the two modes. Under reduced symmetry, the system can also support a second dipole–quadrupole Fano resonance (650 nm) because coupling between the dipolar superradiant mode and the quadrupole mode becomes allowed. We note that the Fano resonances in Figure 2.1.2 are almost isotropic and that the optical response for s and p polarization is very similar even though deposited on a dielectric substrate.

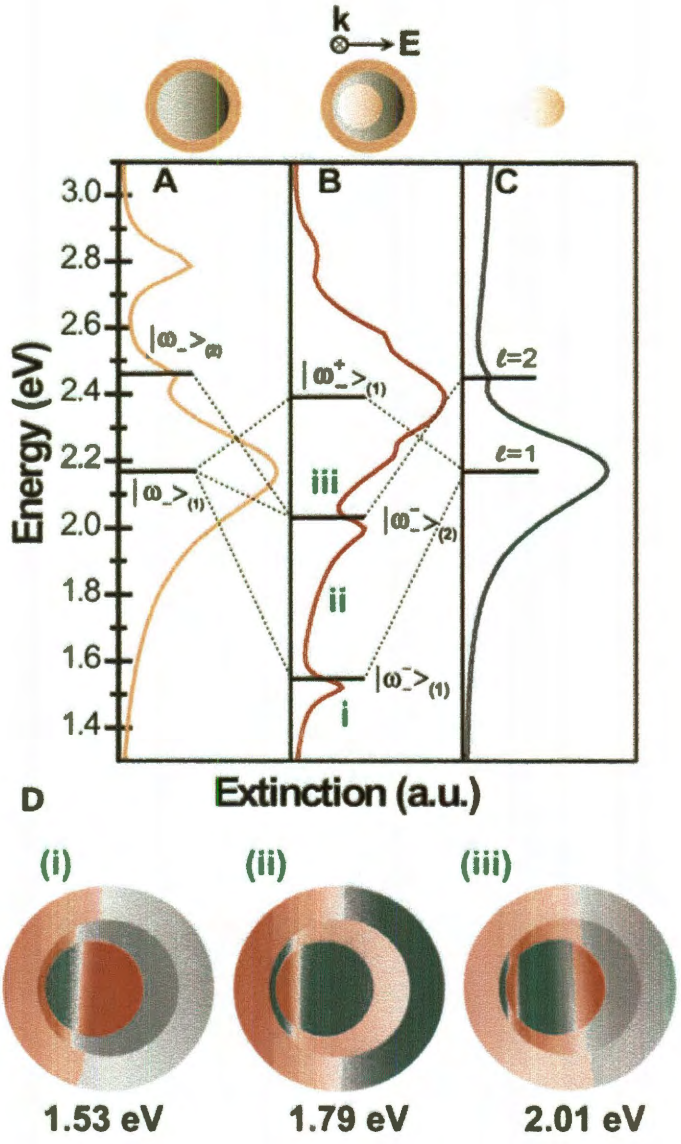

Figure 2.1.3. Energy level diagram of plasmon hybridization of Fanoshells. (A) Extinction spectrum of Au nanoshell [r1, r2] = [50, 75] nm in vacuum with SiO2 as dielectric core. (B) Fanoshell in vacuum with dimensions [r1, r2, r3] = [35, 50, 75] nm with a Δ = 10 nm offset. (C) Au nanosphere of radius 35 nm embedded in dielectric medium (ε = 2.25). All calculations were performed using the finite element method with s-polarized light excitation, a DM permittivity for Au, and a constant permittivity ε = 2.25 for SiO_2. (D) The surface charge distribution of the Fanoshell, corresponding to the (i) subradiant mode, (ii) superradiant mode, and (iii) quadrupole Fano resonances at the indicated energies.

To examine the origin of the two types of Fano resonances observed, a more detailed theoretical analysis was performed by analyzing this structure in the plasmon hybridization picture (Figure 2.1.3) [66, 70]. Theoretical simulations for the simplified geometry depicted in Figure 2.1.1D were performed using the finite element method (COMSOL Multiphysics 3.5a) for a Fanoshell of dimensions $[r_1, r_2, r_3] = [35, 50, 75]$ nm with the Au core having an offset of $\Delta = 10$ nm. In these calculations, in order to better resolve the higher energy modes, we use a Drude model permittivity (DM) for Au which neglects the damping caused by interband transitions. The plasmonic response can be understood as an interaction between primitive sphere plasmon and nanoshell plasmon modes. For a nonconcentric alignment, primitive core and shell modes of different multipolar symmetries can interact. The dipole bonding mode $|\omega_-\rangle_{(1)}$ of the shell and the primitive dipole plasmon mode ($l = 1$) of the spherical core hybridize, giving rise to a subradiant dipole bonding mode $|\omega_-^-\rangle_{(1)}$ at 1.53 eV and a superradiant dipole antibonding mode $|\omega_-^+\rangle_{(1)}$ at 2.39 eV. This superradiant mode is significantly broader than the much narrower subradiant mode. The near field coupling between the two modes gives rise to the dipole–dipole Fano resonance observed at about 1.6 eV.

The interaction between the primitive quadrupolar ($l = 2$) bonding modes of the nanoshell $|\omega_-\rangle_{(1)}$ and the Au core gives rise to a hybridized quadrupole bonding mode $|\omega_-^-\rangle_{(2)}$ in the Fanoshell. Under reduced symmetry, this narrow quadrupolar dark mode $|\omega_-^-\rangle_{(2)}$ interacts with the broad superradiant bright mode $|\omega_-^+\rangle_{(1)}$ and induces the dipole–quadrupole Fano resonance at nominally 2 eV. The excitation of the quadrupole is

due to its coupling to the dipolar mode and NOT because of phase retardation. A very weak octupole Fano resonance appears for the same reason around 2.25 eV.

Surface charge distributions for the Fanoshell at specific frequencies characteristic of the coupled modes of the nanoparticle are shown in Figure 2.1.3D. The charge profiles for (i) the subradiant mode at 1.53 eV, (ii) 1.79 eV, sufficiently detuned from both the Fano resonances to clearly show the superradiant mode, and (iii) the dipole–quadrupole Fano minimum at 2.0 eV are shown. At 2.0 eV, corresponding to the minimum in the spectrum associated with the dipole–quadrupole Fano resonance$|\omega_{-}\rangle_{(2)}$, the surface charge on the shell exhibits a dipolar pattern with a distinct separation of positive (red) and negative (blue) charge, while the core exhibits a quadrupolar pattern. This charge distribution clearly shows the mixed dipolar–quadrupolar character of the dipole–quadrupole Fano resonance. A related planar structure consisting of a disk inside a ring has been investigated in recent publications [71-72]. The hybridization diagram for these structures is similar to Figure 2.1.3 with a bonding subradiant and an antibonding superradiant hybridized mode. However, for these planar systems, the interactions are stronger and the subradiant mode is shifted sufficiently well below the superradiant continuum that the mode appears as a peak rather than as a Fano resonance. For a nonconcentric alignment of the disk and ring, a quadrupolar Fano resonance can appear for parallel polarization of incident light. In contrast, the Fanoshell exhibits an almost isotropic response with a Fano resonance which is observable for all incident polarizations.

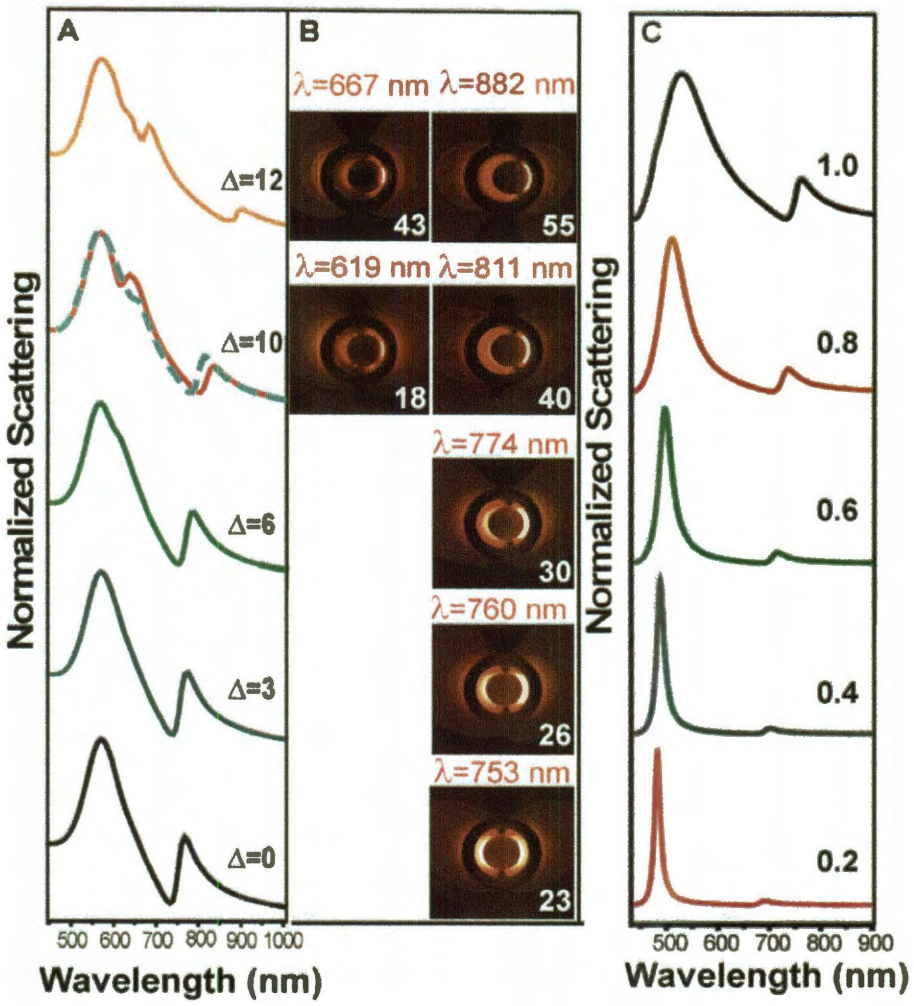

Figure 2.1.4. Dependence of Fano resonances on core offset. (A) Theoretical scattering spectra calculated by FDTD as a function of offset parameter Δ. The bottom spectrum (black) corresponds to the concentric nanoparticle geometry [r1, r2, r3] = [35, 50, 75] nm. Solid curves are for polarization parallel to the symmetry axis. The blue dashed spectrum for Δ = 10 nm is for perpendicular polarization. (B) Near field distributions at the dipole–dipole and dipole–quadrupole Fano resonance wavelengths. The numbers in white indicate the maximum electromagnetic near field enhancements. (C) Scattering spectra of concentric Fanoshells (Δ = 0) scaled to different sizes (Mie theory). The bottom spectrum corresponds to a concentric Fanoshell in the quasi-static limit, of dimensions 20% of the concentric experimental nanoparticle, i.e., [r_1, r_2, r_3] = [7, 10, 15] nm. The Au metal was modeled using the DM.

To investigate the effect of symmetry breaking on the Fano resonances, FDTD simulations were performed using a DM dielectric function initially starting with a concentric Fanoshell geometry of $[r_1, r_2, r_3]$ = [35, 50, 75] nm. Asymmetry was introduced by progressively offsetting the core with respect to the shell. The variation in the strength of the Fano resonances as a function of core offset (Δ) is shown in Figure 2.1.4A. The scattering spectrum of the concentric Fanoshell (Δ = 0) exhibits a single strong Fano resonance with a minimum around 750 nm. This is the dipole–dipole Fano resonance, due to the coupling between the subradiant mode $|\omega_-^-\rangle_{(1)}$ at 750 nm and the superradiant mode $|\omega_-^+\rangle_{(1)}$ near 580 nm. With increasing core offset, the quadrupolar mode starts to appear in the spectrum (Δ = 6). This dark quadrupolar resonance couples to the superradiant dipolar mode and induces the Fano resonance at ~650 nm. The coupling between the quadrupolar mode and higher order modes (e.g., octupole at 640 nm in the Δ = 12 nm spectrum), red shifts the quadrupolar Fano resonance with increasing offset. The lower energy Fano resonance also red shifts and decreases in intensity with increasing core offset. In Figure 2.1.4A for Δ = 10 nm, we compare the scattering spectra for two different polarizations. The curves are very similar showing the near isotropic response of individual Fanoshells.

The electromagnetic hotspots for the subradiant mode become more localized and intense with increasing offset Δ (Figure 2.1.4B). This is consistent with an increasing coupling between the subradiant mode and the higher order modes. The nonradiative nature of the subradiant mode, along with a highly confined electromagnetic near field inside the dielectric may be important in Spaser or nanolaser applications [24, 73].

To investigate retardation effects and the influence of particle size on the dipole–dipole Fano resonance, Mie theory calculations were performed starting with a quasi-static-sized concentric Fanoshell and then rescaling it to the experimental geometry of $[r_1, r_2, r_3] = [35, 50, 75]$ nm (Figure 2.1.4C). In the quasi-static limit, the superradiant peak is narrow. In this size regime it couples only very weakly with the subradiant mode, and the subradiant mode appears as a minor but distinct peak. With increasing nanoparticle size, the superradiant mode broadens due to the increased radiative damping and eventually provides a sufficient spectral overlap with the subradiant mode that a characteristic asymmetric Fano resonance is induced.

2.1.2. Plasmonic Nanoclusters

Here we examine how the coherent properties of a nanoscale plasmonic cluster are affected by cluster size, geometry, and local dielectric environment. Our study focuses primarily on the seven-member "heptamer" cluster. The plasmonic structures investigated in this section were fabricated by Britt Lassiter from Naomi Halas group via electron beam lithography and are composed of 30 nm thick Au disks on a 1 nm Ti adhesion layer, evaporated onto a Si substrate coated with a 100 nm thick silicon dioxide layer. The dielectric permittivity of the substrate is therefore similar to a typical glass substrate.

In Figure 2.1.5, we show the scattering spectra of three heptamers of increasing size. As can be seen from the SEM images of the clusters in the top panels, the dimensions of the particle radii are increased while the gap sizes are kept constant at ~15 nm (Figure 2.1.5A–C (i)). The scattering spectrum of each cluster was collected using dark-field spectroscopy (Figure 2.1.5A–C (ii)). For more information related to the experimental method you can check the paper published by Britt Lassiter, B. Lassiter et al. (2010) [46].The FRs were not as pronounced when using objectives with higher incidence angles or numerical apertures. Because these structures are not in the quasistatic limit, retardation effects are present when light is incident from large angles with respect to the substrate normal. In this case, the retardation effects allow direct excitation of the subradiant mode, effectively limiting the interference effect that causes the Fano resonance. This Fano interference effect is described below in detail.

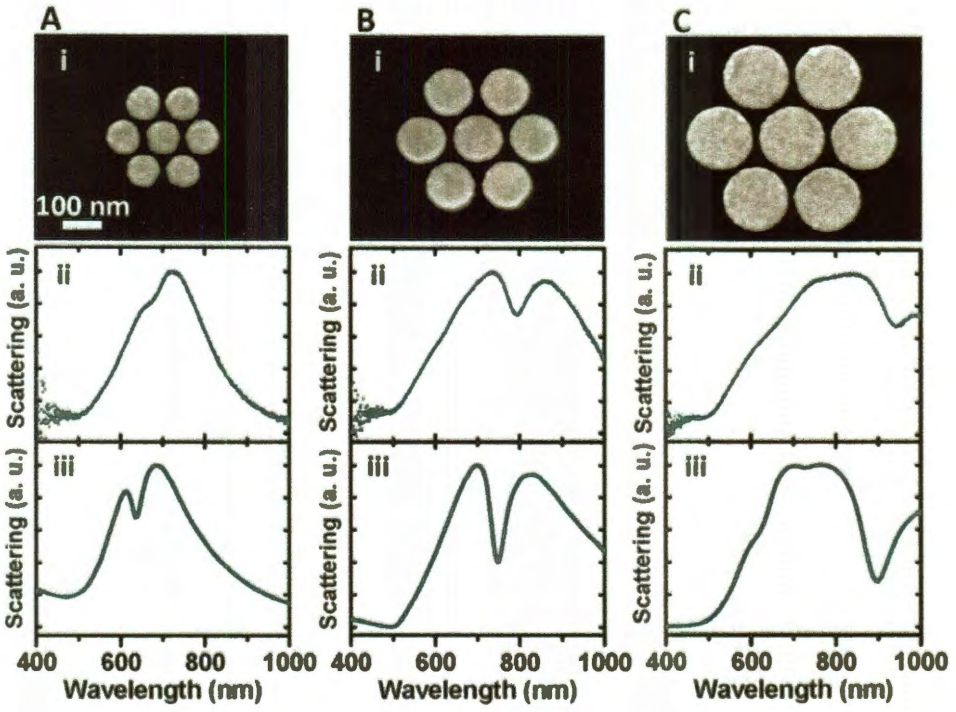

Figure 2.1.5. Size dependence of the scattering spectrum of a heptamer: (A) 85 nm diameter constituent particles; (B) 128 nm diameter particles; (C) 170 nm diameter particles. In all cases, the gap sizes between the particles in the heptamers were nominally 15 nm. (i) SEM images obtained using an FEI Quanta 400 SEM; (ii) experimentally obtained dark-field scattering spectra, obtained with unpolarized light, of each individual cluster shown in (i); (iii) FDTD calculations of the dark-field spectral response of the same structure.

Theoretical scattering spectra for these structures were obtained using the finite-difference time-domain (FDTD) method (Figure 2.1.5A–C (iii)). The dielectric function used to model Au was obtained from the experimental data of Johnson and Christy (JC) [68]. The clusters were simulated on an infinite dielectric substrate with $\varepsilon = 2.04$ to represent the experimental supporting substrate and illuminated with oblique incident light. The back scattered light in the simulation was recorded over a conical solid angle corresponding to the numerical aperture of the objective lens used in the experiment.

The optical properties of symmetric plasmonic heptamers composed of spherical and cylindrical nanoparticles have been analyzed and described in several recent publications [13, 74-75]. The symmetry group of the heptamer is D_{6h}. Using the plasmon hybridization concept, the plasmon modes can be classified according to their irreducible representations. The collective modes that can couple efficiently to light are the E_{1u} modes. The two relevant modes for Fano interference are (1) a bonding bright (superradiant) mode where the dipolar plasmons of all nanoparticles oscillate in phase and in the same direction, and (2) an antibonding dark (subradiant) mode, where the dipolar moment of the center particle opposes the dipole moment of the surrounding ring. In the quasistatic, non-retarded limit, the dark mode possesses nearly no net dipole moment and does not easily couple to light. In the retarded limit, the bright mode becomes superradiant, while the dark mode remains subradiant. Also in this limit, the weak coupling mediated by the plasmonic near-field introduces an interaction between the sub- and superradiant modes, inducing a FR in the superradiant continuum at the energy of the subradiant mode. Because of its D_{6h} symmetry, the optical properties of the cluster, including its FR, are isotropic that is independent of the orientation of the in-plane polarization of light incident on the structure.

Figure 2.1.5 shows the evolution of the scattering spectrum of a heptamer as the cluster is scaled up from the near-quasistatic to the fully retarded limit. The Fano minimum is strongly dispersive toward lower energies with increasing cluster size, and the Fano line shape becomes broadened. The smallest heptamer (A) exhibits a relatively narrow plasmon resonance near 700 nm, which is the bright superradiant bonding E_{1u} mode. Since the overall structure size is small, this mode does not radiate strongly

and is quite narrow. A very weak FR appears in the theoretical spectrum and appears only as a weak modulation (at nominally 690 nm) in the experimental spectrum of the cluster. For the intermediate size heptamer in (B), the bright mode is red shifted to approximately 750 nm and significantly broadened due to the increased radiation damping. The FR at 750 nm is now very pronounced. For the largest heptamer (C), the superradiant mode shifts to nominally 900 nm and is dramatically broadened. A strong FR is induced at 900 nm. For a heptamer this large, the subradiant mode radiates slightly, resulting in a slight broadening of the line width of the FR. Interestingly, the subradiant mode appears to redshift slightly more strongly than the superradiant mode with increasing size of the heptamers. This effect likely occurs because the antibonding subradiant mode contains a significant admixture of higher order modes, while the superradiant is mostly dipolar in nature. Since the gap size is kept constant, larger diameter disks result in stronger plasmonic interactions between the individual disks and consequently stronger hybridization. Because of this stronger hybridization of the higher order modes, the subradiant mode redshifts more than the superradiant mode for increasing heptamer size in the present size range.

In Figure 2.1.6, an example of the effect of symmetry breaking on the optical spectrum of the heptamer is shown. One of the peripheral particles of a heptamer is removed, resulting in an incomplete ring of nanostructures surrounding the center particle. The optical response of this reduced symmetry structure is no longer isotropic. To study the polarization dependence of the spectral response of this cluster, a rotating analyzer (Zeiss) is inserted in the collection optics of the microscope. Thus, the nanoparticle is still excited using unpolarized light, but the scattered light is polarized just

before collection. In Figure 2.1.6 (B, C), we show the measured and calculated scattering spectra for different polarization collection angles. As for the case of the isotropic, complete heptamer, the spectrum is characterized by a broad superradiant mode centered around 700 nm. However, with reduced symmetry the Fano interference displays a more complex behavior. For horizontal polarization (blue), a clear FR appears at 700 nm, and for vertical polarization (red), it appears at 740 nm. For other polarizations, the scattering spectra exhibit a mixture of these two resonances.

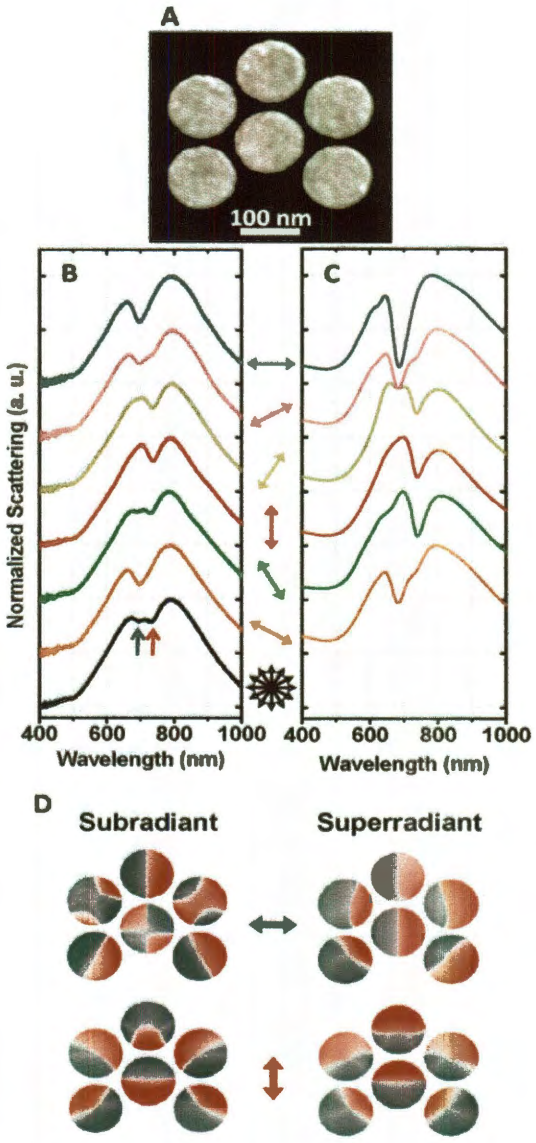

Figure 2.1.6. Asymmetric heptamers. (A) SEM image of heptamer. The disk diameters are 128 nm with 15 nm gaps. (B) Experimental dark-field scattering spectra of the asymmetric heptamer, obtained with unpolarized incident and polarization-analyzed scattered light. Colored arrows show the polarization angle with respect to the particle, as in the SEM image. Polarized spectra were collected at 30° angular increments. The black curve is unpolarized data. (C) FDTD simulations corresponding to the experimental spectra in (B). (D) Charge plots calculated using FEM for the subradiant (left) and superradiant (right) modes for the two fundamental polarizations of the structure depicted by the arrows.

A calculation of the induced charge densities of this reduced-symmetry cluster reveals the microscopic origin of the unusual split-FR observable in this structure (Figure 2.1.6D). These calculations were performed using a commercial (COMSOL) implementation of the Finite Element Method (FEM). For both polarizations, the subradiant charge plots were calculated at the wavelength of the Fano minimum (Figure 2.1.6D, left) and the superradiant charge plots were obtained for the maximum at the long-wavelength side of the Fano dip (Figure 2.1.6D, right). The superradiant charge plots clearly show that the dipolar components of all constituent particles are oriented in the same direction, resulting in the enhanced radiative damping and resultant broadening characteristic of superradiant modes. For the subradiant modes, however, the charge plots are distinctly different. For horizontal polarization, the subradiant mode has a strong admixture of nanoparticle quadrupoles. This hybridization is caused by the absence of a symmetry axis along the polarization vector. For vertical polarization, the subradiant mode is mostly a dipolar mode with the in-phase dipolar contribution of the two center particles opposing the dipole moment of the surrounding four particles, similar to the case of the fully symmetric heptamer.

Fano resonances can be realized in other symmetric clusters consisting of a center particle surrounded by a ring of particles. The reason for the very pronounced FR in the heptamer (Figure 2.1.5) is the almost perfect cancellation of the total dipole moment of the ring of particles and the (out-of-phase) center particle in the subradiant mode. For a larger ring, such as the homo-octamer shown in Figure 2.1.7A (i), the dipole moment of the ring will become larger than that of the center particle. For such a structure, the antibonding mode will have a finite dipole moment and couple efficiently to incident

light. The conditions for a FR are thus not satisfied. Neither the experimental nor the calculated spectra in Figure 2.1.7A show a pronounced FR. However, by making the diameter of the center particle larger, its dipole moment increases. For a sufficiently large center particle, its dipole moment can become equal to that of the surrounding ring. For such a hetero-octamer consisting of particles of different sizes, the antibonding mode becomes subradiant, and a strong FR with a very deep minimum, approaching transparency, is induced around 800 nm as shown in Figure 2.1.7B.

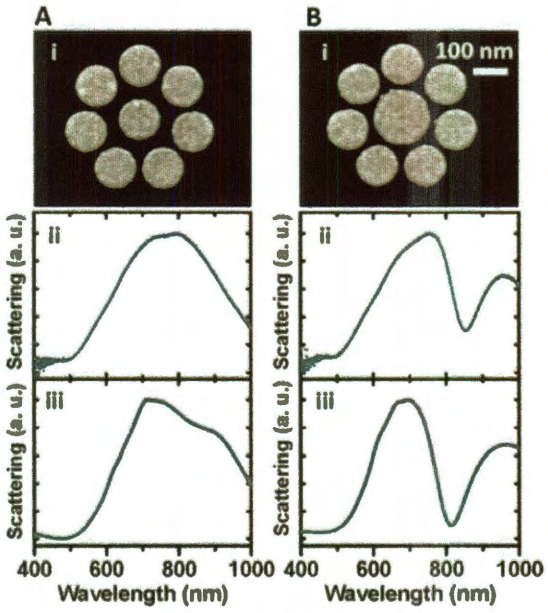

Figure 2.1.7. Scattering spectra of octamers. (A) Homo-octamer SEM image (i), dark-field scattering spectrum (ii) and FDTD simulation (iii). All particles have the same diameter =128 nm. This results in a gap of 15 nm between the outer particles and a gap of 40 nm between the inner particle and outer ring. (B) Hetero-octamer SEM image (i), dark-field scattering spectrum (ii), and FDTD simulation (iii). Here, the inner particle was enlarged such that all gaps were the same size (~15 nm). This resulted in an inner particle diameter =175 nm and the outer particle diameter =128 nm. All fabrication and data collection procedures are the same here as for Figure 2.1.5. All data were obtained with unpolarized light.

Later on in section 2.4 we examine the important case of how local changes in dielectric environment modify the frequency of the FR of the cluster. Heptamers have been predicted to have extremely large spectral shifts of their FR induced by changes in the surrounding refractive index. We will show that, as predicted, the FR in heptamers exhibits an unusually large shift with changes in refractive index; in fact, this structure exhibits the largest localized surface plasmon resonance (LSPR) response of any known nanostructure, assessed in terms of the figure of merit (FOM) of the cluster aggregate.

2.2. Mapping the Fano Resonance

Up to now, the interpretation of the constructive and destructive Fano interferences has been based on far-field spectroscopy and calculations of the charge density distributions. Such characterization of multiresonant metamolecules is both insufficient and ambiguous because the same far-field scattering pattern can be caused by different charge distributions. For example, while destructive interference—yielding a dip in the extinction spectrum—can be directly measured in the far field, its root cause (charge redistribution between different portions of the plasmonic meta-molecules) cannot be experimentally confirmed. In this sub-chapter, we use interferometric scattering-type scanning near-field optical microscopy (s-SNOM) to experimentally verify the theoretically predicted near-field patterns in Fano-resonant metamolecules.

2.2.1. Real-Space Mapping of Fano resonance in heptamer clusters

We present near-field optical amplitude and phase images of highly symmetric heptamer structures comprised of plasmonic disks (shown in Figure 2.2.1a), which was fabricated using top-down electron beam lithography. What conceptually unites this structure is that it supports a "dark" and a "bright" resonance, which can interfere with each other producing Fano resonances in the extinction and reflection spectra. We can change the relative phase of these interfering resonances by changing the sizes of the plasmonic molecules. Our near-field optical measurements directly demonstrate that Fano interferences result in the phenomenon of *intensity toggling*: strong spatial redistribution of the high-field areas inside the metamolecules upon crossing the "dark" resonance. To date, no direct experimental evidence of interfering electromagnetic eigenmodes of plasmonic metamolecules (or their arrays constituting a metamaterial) has been presented.

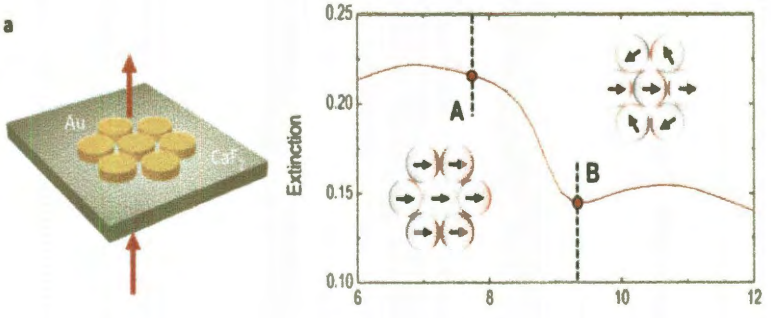

Figure 2.2.1. Fano interference in mid-infrared plasmonic metamolecules on CaF2 substarte. Calculated extinction spectrum (right) of a heptamer structure consisting of seven gold disks (left). The insets display the charge density distribution of the superradiant mode (A) and in the Fano minimum (B).

In Figure 2.2.1 we illustrate a typical Fano resonance in a heptamer structure consisting of seven gold disks of 2.70 μm in diameter on a CaF_2 substrate. Calculating the extinction spectrum of this structure, we find a resonance in the mid-infrared spectral range at about 8 μm wavelength, accompanied by a minimum at around 9.3 μm. A similar spectral behavior has been previously observed for heptamer resonances at higher frequencies, which have been fabricated using both bottom-up and top-down approaches. The calculated charge density plot at about 8 μm wavelength (position A in Figure 2.2.1) shows the surface charge density on each disk, as well as the individual electric dipole moments (black arrows), which are all oriented in the same direction. Thus, the predominantly excited eigenmode is the bright one, resulting in strong scattering and extinction (bright mode). The Fano minimum in the extinction spectrum at $\lambda = 9.3$ μm (position B in Figure 2.2.1) can be explained by the suppression of scattering caused by the destructive Fano interference between the bright and dark plasmonic eigenmodes, which minimizes the total dipole moment of the heptamer structure.

Figure 2.2.2(a) illustrates the experiment with the heptamer structures. We use a transmission-mode s-SNOM, where plane wave illumination from below the sample surface is employed. Near-field amplitude $|E_z|$ and phase φ_z imaging is performed by detecting the light scattered from the scanning probe tip with a pseudoheterodyne interferometer, simultaneously to topography (gray image in Figure 2.2.2a). We perform the experiments at a fixed incident wavelength of $\lambda = 9.3$ μm because of the limited wavelength range of the present setup. In order to observe the intensity *toggling* due to Fano interference that occurs upon crossing the "dark" resonance, we imaged heptamer structures of different sizes. As seen in the calculated extinction spectra (Figure 2.2.2b),

the Fano minimum shifts to smaller wavelengths when the radius R of the disks is reduced. We image the bright or superradiant mode for R = 1.80 μm and for R = 1.15 μm, and the Fano interference for R = 1.35 μm. For the heptamers with R = 1.80 μm and R = 1.15 μm disks, we find a typical dipole pattern on each disk. Each dipole is oriented in the same direction, oscillating with nearly the same phase, such that a strong total dipole moment is generated. For the R = 1.35 μm disks, the amplitude distribution is similar; however, the patterns on the upper and lower disks are rotated in both experiment and theory. The most significant change is observed in the phase image. The central disk still exhibits a dipolar pattern, but the fields oscillate about 90° out of phase with the outer disks, thus reducing the total dipole moment of the heptamer structure.

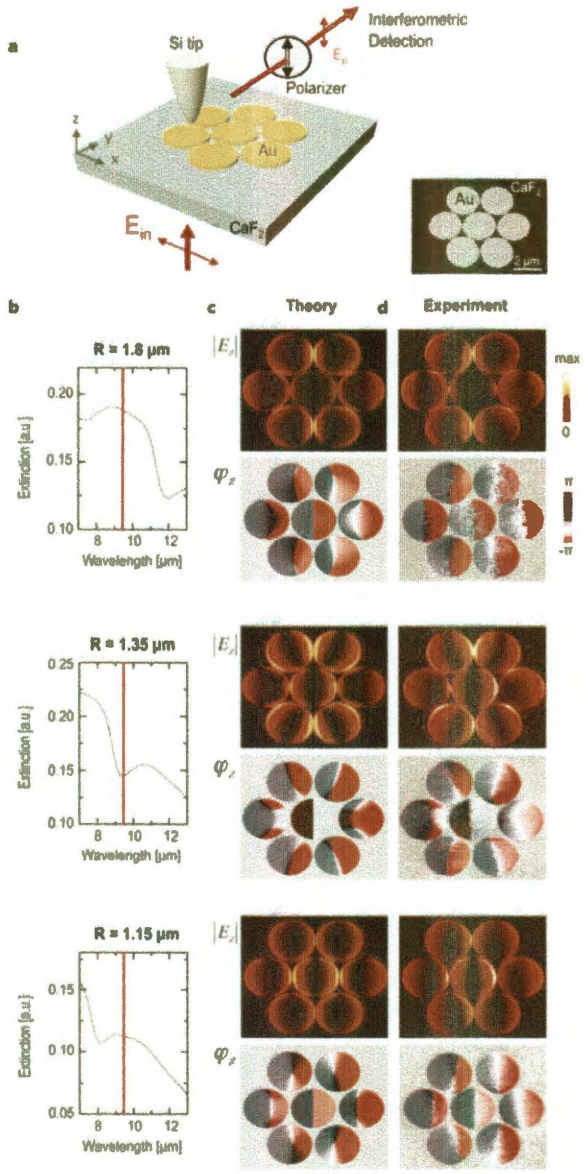

Figure 2.2.2. Real-space mapping of Fano interference in symmetric heptamer structures. (a) Experimental setup for near-field imaging in transmission mode. The heptamer structure is illuminated from below. Near-field imaging is performed by recording the tip-scattered radiation with an interferometer, yielding amplitude and phase images simultaneously to topography (gray image to the right). (b) Calculated far-field spectra for heptamer structures with different disk radius *R*. The red line marks the imaging wavelength ($\lambda = 9.3$ µm). (c and d) Calculated and experimental near-field amplitude $|E_z|$ and phase φ_z images for the differently sized heptamer structures.

Comparing the experimental results (Figure 2.2.2d) with the numerical calculations (Figure 2.2.2c), we find excellent agreement. A dramatic intensity and phase *toggling* from the outer-ring disks to the central disk is clearly observed in the experiment. An interesting observation is made when comparing the real part of the charge density distribution of the heptamer structure at the Fano dip (position B in Figure 2.2.1a) with the corresponding amplitude and phase near-field images (Figure 2.2.2b, R = 1.35 μm). In the charge density plot, the entire center row seems to be 180° out of phase with the upper and lower disks. However, the near-field phase image reveals that the central disk is phase-shifted for about only 90° relative to the upper and lower disks. This finding points out the importance of considering both amplitude and phase of the near-field or charge density distribution, in order to fully and unambiguously characterizes the oscillation state of the individual meta-atoms within complex plasmonic metamolecules.

The phase shift between the central and outer disks at the Fano dip can be explained by considering that the near-field images yield a superposition of the bright mode (all disk dipoles oscillate in phase) and the dark mode (central disk dipole oscillates out of phase with the outer disk dipoles). According to the Alzar model, which we introduce in Chapter 3 the dark and the bright modes are phase-shifted for about 90° near the Fano resonance. In the case that the dark mode is dominant—as is the case for small heptamer structures—we expect the central disk dipole being out of phase with the outer disk dipoles for about 180°. However, when the dark and the bright modes have a similar strength—as is the case for our heptamer structure—the phase shift between the central and outer disks is reduced to about 90°. Generally speaking, the phase shift between the central and outer disks can assume any value between 0° and 180° dependent on the

individual strengths of the dark and bright modes, which cannot be traced by analyzing only the real part of the charge or near-field distribution [76].

2.3. High Electromagnetic field and SERS

Fano resonances, occurring in many physical systems, are defined by their far field optical response, with its characteristic lineshape and reduced extinction cross section within a narrow spectral window. Clusters of plasmonic nanoparticles have been shown to support strong Fano resonances due to the coupling between their superradiant and subradiant plasmon modes. The Fano resonance of plasmonic nanostructures is highly sensitive to local changes in their dielectric environment, a promising property for the development of ultrasensitive nanoscale sensors. Counter intuitively, the reduced light scattering within the Fano resonance of plasmonic clusters also corresponds to intense local fields around and within the cluster. These local fields have been predicted theoretically, and have recently been imaged for plasmonic clusters with infrared Fano resonances.

Here we examine the near field properties of individual Fano resonant plasmonic clusters in detail, using surface enhanced Raman scattering (SERS), in combination with far field optical (dark field microspectroscopy) and nanoscale structural characterization (scanning electron microscopy). The strong variation of near field intensities across the finite spectral window of the Fano resonance has a direct influence on the SERS enhancements of individual clusters. Based on their geometry and resonant properties, the spatially complex near field of Fano resonant structures can be calculated using computational electromagnetic methods (performed here using the finite-difference time-domain (FDTD) method). The SERS enhancement in Equation 2.3.1 also shows a

complex spatial dependence, or a "map" of the SERS response across each plasmonic cluster.

$$EF = |\frac{E_{ex}}{E_0}|^2 \times |\frac{E_{Stokes}}{E_0}|^2$$

Equation 2.3.1.The electromagnetic SERS enhancement factor.

The SERS maps of plasmonic clusters provide a direct physical picture of the number and intensity of the local regions of high SERS enhancements, known as "hot spots", correlating well with experimentally observed SERS intensities. Variations in cluster size, interparticle spacing, and cluster geometry, all modify the near field properties in ways that can be observed directly by monitoring the SERS response. The addition of a single Raman-active carbon nanoparticle at specific locations on a plasmonic cluster distorts the spatial distribution of its near field quite effectively, depending on the specific position of the nanoparticle: this has important implications for detection of discrete analytes such as large biomolecules or viral spores. Integrating the SERS map over the surface of the cluster provides an overall relative enhancement factor for each cluster substrate that agrees well with experimental SERS measurements of a *para*-mercaptoaniline (*p*-MA) monolayer adsorbed on each structure. The spectral dependence provided by this analysis also agrees well with the relative enhancements of the two dominant Stokes modes of the adsorbate *p*-MA molecules. These observations may provide a first step toward the design of SERS substrates tailored to enhance the Stokes modes of specific molecules of interest, for tailoring the *specificity* as well as the *sensitivity* of nanoengineered SERS substrates.

2.3.1. SERS measurements of p-MA

Scanning electron microscope images of Au heptamers of three different sizes, where the individual disk diameters of fixed heights (30 nm) are increased from 85 to 170 nm while the interparticle gap distance is kept constant at ~15 nm are shown in Figure 2.1.1A. The optical properties of symmetric plasmonic heptamers have been recently studied. Interference between the bonding bright (superradiant) mode, where the dipolar plasmons of all disks oscillate in phase, and the antibonding dark (subradiant) mode, where the dipolar moment of the center particle opposes the dipole moment of the outer ring, induces a pronounced Fano dip that is highly sensitive to both cluster geometry and dielectric environment. The Fano dip can be tuned to different wavelengths by varying the size of the constituent disks.

Here we observe the same size-dependent resonance tuning, but at the individual cluster level: the larger the cluster dimensions, the further the Fano resonance is redshifted. For the smallest heptamer (i), the Fano dip is barely observable, and only a superradiant mode at 663 nm is present under horizontally polarized light (Figure 2.3.1B(i), red). For the intermediate size heptamer (ii), a pronounced Fano resonance appears at 771 nm (Figure 2.3.1B(ii), red). For the largest heptamer (iii), the Fano resonance redshifts even further to 865 nm and appears less pronounced than for the intermediate size cluster (Figure 2.3.1B (iii), red). The heptamers (i-iii) were functionalized with *p*-MA: due to the formation of a strong Au-S covalent bond between the cluster surface and the thiol group of a *p*-MA molecule, a monolayer of *p*-MA molecules self-assembles onto the heptamer surface upon functionalization. The heptamers were functionalized with a 5 mM *p*-MA ethanol solution. After

functionalization, the Fano resonance of the heptamer shows a clear redshift for all sizes (Figure 2.3.1B).

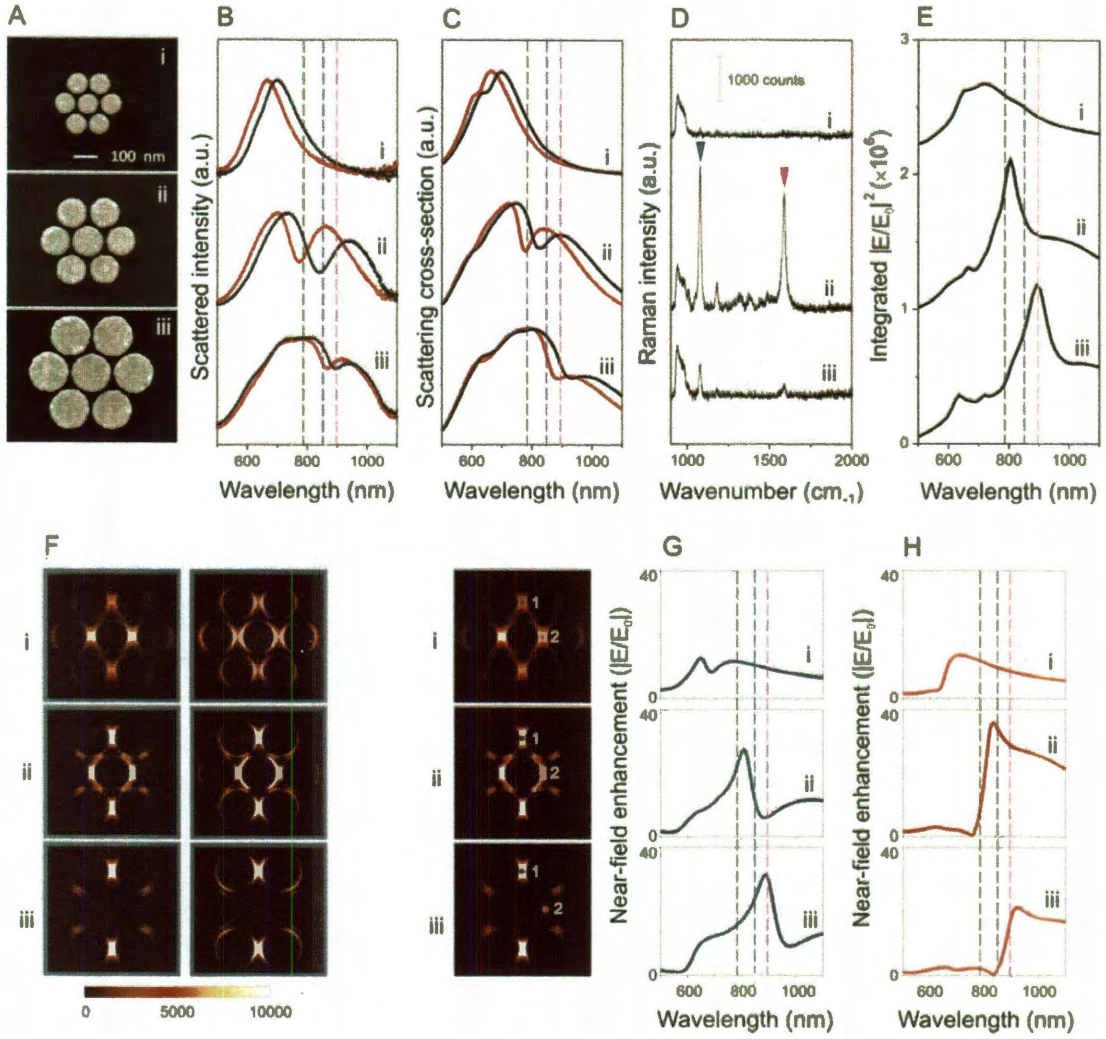

Figure 2.3.1. Far-field scattering spectra, near-field enhancement spectra and SERS properties of individual heptamers with varying sizes: (i) 85 nm diameter constituent disks; (ii) 130 nm diameter constituent disks; and (iii) 170 nm diameter constituent disks. In all structures, the height of the disks is 30 nm and the gaps between the disks are ~15 nm. (A) SEM images, (B) experimentally obtained dark-field scattering spectra, (C) FDTD calculated scattering spectra, and (D) SERS spectra of a monolayer of *p*-MA molecules for the individual heptamers (i – iii)

obtained with horizontal polarization. In (B) and (C), the scattering spectra of individual heptamers exhibit a significant redshift with chemisorption of a monolayer of *p*-MA molecules. Pristine structure (red), after *p*-MA binding (black). (E) Total near field enhancement intensity ($|E/E_0|^2$) spectra calculated by integrating over all surfaces of the heptamer. (F) Spatial distribution of the SERS enhancement ($= |E_{ex}/E_0|^2 \cdot |E_{stokes}/E_0|^2$) for the *p*-MA Stokes line at 1080 cm^{-1} for each of the individual heptamers (i – iii). Enhancement evaluated at ½ the height (left) and 2 nm above the top surface (right) of the cluster. Calculated near field enhancement ($|E/E_0|$) spectra at the hot spot (G) 1 and (H) 2 indicated on the left side of SERS maps. Dashed lines in (B, C, E, G, H) denote: the excitation laser at 785 nm (black); the Raman Stokes lines of *p*-MA at 1080 cm^{-1} (blue) and 1590 cm^{-1} (pink). These modes are indicated by the blue and pink arrows in D(ii), respectively.

It is interesting to note that the monolayer of *p*-MA molecules induces different LSPR shifts on these three different clusters: for the intermediate size heptamer with the strongest Fano resonance, a 70 nm redshift in the Fano dip is induced, due to its pronounced sensitivity to changes in dielectric medium. This large LSPR shift is quite dramatic, considering that it is induced by a molecular monolayer. It is roughly twice as large as the LSPR shifts observed for the resonance peak of cluster (i) (Figure 2.3.1B(i)) and the weak Fano dip of cluster (iii) (Figure 2.3.1B(iii)). We have performed FDTD simulations (Lumerical Solutions, Inc.) of the plasmonic response of these clusters using an empirical dielectric function for Au and for the supporting substrate. The calculated scattering spectra of the pristine heptamers show consistent agreement with the corresponding experimental spectra (Figure 2.3.1C, red). A 2 nm thick dielectric layer ($\varepsilon = 9$) on the side and top surfaces of each disk was used to model the *p*-MA monolayer. The resulting spectra agree fairly well with the experimental spectra of the *p*-MA functionalized clusters.

Surface enhanced Raman spectra of *p*-MA on the three heptamer clusters, as SERS substrates, were obtained with a 785 nm wavelength pump laser. The Raman pump laser wavelength (black) and the wavelengths corresponding to the two most prominent *p*-MA Stokes modes at 1080 cm^{-1} (blue) and 1590 cm^{-1} (pink) are shown superimposed on the spectrum of each substrate (Figure 2.3.1B,C). The different structures represent various degrees of detuning of the Fano resonance, pump laser and Stokes wavelengths: for (i), all three wavelengths are detuned from the functionalized cluster resonance, for (ii), all three wavelengths are within the Fano dip of the functionalized cluster, and for (iii), only the 1590 cm^{-1} Stokes mode is within the Fano dip of the functionalized cluster.

The effect of this detuning on the magnitude of the SERS spectrum for each cluster is shown in Figure 2.3.1D. For the intermediate size heptamer (ii), two pronounced Raman bands at 1080 and 1590 cm^{-1} are observed, which correspond to C-S and C-C vibrational modes of a1 symmetry, respectively. These two bands drop significantly for the largest size heptamer (iii) and disappear for the smaller size heptamer (i). The small broad band at 900 – 1000 cm^{-1} is from the Si substrate.

Moreover, we have calculated the total near field enhancement intensity spectrum, namely, an integration of the EF over the exposed surfaces (walls and top surfaces) of the heptamers for each wavelength in the range of 500 – 1100 nm (Figure 2.3.1. E). It is found that the Fano dip in the far-field scattering spectrum is very close to the maximum in the near field enhancement spectrum. Furthermore, it is clear from the SERS spectra of these three heptamer substrates that the strongest SERS response corresponds to the cluster substrate where the pump and Stokes wavelengths are resonant with the Fano dip. For example, although heptamer (iii) has a larger surface area, and therefore a larger

number of *p*-MA molecules bound to its surface than clusters (i) and (ii), the SERS intensities from this cluster at 1080 and 1590 cm^{-1} are nominally 5 and 8 times smaller than that of heptamer (ii).

To evaluate the SERS response of these cluster substrates, we calculate enhancement factor as mentioned in Equation 2.3.1, where E_{ex}/E_0 is the near field enhancement factor at the excitation laser wavelength and E_{Stokes}/E_0 is the near field enhancement factor at the wavelength specific to the Stokes mode of interest for the molecular analyte. The near field of a heptamer cluster has been previously reported, but here we directly evaluate the SERS enhancement factor, the product of the two local intensity distributions at two distinct wavelengths characteristic of the SERS response for a specific Stokes mode. The result is a spatial distribution of the EF over the heptamer cluster: we refer to this function of the local fields as the "SERS map" of the cluster.

The SERS maps of heptamers (i-iii) for the 1080 cm^{-1} Stokes mode of the *p*-MA molecules are shown in Figure 2.3.1F. Here we show the SERS maps calculated in two ways: with the local fields evaluated at half the height of the structures (15 nm for the 30 nm high disks) on the left, and in a plane 2 nm above the top surface of the structure (right). (Although there are slight differences between the SERS maps obtained for these two "slices", we see that the two methods of evaluation produce similar spatial distributions of SERS enhancements.) From the SERS maps we can clearly see a correlation between the strength of the observed SERS signal for each heptamer substrate, and the number and magnitude of high EF regions on each structure, commonly known as "hot spots".

For the smallest heptamer (i), two moderate-strength hot spots, located in the gaps between the central and side disk, are observed. For heptamer (ii), with the strongest SERS response, we observe hot spots in the same region as with heptamer (i), but of greater magnitude, and accompanied by two additional hot spots, again of greater magnitude, in the gaps between the top two and bottom two disks of the cluster. For heptamer (iii), the magnitude of the hot spots is similar to that of heptamer (ii) but only two hot spots, between the top two and bottom two disks, are visible. It is interesting to see how the strong local fields, characteristic of the Fano resonance of the structure, can contribute explicitly to the SERS response in such a systematic manner.

Furthermore, we have calculated near field enhancement ($|E/E_0|$) spectra at the position of two hot spots (labeled as 1 and 2 on the SERS maps on the left side of Fig. G and H) for heptamer (i) – (iii). It is clear to see that the near field enhancement at the hot spot is strongly dependent on the wavelength, spatial location, and geometry of the heptamer. These observations may guide us in the design of SERS substrates with hot spots at specific spatial positions. Additionally, by comparing the SERS maps evaluated mid-height and 2 nm above the structure, we see that the EF extends above the top of the heptamer and out from the edges of the cluster. This indicates that heptamer cluster substrates may be useful for detecting larger analytes such as biomolecules or biological targets, such as viral spores, viruses or bacteria.

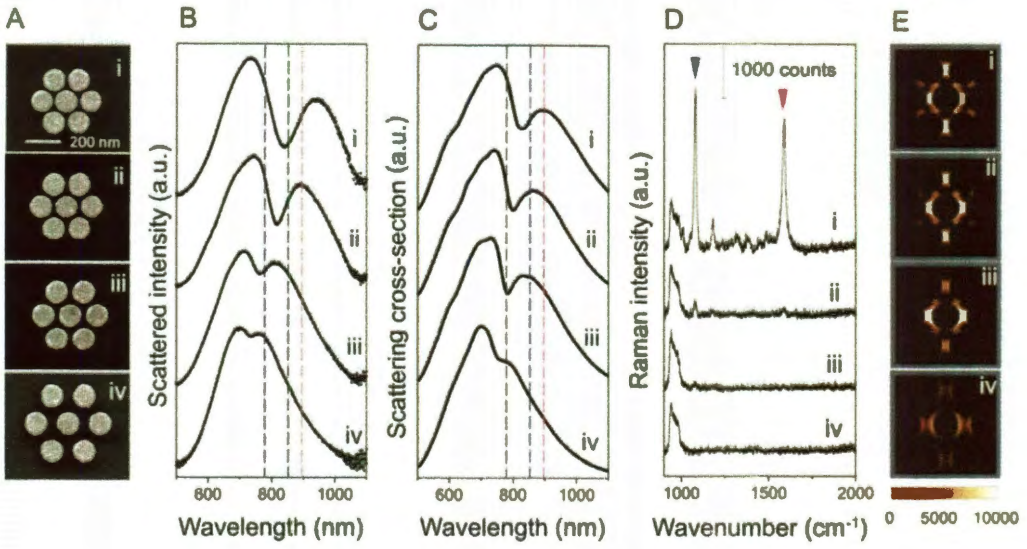

Figure 2.3.2. Scattering spectra and SERS properties of individual Au heptamers with varying gap sizes: (i) ~15 nm, (ii) ~20 nm, (iii) ~30 nm, and (iv) ~60 nm gaps. In all cases, the height of the disks is 30 nm and the diameter of the disks is 130 nm. (A) SEM image, (B) experimentally obtained dark-field scattering spectra, (C) calculated scattering spectra (FDTD), and (D) SERS spectra of a monolayer of *p*-MA molecules on individual heptamers (i – iv) with horizontal incident polarization. Black dashed lines in (B, C) show the excitation laser at 785 nm; blue and pink dashed lines show the Raman Stokes lines of *p*-MA molecules at 1080 and 1590 cm^{-1} (indicated by the blue, and pink arrows in (D)), respectively. (E) SERS maps for the 1080 cm^{-1} Stokes mode of *p*-MA on heptamers (i – iv) evaluated at ½ the height of the structure.

We also studied the effect of interparticle spacing on the scattering spectra and SERS response of a heptamer cluster (Figure 2.3.2). Figure 2.3.2A shows the SEM images of a heptamer with 130 nm diameter disks, with variations in gap size of 15 nm (i), 20 nm (ii), 30 (iii), and 60 nm (iv). Our experimental dark-field scattering spectra indicate that the Fano dip of the heptamer (functionalized with *p*-MA molecules) weakens and blueshifts when the gap size is increased, due to the decreased coupling between the superradiant and subradiant mode of the cluster (Figure 2.3.2B). The Fano

dip appearing at 841 nm for the 15 nm gap heptamer (i) is blueshifted to 733 nm when the gap size is enlarged to 60 nm (heptamer (iv)).

The spectral evolution, including the position, blueshift and weakening of the Fano resonance in the scattering spectrum with increasing gap size is reproduced in the theoretical simulation spectra, incorporating a 2 nm thick dielectric layer ($\varepsilon = 9$) for the adsorbate monolayer (Figure 2.3.2C). The corresponding Raman spectra in Figure 2.3.2D clearly show that the Stokes modes that appear at 1080 and 1590 cm^{-1} (indicated by blue and pink arrow) reach maximum intensities for the heptamer with the smallest, 15 nm gap size (i), decrease dramatically for a slightly larger 20 nm gap size (ii), and disappear almost entirely for the clusters with larger gap sizes of 30 and 60 nm (iii and iv). This nonlinear decrease of the SERS signal with increasing gap size can be understood most transparently by examining the SERS maps calculated for this series of clusters (Figure 2.3.2E). The SERS maps indicate that hot spots are located in the gaps between the central and side disk, and between the top/bottom two disks, for horizontally oriented incident polarization. When the gap size is increased, the SERS hot spots between the top/bottom two disks are the first to diminish, then the hot spots in the gaps between the central and side disk. As with variations in cluster size, variations in interparticle spacing within the cluster lead to detuning of the Fano resonance from the pump and Stokes wavelengths with a resulting decrease in SERS signal, however it is interesting to observe that this detuning, and its effect on the SERS response of the cluster substrate, is quite distinct in each case.

Four Au plasmonic oligomer clusters were fabricated; an octamer (i), nonamer (ii), decamer (iii), and undecamer (iv) (Figure 2.3.3A). As can be seen in the SEM

images in Figure 2.3.3A, the diameter of the central disk is increased while the diameter of the peripheral disks and the gap sizes are kept constant at ~85 and ~15 nm, respectively. By varying the size of the center particle with respect to the ring of peripheral particles, the depth of the Fano modulation can be increased, greatly reducing the resonant scattering cross section, and also increased in width (Figure 2.3.3B). .Simulations (FDTD) of the Fano resonances of these oligomers are in very good agreement with the experimental dark field scattering spectra (Figure 2.3.3C).

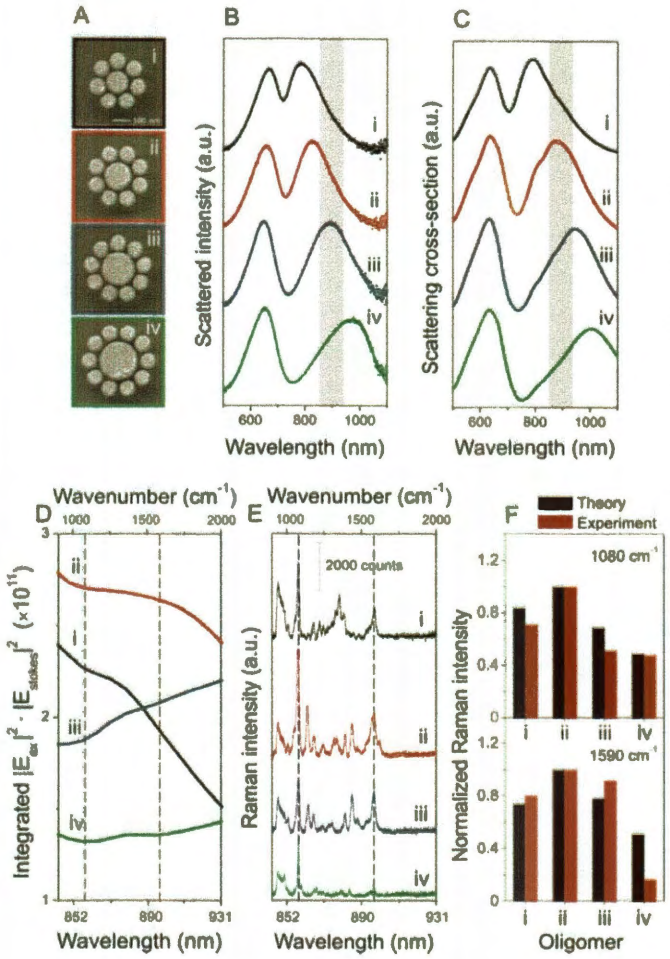

Figure 2.3.3. (A) SEM images of individual Au oligomer clusters: (i) octamer, (ii) nonamer, (iii) decamer, and (iv) undecamer. In all structures, the peripheral disks are 85 nm in diameter and all gap sizes are ~15 nm, obtained by enlarging the central disk diameter to 117 (i), 144 (ii), 178 (iii) and 208 nm (iv), respectively. (B) Experimentally obtained dark-field scattering spectra, (C) theoretical scattering spectra (FDTD), (D) calculated intensity enhancements of the Stokes lines in the range of 844 – 931 nm (indicated in the shaded regions in (B, C), corresponding to 900 – 2000 cm^{-1}) obtained by integrating the SERS maps of each structure over all surfaces, and (E) SERS spectra of a monolayer of *p*-MA molecules on individual clusters (i – iv) obtained using horizontally polarized pump light. The black dashed lines in (D, E) indicate the Stokes lines of *p*-MA molecules at 1080 and 1590 cm^{-1}, respectively. (F) Comparison of the theoretical (black) and experimental (red) normalized Raman intensity of the Stokes lines at 1080 and 1590 cm^{-1} from all oligomer clusters (i – iv).

From this theoretical model SERS maps of EF can be calculated for these structures, as in Figure 2.3.1E and Figure 2.3.2E. Here, however, we integrate the calculated EF over the exposed surfaces (walls and top surfaces) of the oligomers in the SERS map for each wavelength in the range of 844 – 931 nm. This spectral region corresponds to the 900 – 2000 cm^{-1} range in the SERS spectrum of *p*-MA, obtained with a pump laser wavelength of 785 nm. These integrated values are shown in Figure 4D, for each structure. This calculation predicts that the nonamer (ii) gives rise to the highest SERS enhancement and the undecamer (iv) yields the lowest SERS enhancement over this spectral range; the octamer (i) has a slightly lower intensity than the nonamer in the range of 900 – 1500 cm^{-1} but decreases to values lower than the decamer in the 1500 – 2000 cm^{-1} spectral range (Figure 2.3.3D).

Experimentally, we adsorb *p*-MA onto each structure and obtain a SERS spectrum (Figure 2.3.3E). In these spectra, the dashed lines indicate the two major Stokes modes of *p*-MA. The relative amplitudes of the Stokes modes in the experimental spectra obtained (Figure 2.3.3E) are then compared to the calculated values of SERS enhancement (Figure 2.3.3D) for the two major *p*-MA Stokes lines at 1080 cm^{-1} and 1590 cm^{-1}(Figure 2.3.3F). In this comparison, we see that the relative SERS enhancements for each Stokes mode correlate well with the predicted theoretical enhancements, and we also observe that the relative peak heights of the 1080 and the 1590 cm^{-1} Stokes lines, which vary depending on oligomer substrate, correlate well with our theoretical analysis.

2.3.2. Observing spatial dependence of SERS via carbon nanoparticle

Next we examine how the specific location of a discrete Raman-active analyte affects the Fano resonance of a single heptamer substrate, and how its presence modifies the SERS map of the cluster (Figure 2.3.4). The heptamer is composed of seven 120 nm diameter disks with a ~20 nm size for all gaps. In this experiment, a single carbon nanoparticle (CNP) is the Raman-active analyte, which has been demonstrated on single semishells due to the strong near field enhancement. It acts as a discrete near field probe of the cluster via SERS, where its presence also perturbs the near field properties of the cluster and its SERS response.

Figure 2.3.4A shows SEM images of a heptamer at different stages of the experiment, before and after deposition of a 25 nm size CNP on specific regions of the cluster: (i) before deposition, (ii) after deposition of the CNP in the gap between the two top disks, and (iii) following removal of the CNP from the gap shown in (ii), and after deposition of the CNP in the gap between the central and left disk (Figure 2.3.4A iii). The CNP was deposited by electron-beam-induced deposition (EBID) using a scanning electron microscope (FEI Quanta 400) operated at 30 kV with a current of 40 pA in the deposition location of choice on the nanostructure. The CNP can be effectively removed by treatment with oxygen plasma, without noticeably modifying the Au heptamer geometry or properties. A 5 min oxygen plasma cleaning process (Fishione Instruments, Model 1020) operated at 600 watts was sufficient to remove a CNP from the cluster before deposition of a subsequent CNP.

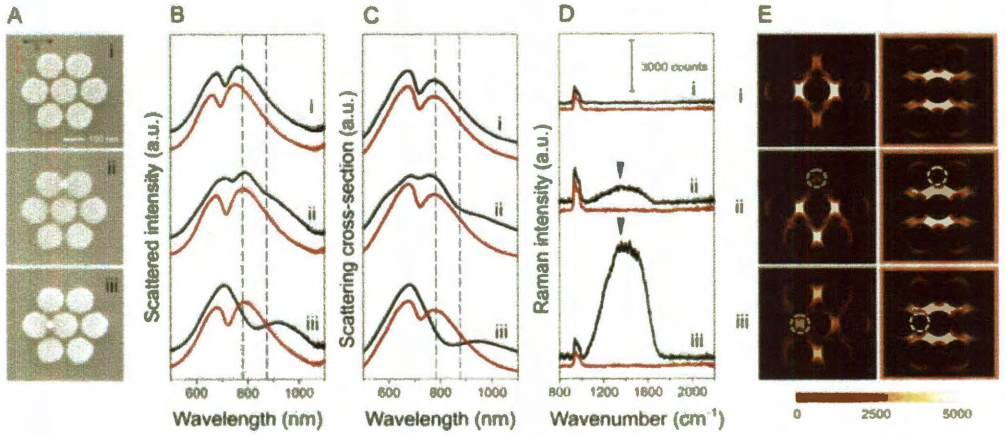

Figure 2.3.4. Spatial dependence of SERS of a single Au heptamer observed by placement of a single 25 nm diameter carbon nanoparticle (CNP) on the cluster structure. The heptamer consists of seven 120 nm diameter disks with a 30 nm height and ~20 nm gap sizes between the disks. (A) SEM images of individual Au heptamer (i) prior to CNP deposition, (ii) with a CNP placed in the gap between the two top disks, and (iii) with CNP deposited in the gap between the central and left disk. (B) Experimentally obtained dark-field scattering spectra, (C) simulated dark field scattering spectra (FDTD), and (D) SERS spectra of the CNP on the heptamer in each case with horizontal (black) or vertical (red) incident polarization. Black dashed lines in (B) and (C) show the excitation laser at 785 nm and blue dashed lines show the Raman Stokes line of the CNP at 1350 cm^{-1}, which are indicated by the blue arrows in (D). (E) SERS maps of the heptamer, corresponding to the 785 nm pump laser and the CNP Stokes mode at 1350 cm^{-1} of the single heptamer at steps i – iii for horizontally (left, black outline) or vertically (right, red outline) polarized pump light. White dashed circles in (E) indicate the corresponding locations of the CNPs in (A).

The effect of CNP placement on the dark field scattering spectrum of the pristine heptamer can be seen in Figure 2.3.4B. Prior to CNP deposition, the scattering spectrum of the pristine heptamer possesses a Fano dip located at 713 nm, when excited by horizontally polarized incident light (Figure 2.3.4B i). After deposition of the CNP in the gap between the top two disks, the Fano dip redshifts to 741 nm and weakens (Figure

2.3.4B ii). When the CNP is deposited in the gap between the central and left-side disk, the Fano dip becomes broader and redshifts further, to 838 nm (Figure 2.3.4B iii). It is surprising to observe such a dramatic (125 nm) optical shift for deposition of the CNP in different gaps of the heptamer. For vertically polarized incident light, the presence of the CNP induces only very minor shifts in the Fano resonance, from 694 to 715 to 724 nm (Figure 2.3.4B (i–iii), red curves). We can attribute this polarization-dependent response to local effects: for horizontal incident polarization, both gaps (ii) and (iii) where the CNP is placed are hot spots, while for vertical incident polarization, neither are hot spots. It is also important to note that after the heptamer in (Figure 2.3.4B ii) was cleaned by oxygen plasma, its scattering spectrum reverted to that of the original pristine heptamer prior to the first CNP deposition (not shown).

To obtain more insight into the effect of the position of the CNP and of the orientation of incident light polarization on the plasmon response, FDTD simulations were performed (Figure 2.3.4C). An empirical dielectric function for carbon was used for the dielectric function of the CNP. The calculated scattering spectra agree well with the experimental scattering spectra with respect to the overall spectral profile and the position of the Fano dip for the two polarization directions. For example, for horizontal incident polarization, the theoretical spectra show a Fano dip appearing at 717 nm without the CNP (Figure 2.3.4C i), which weakens with a rather small spectral redshift after placement of the CNP between the top two disks (Figure 2.3.4C ii). The Fano dip redshifts further, to 845 nm, after deposition of the CNP in its second location, between the central and the left disk (Figure 2.3.4C iii).

For vertical incident polarization, almost no spectral shift is observed. Such a large perturbation in the heptamer spectrum due to the placement of a CNP in the structure can be explained in the framework of the plasmon hybridization picture. For horizontally polarized incident light, the deposition of the CNP in the gap between the top two disks enhances the plasmon coupling between the top two disks, which weakens the antibonding (subradiant) mode, namely, the coupling between the collective mode of the outer ring and the central disk. This weakens the interference between the subradiant and superradiant mode. In contrast, when the CNP is in the gap between the central and left disk, it enhances the subradiant mode and consequently leads to a stronger Fano dip at a higher wavelength. When incident light is vertically polarized, the plasmon coupling between the top two disks or between the central and left disk is too weak to influence the Fano dip. However, in the FDTD simulation of this scenario for horizontal polarization, we observe that the hot spot intensity at the location of the CNP is actually slightly enhanced, corresponding to an increase in SERS signal observed. This study shows that deposition of a discrete dielectric analyte onto a plasmonic heptamer may or may not dramatically affect its far field, Fano resonant response, depending on its location on the cluster and the orientation of incident light polarization.

The SERS spectrum of the CNP deposited on the heptamer is also a strong function of where it is positioned (Figure 2.3.4D). For the pristine heptamer, no SERS modes are observed, and only a Raman signal at 938 nm, due to the Si substrate, appears in the range of 800 – 2200 cm^{-1} for both horizontal and vertical incident polarizations (Figure 2.3.4D(i)). When the CNP is deposited in the gap between the top two disks, a moderately broad SERS band at 1100 – 1700 cm^{-1} is observed for horizontal incident

polarization (Figure 2.3.4D(ii), black curve). This Raman band originates from a mixture of the D band (1100 – 1450 cm^{-1}) and G band (1450 – 1700 cm^{-1}) of amorphous carbon, originated from the breathing mode of A_{1g} symmetry and the atomic displacement of E_{2g2}, respectively. This band increases in magnitude significantly when the CNP is placed the gap between the central and left disk (Figure 2.3.4D (iii), black curve). With the CNP in this position the Raman band is increased by a factor of nominally 6.5 relative to the SERS spectrum obtained when the CNP was placed between the two top disks. In addition, no Raman bands from the CNP were observable for vertically polarized incident light (Figure 2.3.4D (i – iii), red curves).

To understand the dependence of the SERS signal on CNP position in the heptamer, we first examine the optical scattering spectrum of the cluster without, then with, the CNP (Figure 2.3.4B,C). In these spectra, both the laser excitation wavelength of 785 nm and the maximum of the D band at 1350 cm^{-1} are marked (black and blue dashed lines, respectively). Here we see that, for horizontally polarized incident light, both the pump and Stokes wavelengths are redshifted with respect to the Fano resonance for the pristine heptamer (i) and for the first position of the CNP on the structure (ii). However, for the CNP in its second location, between the leftmost and the center particle (iii), the Fano dip is redshifted, and is precisely between the laser excitation and the Stokes band. This spectral overlap between the Fano dip, pump laser and Stokes wavelength is consistent with the largest SERS signals seen earlier with *p*-MA monolayer functionalization, for both heptamer size (Figure 2.3.1) and interparticle distance (Figure 2.3.2).

The SERS maps of this pristine cluster, and with the CNP present at two specific locations, is particularly informative, providing a clear picture of the influence of the CNP on the cluster properties, and how it presence can influence the SERS response of the system (Figure 2.3.4E). The SERS maps are calculated for both horizontal (left) and vertical (right) incident pump laser polarization. The SERS map of the pristine heptamer (Figure 2.3.4E (i)), corresponding to the artificial case of a molecular adsorbate layer of ε=1 bound to the surface of the cluster, is shown for comparison with the two cases of a CNP positioned at a specific location on the cluster (Figure 2.3.4E(ii,iii)).

The SERS map of the pristine cluster reveals that, for horizontally polarized pump light, there are two strongest hot spots located in the two gaps between the central and side disks, and two moderate hot spots distributed in the gaps between the top and bottom two disks, respectively (Figure 2.3.4E (i), left). For vertical incident polarization, the hot spots appear in entirely different locations, at the gaps between the central and top, and central and bottom, disks (Figure 2.3.4E(i), right). When the CNP is deposited on the structure, we see that the spatial distributions of enhancement are altered significantly (Figure 2.3.4E (ii,iii)). When the CNP is between the two top disks, the SERS map shows a decrease in intensity at the location of the particle (white dashed circle, Figure 2.3.4E(ii) left) relative to the SERS map of the pristine cluster. In other words, *the presence of the discrete analyte reduces the SERS response at that specific location*, compared to what would have been anticipated from the SERS map of the pristine cluster.

When the CNP is deposited in the gap between the central and left disk (white dashed circle, Figure 2.3.4E(iii), left) it also reduces the SERS enhancement at that

location, although in this case the reduction is much weaker, and a stronger SERS spectrum is obtained. These observations are consistent with the relative strengths of the SERS signals measured for both CNP locations. When the SERS map is spatially integrated over the two local regions of CNP deposition for (ii) and (iii), the relative signal strength obtained is 7.1, close to the experimental relative signal intensity of 6.5. When the polarization of the incident light is vertical, neither location of the CNP corresponds to a hot spot: this is consistent with the lack of a SERS signal observed for this polarization for either CNP location on the cluster. The observation that the presence of a discrete analyte can reduce the SERS enhancement that would otherwise be anticipated from a pristine cluster substrate is an important one, and should be a prominent consideration when designing SERS substrates for the SERS detection of discrete larger size analytes.

2.4. LSPR shift sensitivity

Much of the current interest in FR at plasmonic system stems from their potential as efficient LSPR sensors [23, 77-80]. The complex interference phenomena underlying the formation of FRs in coupled plasmonic systems are highly sensitive to the dielectric environment in the junctions of the overall structure. In addition, FRs are typically very narrow, which allows for a more precise measurement of small peak shifts induced by changes in the dielectric properties of the nanostructure environment. The LSPR efficiency of a plasmonic nanoparticle is typically evaluated by its FOM, defined as the ratio of the plasmon energy shift per refractive index unit change in the surrounding medium, divided by the width of the spectral peak [23].

For asymmetric FRs, we define the energy of the resonance as the midpoint between the energy of first maximum and the energy of the minimum. The width is defined as the energy difference between those spectral features. This definition for the spectral width used to calculate the FOM has been suggested before [34] and is required because the asymmetric line shape associated with Fano resonances leads to an ill-defined full width at half-maximum (FWHM), as is usually used in the case of ordinary, or peak-like, plasmon resonances [23]. Theoretical predictions for FOM for individual plasmonic nanostructures range from 7 for coupled dipole–quadrupole antennas, 8 for nonconcentric planar ring-disk cavities, to 11 for a symmetric silver sphere heptamer. The recent experimental demonstration of a FOM of 3.8 for a coupled dipole–quadrupole antennas show the tremendous potential for FR-based LSPR sensing.

We finish this chapter by a preliminary sensing study on Concentric Ring-Disk Cavities and heptamer cluster geometry.

2.4.1. LSPR sensing in Concentric Ring/Disks

Figure 2.4.1(a) shows how the resonance of the structure with subradiant and super radiant mode as in Concentric Ring/Disk behaves in media with different refractive indices. The experiment has been conducted by creating a small "cell" with the substrate and a second glass slide, separated by optical fibres, as sketched in panel c. Water is introduced in the cell after treating the sample in an O_2 plasma cleaner (50 W, 3 min) to improve wetting of the surface, and the spectra are acquired (blue curve in Figure 2.3.4a). They are then compared with the spectra for the cell filled with air (red curves). In the experiment a red-shift of 90 ± 10 nm of the low-energy peak is observed (*i.e.*, 510 meV RIU^{-1}), which would correspond to a FOM of 1.6. Turning our attention to the corresponding simulations (Figure 2.4.1b), we observe that the expected shift should be 175 nm for a similar refractive index change (600 meV RIU^{-1}, FOM of 3, red curve to green curve). The discrepancy can be explained by the fact that most of the sensing capabilities of the cavities lie in the gap, where the water wetting is very poor. This reduces the observed shift compared to total filling. For instance, a simulation accounting for a filling of only $^3/_4$ of the gap height seems to reproduce very well the experimental shift (Figure 2.4.1b, green curve). Our approach allows for radiative loss and hence FOM engineering throughout the whole near-IR and, *via* scaling, also the mid-IR part of the spectrum, where resonances of single nanostructures show large radiative damping due to their physical size. Further optimization of cavity fabrication should allow creating structures with higher FOMs.

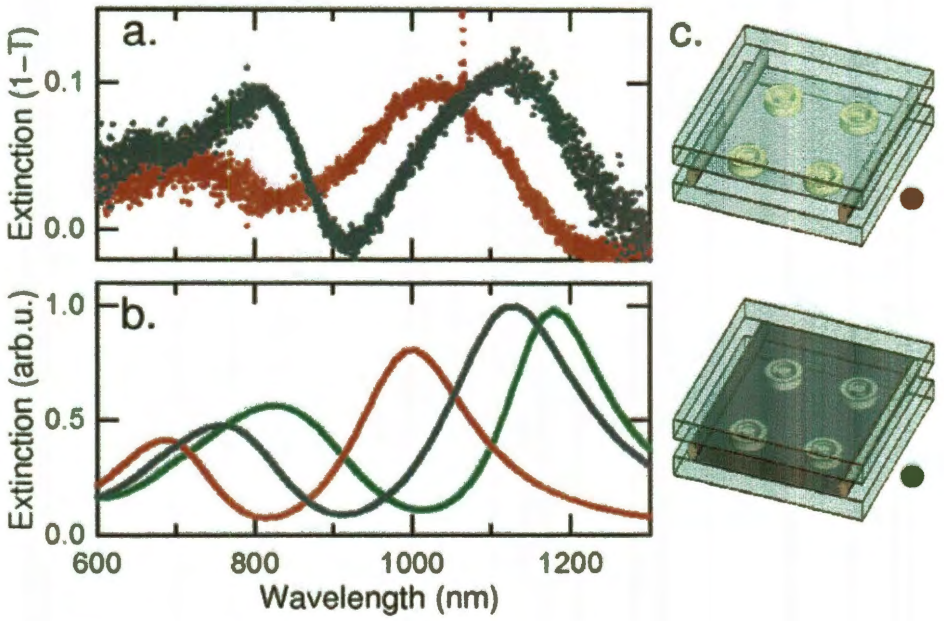

Figure 2.4.1. Sensing with a CRDC. (a) Experimental extinction spectra for the cavity (dimensions Dout = 250 nm, Din = 100 nm, and Ddisk ≈ 75 nm) in air (red) and water (blue). (b) Simulated spectra for a similar cavity (Dout = 248 nm, Din = 100 nm, and Ddisk = 88 nm). Red, in air; green, in water, with the gap completely filled; and blue, in water with $^{3}/_{4}$ of the gap filled. (c) Sketches of the sensing cell: optical fibres (diameter ≈ 200 μm) separate the sample from a capping glass coverslip.

2.4.2. LSPR sensing in heptamers

To investigate the LSPR sensitivity of the planar heptamer, we performed dark-field scattering spectroscopy on individual heptamers embedded in various dielectric media: Methanol (n = 1.326) [81], Butanol (n = 1.397) [81], index matching oil (n = 1.506, Cargille Laboratories internal documentation). For each medium, the entire substrate was first rinsed in that medium and then fully immersed in the medium in a glass-bottom Petri dish (Ted Pella). The scattering spectra were obtained from the immersed samples. Figure 2.4.2 shows a very pronounced redshift of the FR with increasing refractive index of the surrounding medium. In air ambient, the FR appears at 750 nm, and in immersion oil with a refractive index n = 1.5, the FR is shifted to 900 nm. To quantify the LSPR sensitivity, we obtain the slope of the best-fit line (linear regression with a slope =0.53) for the energy of the FR as a function of surrounding dielectric permittivity, and divide by the Fano line width (0.093 eV). The resulting FOM is 5.7, which to our knowledge is the highest LSPR FOM reported so far for an individual finite nanostructure. The FOM calculated from the theoretical simulations (Figure 2.4.2B) is slightly smaller (5.1). From this we can infer that the nanostructures were likely completely coated by each solvent medium, if this was not the case, the theoretical FOM would be larger than that obtained experimentally.

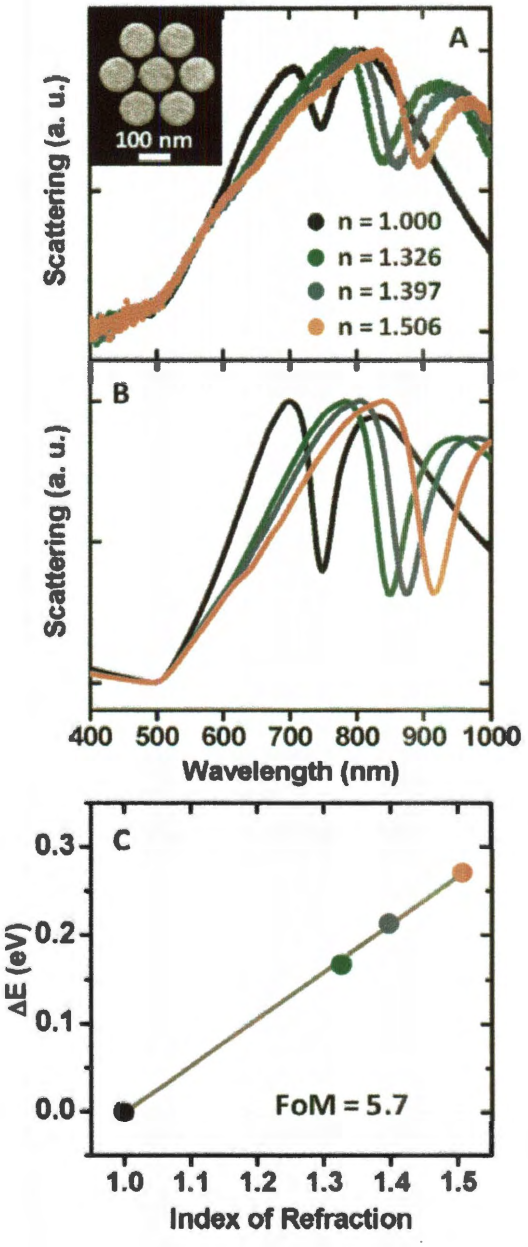

Figure 2.4.2. LSPR sensing in heptamers. (A) LSPR sensing for heptamer of same dimensions as reported in Figure 2.1.5. Four polarized scattering spectra are shown for different media (air, black), (methanol, green), (butanol, blue), (immersion oil, orange). The values for the refractive indices of each medium are shown in the figure. (B) FDTD simulations corresponding to the experiment. (C) Linear plot of the LSPR shifts of the FR vs refractive index of the embedding medium.

While this current result indicates great promise for significantly increasing LSPR sensitivities by focusing on FRs, the full potential for FR-based LSPR sensing is clearly not yet realized. In none of the structures studied in these initial experiments has the LSPR FOM been optimized. By using larger structures or structures with narrower gaps, it is highly likely that an even larger FOM can be achieved. Structures fabricated in silver instead of gold, should also yield even larger FOM than those reported here, since the lattice polarizability and electromagnetic screening of silver is significantly smaller than for gold. An advantage with lithographically fabricated clusters such as the present structure is that the energies of the FRs can be tuned very accurately by varying the ratio of the disk thickness to cluster diameter.

2.5. Conclusion

In conclusion, we have shown that plasmonic nanoparticles, Fanoshell, can be designed and synthesized with highly tunable built-in, multiple, nearly isotropic Fano resonances. Using single nanoparticle dark field spectroscopy, we observed that Fano resonances were a prominent characteristic of the optical response of these nanoparticles. The observed Fano resonances arise from two distinct origins: (1) the coupling of a subradiant and superradiant dipolar plasmon, which excites a Fano resonance even in a symmetric nanoparticle, and (2) the coupling between the superradiant dipolar and subradiant higher multipolar modes, introduced by symmetry breaking.

We have shown that lithographically fabricated nanoscale plasmonic clusters exhibit pronounced FRs, which depend strongly on both the geometry and the dielectric environment of the complex. By changing the size of a heptamer, it is possible to tune the FR to different wavelengths. By symmetry breaking, one can further tune the wavelength of the FR and induce new resonances. A very deep FR, approaching transparency can be induced in an octamer cluster consisting of a center particle surrounded by a ring of seven particles if the size of the center particle is sufficiently large. Interferometric near-field microscopy has been used to image the interference of "dark" and "bright" modes responsible for Fano resonances in plasmonic metamolecules. The results show dramatic redistributions (*toggling*) of the electric field intensity and phase across the structure as the Fano resonance is traversed and are in excellent agreement with numerical calculations. Real-space near-field imaging provides a fundamental and detailed verification of interfering plasmonic modes and their coupling and thus will be an

essential tool for the development of novel spectroscopic applications based on Fano resonances. The insights gained from near-field images will further our understanding of plasmonic Fano resonances and may open up novel applications based on the spectral manipulation of plasmonic near fields such as LSPR sensing. The FR of heptamer clusters possesses exceptional LSPR sensitivities. For a heptamer consisting of seven particles of the same size, we measure a FOM of 5.7. This unparalleled LSPR sensitivity, found in a cluster fabricated by readily available nanofabrication methods, is likely to stimulate increased interest and applications in sensing and detection based on coherent plasmonic phenomena.

We have investigated the near-field properties of Fano resonant plasmonic clusters by examining both their dark field scattering spectra and their SERS response. We have shown that the size, interparticle spacing, the presence of a dielectric particle on the cluster, and modifications in the relative size of the central and peripheral particles of a cluster all affect the Fano resonance. Since the Fano dip is also the spectral region of highest intensity near field in a plasmonic cluster, SERS is shown to be an extremely useful experimental probe of this structure and its complex near field properties. The near field is highly spatially dependent across the cluster, with several regions of large enhancement, known as hot spots, most prominent within the Fano resonance. This spatial dependence can be calculated for each cluster, yielding a specific "SERS map" of the hot spots within each structure, dependent on the Stokes modes of interest and the polarization of incident light. Experimental studies of SERS using a self-assembled monolayer of the Raman-active molecule *p*-MA show enhancements that are greatest when the pump laser and Stokes mode of interest are resonant with the Fano dip of the

structure. For the case of a discrete nanoscale Raman-active analyte, we observe that its presence on a cluster substrate can actually significantly decrease the anticipated SERS enhancement, depending on the specific location of the analyte. Integrated SERS maps yield wavelength-dependent enhancement factors for each specific cluster; comparisons between SERS data for individual clusters and these calculated values correlate very well for each cluster, and also explain changes in the relative peak heights of the two dominant Stokes modes for a *p*-MA adsorbed monolayer on each specific cluster. These studies lay the foundation for the design of new and highly sensitive nanosensor geometries whose properties may be tailored to specific analytes of interest.

Chapter 3

Harmonic Oscillator (Alzar) Model

3.1. Introduction to the Alzar model

We now turn to a more quantitative description of the Fano interference phenomenon using a spring-mass model developed by Alzar and co-workers [63]. We will model the plasmons as a simple harmonic oscillator, consisting of particle 1 with mass m_1, which represents super-radiant plasmon mode, attached to two springs with spring constants k_1 and K (see Figure 3.1.1a). The spring with constant k_1 is attached to a wall, while the other spring is attached to a second particle of mass m_2, which is connected to the third spring of constant k_2 and represent sub-radiant plasmon mode.

Particle 1 is also subject to a harmonic force $F_s = Fe^{-i(\omega_s t+\phi_s)}$, which represents the optical force on the nanoantenna. The optical response of the Fano resonances can be reproduced quite accurately with this mechanical model consisting of two coupled oscillators. The hybridized plasmon modes of the Fano resonance are modeled as two interacting of oscillators of frequency $\omega_1$as super-radiant mode and $\omega_2$as dark mode or sub-radiant mode where $\omega_i^2 = k_i/m_i$ (Figure 3.1.1). For simplicity we consider the case $m_1 = m_2 = 1$. The oscillators couple to each other through a spring $K/m = \Omega^2$.

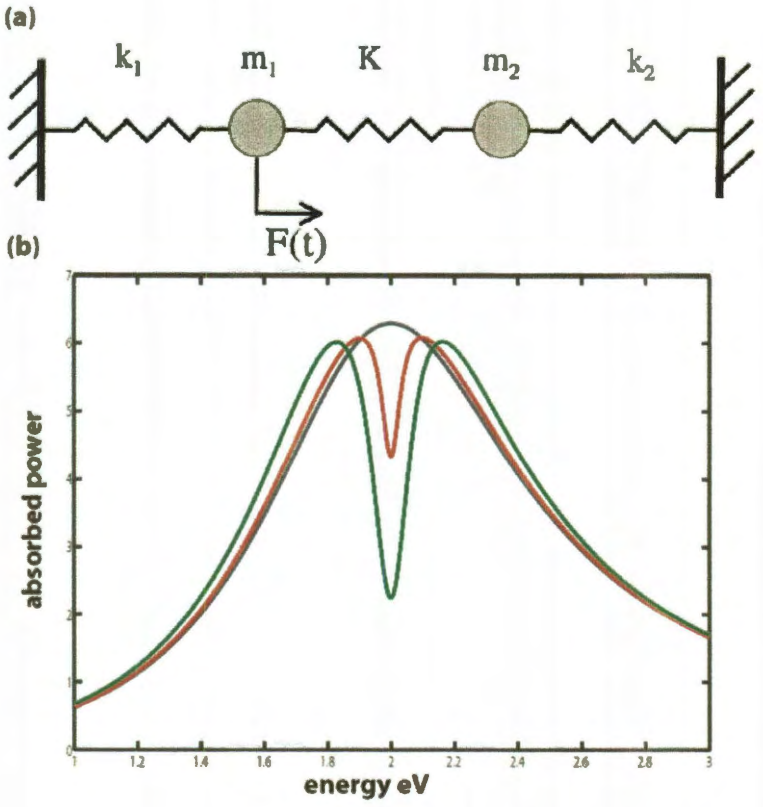

Figure 3.1.1. (a) The Basic Harmonic Oscillator model, which consist of two coupled spring and mass that are driven with a harmonic force, to simulate Plasmonic Fano resonances. (b) The real part of $P_s(\omega_s)$ for three values of the coupling frequency Ω^2 expressed in energy units, 0.0, 0.3 and 0.6 eV for blue, red and green respectively.

To provide a quantitative description of the system, we write the equations of motion of particles 1 and 2 in terms of the displacements x_1 and x_2 from their respective equilibrium positions:

$$\ddot{x}_1(t) + \gamma_1\dot{x}_1(t) + \omega^2 x_1(t) - \Omega^2 x_2(t) = \frac{F}{m}e^{-i\omega_s t},$$

$$\ddot{x}_2(t) + \gamma_2\dot{x}_2(t) + \omega^2 x_2(t) - \Omega^2 x_1(t) = 0.$$

Equation 3.1.1. Equation of motion for Harmonic Oscillator model used to simulate Plasmonics Fano resonances.

We have set $\phi_s = 0$ for the optical force without loss of generality. We also let $\Omega^2 = K/m$, the frequency associated with the coherent coupling between the bright mode oscillator and the oscillator modeling the dark mode; γ_1 is the friction constant associated with the energy dissipation acting on particle 1(which simulates the absorption damping from the plasmonic dipole mode); and γ_2 is the energy dissipation rate of the dark mode.

Because we are interested in the power absorbed by particle 1 from the optical force, we seek a solution for $x_1(t)$. By solving the equation of motion, which mentioned above (Equation 3.1.1), and computing the mechanical power absorbed during one period of oscillation of the optical force, we get the power as:

$$P_s(\omega_s) = -\frac{2\pi i F^2 \omega_s(\omega^2 - \omega_s^2 - i\gamma_2\omega_s)}{m[(\omega^2 - \omega_s^2 - i\gamma_1\omega_s)(\omega^2 - \omega_s^2 - i\gamma_2\omega_s) - \Omega^4]}.$$

Equation 3.1.2. Absorbed power during one period of the optical force oscillation.

In Figure 3.1.1b we show the real part of $P_s(\omega_s)$ for three values of the coupling frequency Ω^2 expressed in energy units, 0.0, 0.3 and 0.6 eV for blue, red and green respectively. These curves were obtained using the values $\gamma_1 = 1.0\ eV$, $\gamma_2 = 0.05\ eV$, and $\omega_1 = \omega_2 = \sqrt{K/m} = 2.0\ eV$. The amplitude F/m was equal to 1 force per mass units. For $\Omega = 0.0$, blue curve, we have a typical absorption profile, with a maximum dipole power absorption for ω. If we increase Ω to 0.3, we observe the appearance of a narrow dip in the absorption profile of $P_s(\omega_s)$. The low absorption at the center frequency of the profile is a result of destructive interference between the normal modes of oscillation of the system. A further increase of the coupling frequency leads to the appearance of more pronounce Fano deep in the probe power absorption profile, which has a clear Fano line-shape for $\Omega^2 = 0.6$.

It is important to mention that the dissipation rate γ_2, associated with the absorption damping of dark mode oscillator, must be much smaller than γ_1 in order to drive particle 1's oscillation coherently. In other words, dark mode should have narrow bandwidth and should not have significant damping rate. For the case of Fano resonance, the condition analogous to $\gamma_2 \ll \gamma_1$ is that the bright mode radiate back and is a strongly radiative mode due to the dipole nature of the mode and is highly damped, however the dark mode doesn't radiate and is dominated by dissipation damping. Therefore scattering properties of different modes and radiative coupling is the nature of the Fano resonance and it is important to use different coefficients for the scattering and absorption damping. In the following subchapters we will include the scattering term to our equation of motion and improve our harmonic oscillator model.

3.2. Scattering Extension of Alzar model

Even though basic Alzar model has a great potential to model the destructive and constructive coupling between plasmons in the nanoantennas but it doesn't differentiate between scattering and absorption coefficient in metallic plasmons. In this subchapter we improve this model by introducing scattering term to the equation of motion and make a distinction between the dissipated and radiated energy. By using Larmor power formula and writing down the equation of motion for charged particle of mass m and charge e acted on by an external force F_{ext}we can identify the radiative reaction force as $m\gamma_r\ddot{v}$ where v is the velocity of charge and is equal to $\dot{x}$ therefore we can use $F_{rad} = m\gamma_r\ddot{x}$ as radiative force. By importing the radiative force to the Equation 3.1.1 we can rewrite the equation of motion as follows:

$$\ddot{x}_1(t) + \gamma_1\dot{x}_1(t) - \gamma_{r1}\dddot{x}_1 + \omega^2 x_1(t) - \Omega^2 x_2(t) = \frac{F}{m}e^{-i\omega_s t},$$

$$\ddot{x}_2(t) + \gamma_2\dot{x}_2(t) - \gamma_{r2}\dddot{x}_2 + \omega^2 x_2(t) - \Omega^2 x_1(t) = 0.$$

Equation 3.2.1. Including scattering term into the equation of motion for Harmonic Oscillator model.

Where $\gamma_{r1}$and $\gamma_{r2}$are the scattering coefficient for the bright and dark mode respectively. We used the negative sign for the scattering term to keep the radiative force as a reaction force against external force and as an energy loss. Distinguishing between scattering and absorption coefficient give us an opportunity to exclude the force for

absorption and scattering which results in calculation of absorption and scattering power as follows:

$$Extinction = 2\pi\, real(\, F^* \times \dot{x}_1),$$

$$Absorption = 2\pi\, real((\gamma_1 \dot{x}_1)^* \times \dot{x}_1 + (\gamma_2 \dot{x}_2)^* \times \dot{x}_2),$$

$$Scattering = 2\pi\, real((\gamma_{r1} \ddot{x}_1)^* \times \dot{x}_1 + (\gamma_{r2} \ddot{x}_2)^* \times \dot{x}_2).$$

Equation 3.2.2. Total (extinction) dissipation and scattering power during one periode of oscillation.

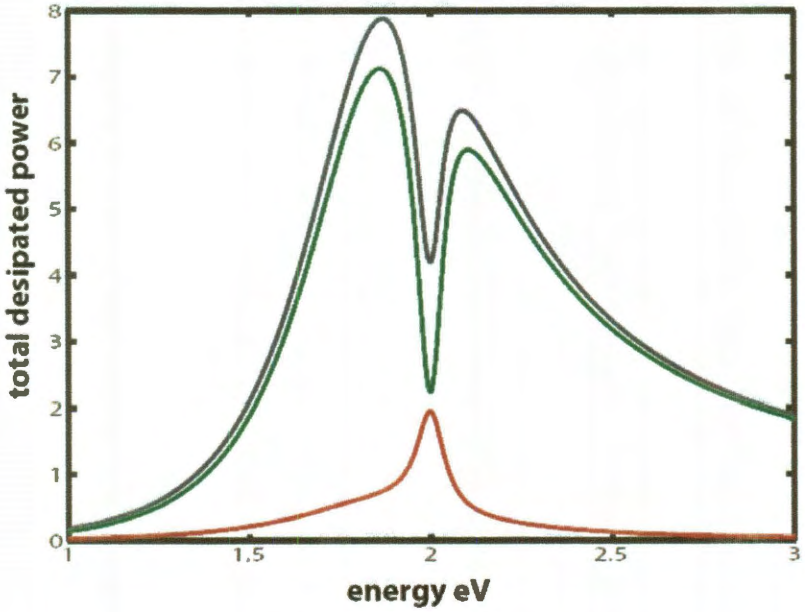

Figure 3.2.1. Extinction (blue curve), scattering (green curve), and absorption power (red curve) is plotted for $F = 1$, $m = 1$, $\omega_1 = \omega_2 = 2.0\, ev$, $\gamma_1 = \gamma_2 = 0.05\, ev$, $\gamma_{r1} = 0.2\, ev$, $\gamma_{r2} = 0.0\, ev$ and $\Omega = 0.6\, eV$ as it is predicted absorption spectra has a peak at the fano resonance deep in scattering spectra.

In Figure 3.2.1 we plotted the dissipated power through scattering and absorption as formulated in Equation 3.2.2 for $F = 1, m = 1, \omega_1 = \omega_2 = 2.0\, ev, \gamma_1 = \gamma_2 = 0.05\, ev, \gamma_{r1} = 0.2\, ev, \gamma_{r2} = 0.0\, ev$ and $\Omega = 0.6\, eV$. Scattering spectra which is plotted

as solid green curve shows a pronounced Fano interference at the dark mode, even though absorption spectra, red curve, have p resonance peak at this frequency. The radiative coefficient for dark mode,γ_{r2}, has been chosen as 0 due to the none radiative nature of dark mode and lake of dipole moment of this mode.

Now that Alzar spring model is improved we can apply our model to some plasmonic structure with Fano resonance transparency in their scattering spectra. In the next subchapter we show how we can apply this model to the Fanoshells and Heptamer clusters.

3.3. Modeling Plasmonic Fano resonances

In this section, we use classical harmonic oscillator to investigate the nature of the Fano resonance in the scattering spectrum for Fanoshell and heptamer structures as it is shown in the chapter 2 of this thesis. Fano resonances in plasmonic systems can be understand by using coupled harmonic oscillator model originally developed as classical analogy to electromagnetic induced transparency (EIT) in atomic systems [63]. Here we used the same model to explain the Fano interference for Fanoshell structures, which is a simple multilayered plasmonic nanoparticle consisting of an Au nanocrystalline core, a silica spacer layer and metallic shell, and heptamer structure with radius 45 nm and gap size of 3 nm made of silver. Fano resonance in the scattering spectra would be induced due to dispersive coupling a narrow dark mode and broad bright mode.

3.3.1. Harmonic Oscillator model for Fanoshell

The optical response of a Fanoshell can be reproduced quite accurately with a mechanical model consisting of three coupled oscillators. The hybridized plasmon modes of the Fanoshell are modeled as three interacting oscillators of frequencies ω_1, ω_2, and ω_3 where $\omega_i^2 = k_i/m_i$ (Figure 3.3.1A). For simplicity we consider the case $m_1 = m_2 = m_3 = 1$. The three oscillators interact with three springs, k_{12}, k_{23}, and k_{13}. The Fanoshell bright dipole plasmon mode is modeled with resonance frequency $\omega_1 = 2.2$ eV, the dark subradiant mode with resonance frequency $\omega_2 = 1.64$ eV, and the quadrupolar mode with resonance energy $\omega_3 = 1.98$ eV. Oscillator 1 is driven by a periodic harmonic force $F(t) = Fe^{-i(\omega t+\xi)}$. This is analogous to optical excitation of the bright, superradiant mode. The subradiant mode represented by oscillator 2, which is connected to oscillator 1 via k_{12}, is only excited due to its coupling with oscillator 1. This coupling is due to the near field interaction between the two modes. The quadrupole mode, represented by oscillator 3, is connected to both oscillators 1 and 2 via k_{13} and k_{23}. These couplings are due to the symmetry breaking and responsible for the red shifting of the subradiant mode with increasing core offset observed in (Figure 2.1.4A). The equations of motion of oscillators 1, 2, and 3 are solved in terms of the displacements x_1, x_2, and $x_3$from their respective equilibrium position in a one-dimensional system

$$\ddot{x}_1(t) + \gamma_1\dot{x}_1(t) + {\omega_1}^2 x_1(t) - {\Omega_{12}}^2 x_2(t) - {\Omega_{13}}^2 x_3(t) = Fe^{-i\omega_s t}/m,$$
$$\ddot{x}_2(t) + \gamma_2\dot{x}_2(t) + {\omega_2}^2 x_2(t) - {\Omega_{12}}^2 x_1(t) - {\Omega_{23}}^2 x_3(t) = 0,$$
$$\ddot{x}_3(t) + \gamma_3\dot{x}_3(t) + {\omega_3}^2 x_3(t) - {\Omega_{13}}^2 x_1(t) - {\Omega_{23}}^2 x_2(t) = 0.$$

Equation 3.3.1. Equation of motion for Harmonic Oscillator model of Fanoshell.

Where $\Omega_{ij}^2 = k_{ij}$ is the frequency associated with the coherent coupling between the interconnected oscillators. The friction coefficient used to account for energy dissipation of the broad superradiant mode is given by $\gamma_1 = 0.65$. Much lower frictional constants were used for the narrower dark modes; $\gamma_2 = 0.08$ and $\gamma_3 = 0.12$ for the subradiant and the quadrupole modes, respectively. To calculate absorption we compute the mechanical power $P(t)$ absorbed by particle 1 from the external force, $P(t) = Fe^{-i\omega t}\dot{x}_1(t)$. By turning off the coupling between the quadrupole mode and the other modes, ($\Omega_{13}^2 = \Omega_{23}^2 = 0$) and by assigning a reasonable coupling between the superradiant mode and the subradiant mode ($\Omega_{12}^2 = 0.5$), the absorbed power of the oscillator system reproduces the plasmonic response of the Fanoshell (Figure 3.3.1B, black curve). For this case, the three-oscillator model is reduced to a two-oscillator model and, as such, yields a single Fano resonance in its spectrum. To simulate the effect of symmetry breaking, a coupling ($\Omega_{13}^2 = 0.6$) is introduced between the quadrupole and the superradiant oscillators. This results in the immediate appearance of a higher energy dipole–quadrupole Fano resonance, which increases in strength with an increase in the coupling constant ($\Omega_{13}^2 = 0.9$) (Figure 3.3.1B). By turning on the interaction between the subradiant and quadrupolar oscillators ($\Omega_{23}^2 = 0.4$) a red shifting of the subradiant mode is observed with a simultaneous reduction in the strength of the dipole–dipole Fano resonance, in excellent agreement with our FDTD simulation results (Figure 2.1.4A).

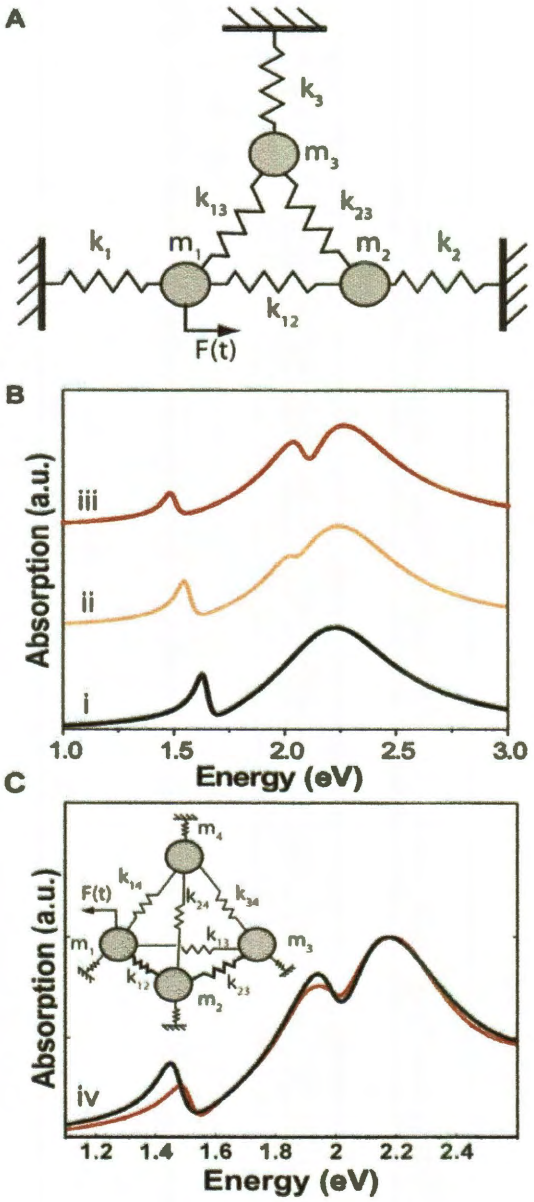

Figure 3.3.1. The coupled harmonic oscillator description of the Fanoshell optical response. (A) Three-body classical oscillator model with masses m1, m2, and m3 coupled with springs. Oscillator 1 is driven by the periodic harmonic force F. (B) The absorbed powe r for various interparticle coupling constants yields the spectra of symmetric (i) and asymmetric Fanoshells (ii, iii). (C) Comparison between the FDTD simulation of a Fanoshell $[r_1, r_2, r_3]$ = [35, 55, 75] nm, with an offset parameter Δ = 10 nm (red) and the four-body oscillator model (black curve and inset).

	i	ii	iii	iv
ω_1, γ_1	2.2, 0.65	2.2, 0.65	2.2, 0.65	2.2, 0.65
ω_2, γ_2	1.64, 0.08	1.64, 0.08	1.64, 0.08	1.64, 0.08
ω_3, γ_3	1.98, 0.12	1.98, 0.12	1.98, 0.12	1.98, 0.12
ω_4, γ_4				2.60, 0.6
Ω_{12}^2	0.5	0.4	0.2	0.1
Ω_{13}^2	0.0	0.6	0.9	0.3
Ω_{14}^2				1.2
Ω_{23}^2	0.0	0.4	0.5	0.5
Ω_{24}^2				0.9
Ω_{34}^2				0.8

Table 3.3.1. Parameters Used for Simulation of Three- and Four-Body Oscillator Model.

However, the Ω_{23} interaction blue shifts the dipole–quadrupole Fano resonance which is opposite to the red shift observed in the FDTD result Figure 2.1.4. The FDTD red shift is due to coupling with higher order multipolar modes which are absent in the three-oscillator model. By introducing an additional coupled oscillator 4 Figure 3.3.1C, inset) one can qualitatively account for the interaction with the higher order modes and reproduce the FDTD spectrum (Figure 3.3.1C). The parameters used in both the three-body and the four-body oscillator model are given in Table 3.3.1.

3.3.2. Harmonic Oscillator Model for Heptamer structure

The optical response of heptamer can be reproduced quite accurately with a mechanical model consisting of three coupled oscillators. This model is an extension of the classical oscillator system used to model EIT. The hybridized plasmon modes of heptamers are model led as three interacting oscillators of frequency $\omega_1 = 2.25$, $\omega_2 = 2.16$ and $\omega_3 = 2.45$ where $\omega_i^2=K_i/m_i$ (Figure 3.3.2A). for simplicity we consider the case $m_1=m_2=m_3=1$. The three oscillator intercating with three springs $\Omega_{12}^2=0.9$, $\Omega_{13}^2=0.9$ and $\Omega_{23}^2=0$. By using higher damping coefficient for oscillator as bright mode ($\gamma_1= 1.0$) and low damping for dark modes, oscillator 2 and 3, ($\gamma_2 = 0.02$ and $\gamma_3= 0.4$) and couple them to each other as it is shown in Figure 3.3.2A, the fano resonance can be reproduced as shown in Figure 3.3.2B with blue curve.

By comparing two fano resonances at 2.16 eV and 2.45eV, it is clear that the nature of fano dip depend strongly on dark mode damping factor. For narrower dark modes fano dip is more pronounce than than broader dark modes. Using this harmonic oscillator give us a good insite of Fano resonance in plasmon modes of nanostructures [82].

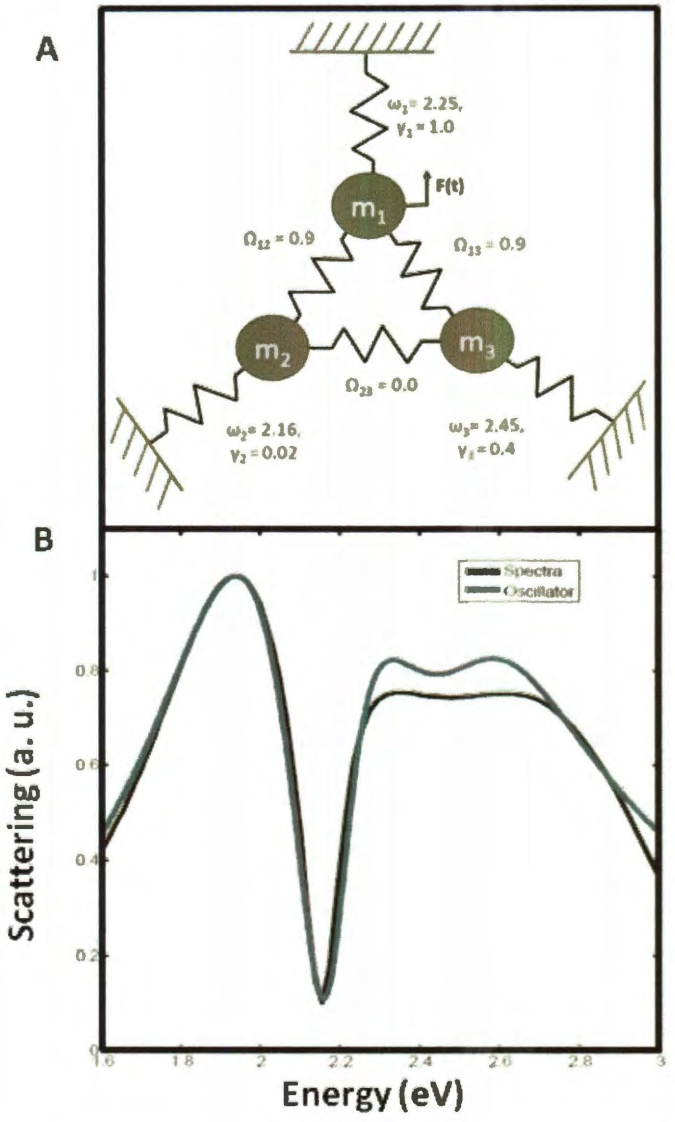

Figure 3.3.2. the coupled harmonic oscillator description of the Heptamer optical response. (A) three-body harmonic oscillator model with masses m1, m2 and m3, coupled with springs. Oscillator 1 is deriven with the periodic hrmonic force F(t). (B) comparision between scattering spectra from Comsol simulation of a heptamer of radius 45 nm with 3 nm gapsize (black) and harmonic oscillator model (blue curve).

3.4. Modeling Cathodoluminescence

Here we examine the plasmonic properties of planar nanoclusters, focusing on arrangements of coupled nanodisks consisting of a central particle surrounded by a ring of peripheral particles. We observe that the depth and width of the FR can be controlled by varying the relative size of the inner particle with respect to the surrounding particles. We also observe that the FR is characteristic of optical excitation of this structure. Excitation by a localized electron beam on various components of the structure does not result in a Fano resonance in the cathodoluminescence spectrum but instead results in the selective excitation of the center disk mode or the peripheral ring mode of the complex. This contrasting behavior can be understood through the coupling between the superradiant and subradiant modes of the cluster, where the contrasting selection rules of optical and e-beam excitation give rise to different superposition of radiant modes in the corresponding spectra. In this system, cathodoluminescence allows us to "deconstruct" the Fano resonance into distinct superposition of super-radiant and subradiant modes not observable by optical means. This analysis gives new insight into the interplay between the subradiant and superradiant modes in coherent plasmonic systems.

The plasmonic nanoclusters studied here were made by Britt Lassiter via planar fabrication. Clusters of nanodisks were patterned by electron beam lithography and deposited by evaporation of 30 nm of Au with a 2 nm Ti adhesion layer. The substrate was a silicon wafer coated with a 100 nm thick oxide layer to ensure that the plasmons did not interact with the conductive silicon surface. In Figure 3.4.1B, SEM images are shown of the specific structures, progressing from (bottom to top) heptamer to octamer,

nonamer, decamer, and undecamer. The disks in the outer ring of each structure are nominally 85 nm in diameter, and the gaps between all particles are approximately 15 nm. As each new particle was added to the outer ring, the central disk was made larger in order to maintain this gap size and preserve coupling between the particles. Thus the inner particle diameters were 85, 115, 146, 177, and 209 nm for the heptamer, octamer, nonamer, decamer, and undecamer, respectively.

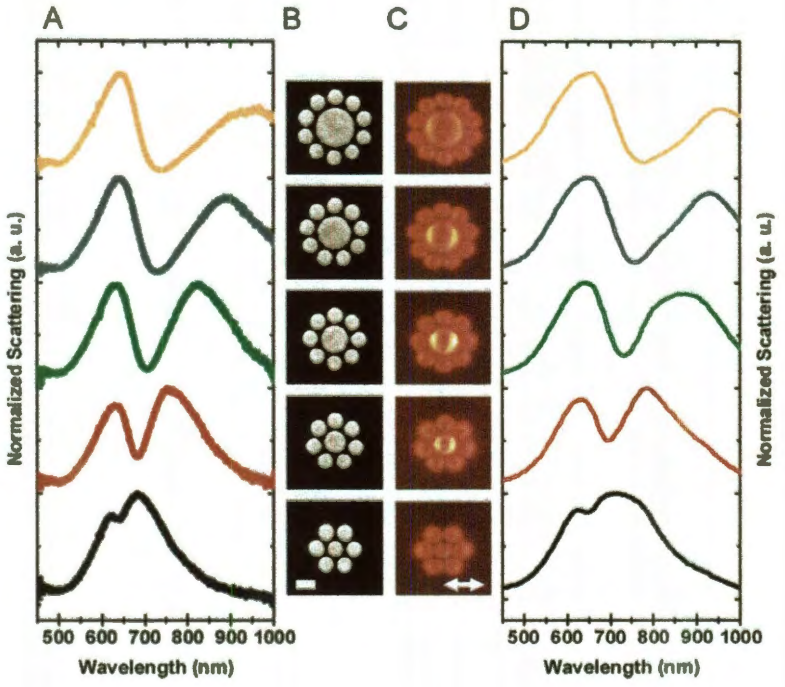

Figure 3.4.1. Scattering spectra of plasmonic nanoclusters. (A) Experimental dark-field spectra of individual structures. (B) SEM images of the structures associated with each spectrum in panel A. Scale bar is 100 nm. (C) Panchromatic cathodoluminescence images for the same structures. Arrow indicates polarization of the collected light. (D) Finite difference time domain (FDTD) simulations of the scattering spectra for each geometry.

Individual scattering spectra for these structures (Figure 3.4.1A) were obtained by dark-field spectroscopy, using a home-built microscope by Britt Lassiter at Rice University. Each spectrum was also simulated (Figure 3.4.1D) using finite difference time domain analysis (FDTD, Lumerical). For these simulations, care was taken to match the experimental conditions as closely as possible. The structures were modeled as 30 nm tall cylindrical Au disks with an experimental dielectric function [68] on a 2 nm thick Ti layer. To include substrate effects, the structures were placed on top of an infinite silica slab (ε = 2.04). The dark-field geometry was taken into account by injecting the excitation and collecting the scattered light at the appropriate angles to match the experimental conditions.

The experimental and simulated scattering spectra for these structures match each other extremely well. Both show a progression where the Fano resonance dip becomes deeper and broader with increasing size of the central disk structure from heptamer to undecamer. For the heptamer, the Fano resonance occurs as a narrow, shallow dip at ~ 650 nm. The dip redshifts slightly and becomes broader and much deeper for the octamer. For the nonamer, the dip has become broader still, but its depth now extends to the baseline, making the nonamer essentially transparent at this wavelength. The decamer and undecamer spectra remain fully transparent at the Fano resonance but continue to broaden even further. This effect illustrates the possibility of precise engineering of the line shape of a plasmonic Fano resonance spectrum, a remarkable prospect for applications requiring precisely controlled and tunable transparency windows. Just as tunable nanoparticles provided a general platform for plasmonic applications across the

full optical and infrared spectrum, plasmonic Fano resonances with engineered depths and widths can provide a general framework for applications using Fano resonances.

To better understand the origin of the Fano resonance in this family of structures, we studied their response using cathodoluminescence (CL) imaging and spectroscopy [83-85]. In cathodoluminescence, the plasmon modes of a structure are excited using a focused, high-energy electron beam (30 keV in this experiment) impinging upon a localized region of choice on the nanoscale complex. The plasmons excited in this manner then radiatively decay and emit light, which is collected by a parabolic mirror and directed into a spectrograph/detector system (Gatan, MonoCL4 Elite) for imaging and spectroscopy. This allows us to construct excitability maps and spectra that are proportional to the radiative local density of states (LDOS) of the structure [86].

The polarized, panchromatic CL images of each structure are shown in Figure 3.4.1C. These images were constructed by changing the optical path of the CL system to bypass the spectrograph, instead routing the radiated light directly to the PMT detector through a linear polarizer. These images allow one to directly access the local density of states of the plasmon modes. In the case of the heptamer, the LDOS on the center particle is similar in strength to the outer particles, but as the center particle size is increased and extra particles are added to the outer ring, the intensity of the central disk becomes markedly stronger. This increase in radiative contribution from the central particle coincides with a deepening of the Fano dip, suggesting the importance of the central particle to the spectral line shape. As the center particle is made larger, the strength of its induced dipole moment is increased, more closely matching the collective dipole moment strength of the outer ring of particles. This leads to complete destructive interference

between the central disk and the outer ring of particles at the Fano resonance wavelength, and therefore complete transparency.

The panchromatic images shown in Figure 3.4.1C provide an intuitive visualization of the plasmon resonances at play in these structures. However, they do not provide wavelength-specific information that would permit us to identify the specific plasmon modes giving rise to the radiative response. To obtain this information, we performed wavelength selected CL imaging on the planar nonamer cluster (Figure 3.4.2). In panels A, B, and C, we show polarized CL images obtained at the selected wavelengths of 660, 700, and 770 nm respectively. Here it is evident that as we move across the Fano resonance from shorter to longer wavelengths, the contribution of the particles in the outer ring diminishes while the contribution from the central particle increases dramatically. Furthermore, cathodoluminescence spectroscopy reveals that under electron beam excitation there are actually two independent resonances associated with either the center particle or the outer ring (Figure 3.4.2D). When the electron beam scans a small region on the side of the central particle (red region denoted in inset image), a lower energy "center particle resonance" is obtained in the spectrum (red), but if the structure is excited by electron beam scanning a small region of a peripheral particle (blue region in inset image), the CL spectrum obtained (blue) shows a higher energy "ring resonance." Most notably, no Fano resonance is observed in the CL response in either case.

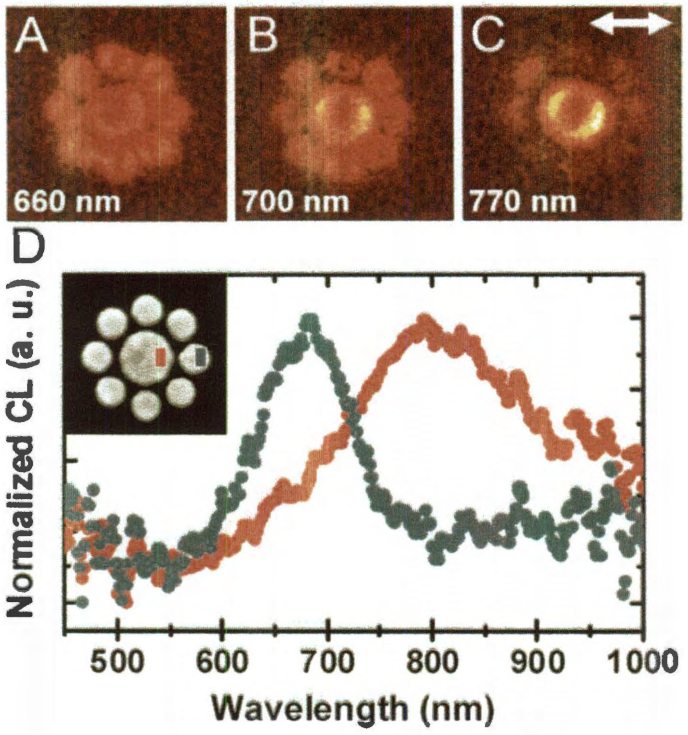

Figure 3.4.2. Polarized, wavelength-selected cathodoluminescence images of a nonamer at (A) 660, (B) 700, and (C) 770 nm. Arrow indicates analyzer angle. (D) Cathodoluminescence spectra where the electron beam is exciting the center particle (red) and a particle in the outer ring (blue). The inset shows an SEM image of a nonamer with blue and red squares to indicate the location of the beam for the blue and red spectra, respectively.

By directly comparing the dark-field scattering spectrum of the nonamer, obtained with optical excitation, with the two CL spectra, obtained with localized electron beam excitation, we see that the crossover between the two resonances observed in CL is located at the same spectral position as the Fano resonance dip in the dark field case (Figure 3.4.3). To understand this behavior, we invoke a coupled oscillator, mass-and-spring model used to describe Fano resonances (Alzar model) (Figure 3.4.3B).

A Fano resonance can be understood using the analogy of two masses, each connected to rigid walls by spring constants k_1 and k_2 and connected together by spring constant K. Here the masses represent the superradiant (m_1) and subradiant (m_2) modes while the spring constant K represents the coupling between them. By applying a sinusoidal force to m_1 only and plotting the power dissipated by m_1, a typical Fano resonance line shape emerges. Here, the dip represents energy where m_2 is "stealing" the oscillation amplitude from m_1. This is directly analogous to the Fano resonances observed in plasmonic systems where plane-wave illumination can only excite superradiant modes, but, due to near-field coupling, energy is transferred to the subradiant mode from the superradiant mode at the Fano resonance frequency. During this transfer, the oscillation undergoes a π-phase shift, resulting in destructive interference of the superradiant mode, resulting in a Fano resonance, in the spectrum. Thus by choosing the correct parameters for the spring constants and damping rates, the dark-field nonamer spectrum (Figure 3.4.3A, green) can be reproduced with remarkable agreement by the Alzar model (Figure 3.4.3C, green).

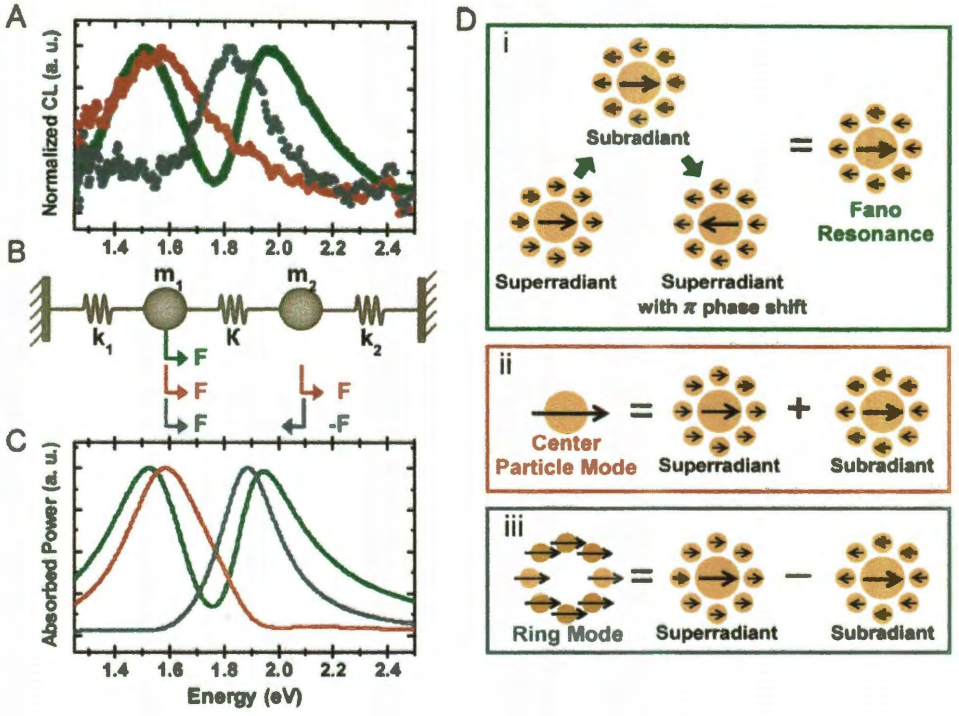

Figure 3.4.3. (A) Experimental spectra of the plasmonic nonamer plotted in energy units: plane wave excitation (green), excitation by electron beam impinging on an outer particle (blue), and the center particle (red). (B) Schematic representing the coupled oscillator model used to generate the spectra in (C). The arrows (colors corresponding to spectra in panel C) indicate how the forces are being applied in each case. (C) Theoretical spectra using the coupled oscillator model. (D) Schematics for the construction of the nonamer modes present in the case of optical excitation (i) and electron excitation (cathodoluminescence) of the center particle (ii) and the particles in the outer ring (iii). Here the arrows in (i) represent energy transfer between modes while addition and subtraction in (ii) and (iii) represents direct excitation of linear combinations of modes.

This simple picture can also be used to explain why the cathodoluminescence spectra (Figure 3.4.3A, blue and red) do not display a Fano resonance. In contrast to plane wave optical excitation that excites the collective modes of the interacting nanostructure, the localized electron beam will couple predominantly to the localized

plasmons in the individual nanoparticle closest to where it impinges. Since the collective modes of the nanocluster can be described as superposition of plasmon modes of the individual nanoparticles, an electron beam can simultaneously excite both the superradiant and subradiant modes. This situation is equivalent to simultaneously applying an oscillating force to both masses in our simple mass and spring model. However, an equal magnitude, sinusoidal force can be applied to both masses in two ways: as an in-phase excitation (red) or an out-of-phase excitation (blue). Using these two excitation conditions, we are able to reproduce the experimental CL spectra with exceptional agreement (Figure 3.4.3C). Note that the slight redshifts of the experimental CL data with respect to the coupled oscillator model are caused by deposition of carbonaceous contamination during the CL experiment due to the high electron beam current. Here, all of the parameters for the masses and springs were kept equivalent to the one-force case (green) and only the excitation conditions were changed. Because in this model the two masses represent the subradiant and superradiant modes of the plasmonic system, applying forces to both masses is analogous to exciting a linear combination of these two modes in the nonamer. We can visualize these three different excitation conditions in the nonamer structure directly. For optical excitation (Figure 3.4.3Di), only one mode is excited, but, characteristic of Fano-resonant systems, there is energy coupling between the superradiant mode excited and the subradiant mode of the structure with energy transfer back to the superradiant mode occurring with a π-phase shift. For CL excitation, when the electron beam impinges on the center particle, the resulting instantaneous dipolar polarization of the disk is equivalent to a symmetric superposition of the sub- and super-radiant modes and thus equivalent to in-phase driving of the two

collective modes (Figure 3.4.3Dii). When the electrons impinge on the ring, the resulting instantaneous polarization of the ring is equivalent to an out-of-phase superposition of the two dominant collective modes (Figure 3.4.3Diii). It is important to note that both the "ring mode" and the "center particle mode" are coupled modes of the nonamer and not uncoupled modes of the constituent particles. We have performed simulations showing that both of these modes observed in our CL spectra occur at different energies than the plasmon modes of uncoupled disks, identical to either the center or ring particles. This picture can now be applied to the CL images and spectra shown in Figure 3.4.2. At longer wavelengths, only the central particle is visible in the CL image because the red spectrum corresponds to the in-phase superposition, while at shorter wavelengths, the particles in the outer ring appear dominant because the blue curve represents the out-of-phase superposition. Note that the central disk is still visible in Figure 3.4.2A because the center particle mode is broad and overlaps with the ring mode at these wavelengths.

3.5. Conclusion

We have shown that Fano resonance can be modeled by a totally classical system, Harmonic Oscillator, introduced by Alzar and his coworkers. The nature of Fano resonance can be understood using analogy of two masses, each connected to rigid walls by two springs and connected together by another spring to demonstrate the coupling between these two plasmon modes. We used two different friction terms to represent the plasmon damping in harmonic oscillator model, although using higher friction for bright mode is necessary to construct a Fano lineshape in the spectra, $\gamma_1 \gg \gamma_2$.

Using basic harmonic oscillator model gave us limited capability to model more complicated Fano interferences in complex plasmonic nanostructures; hence we upgrade our model to the next level by including scattering term in the equation of motion and split plasmon damping to the intrinsic damping, which is associated with the nature of the metal and is due to the coupling to the high energy carrier, and radiative. Radiative damping which is known as scattering damping as well, is proportional to the dipole moment of the plasmon and is related to the shape of particle. Since the radiative damping is proportional to the dipole moment of the plasmon mode, it is clear that bright plasmon mode should have a high radiative coefficient in the spring model compare to the non-radiative modes.

We showed how to use this upgraded system to model Fano resonances induced in Fanoshell structures, which is a simple multilayered nanoparticle consisting of an Au nanocrystalline core, a silica spacer layer and a metallic shell. In the case of Fanoshell we used three-oscillator model to provide a direct mechanical analogy to the coupling

observed in the plasmonic nanoparticle. The analogy provides additional opportunities to design plasmonic effects and to realize them in nanoscale particles, and complex systems. At the end, we have examined the plasmonic properties of planar nanoclusters. We have shown that optical excitation of this family of structures results in a Fano resonance with a spectral line shape that can be precisely controlled, in a sense "designed", by changes in geometry. By also studying the resonant properties of this structure under localized electron-beam excitation using CL imaging and spectroscopy, we have "deconstructed" the Fano resonance observed under optical excitation of this system. We found that under electron excitation, no Fano resonance is present, but rather two independent noneigen polarizations appear, one associated with the central particle only and one associated with the outer ring of particles. The overall resonant behavior of this system has been explained using a coupled oscillator model, where optical and electron-beam excitation correspond to distinct excitation conditions in the coupled oscillator picture. This simple and intuitive approach may be useful in understanding, and ultimately predicting, both the optical and CL responses of additional plasmonic complexes.

Chapter 4

Hot Electron generation

4.1. Introduction

While electron-hole pairs can be generated by direct excitation by light, the process is not very efficient. The probability for direct electron-hole pair excitation is proportional to the square of the local electric field. Thus it is possible to enhance the hot electron population by using metallic nanoparticles with appropriately tuned plasmon resonances. In addition and much more importantly, an excited plasmon can decay into an electron hole pair with a time constant τ_L. This Landau damping depend on the plasmon energy, size of particle, and the symmetry of the plasmon mode. Typical time

scales for Landau damping of plasmon resonances of gold particles in the near IR range from τ_L =1 to 100fs.

In this project we want to pursue a fundamental investigation of how plasmonic nanoparticles can be used to act as efficient hot-electron sources. The two damping mechanisms of plasmon resonances in nanostructures are radiative and nonradiative (Landau) damping. The radiative damping is minimized in subradiant (dark) plasmon modes. The Landau damping is determined by the imaginary part of the dielectric permittivities of the metals in the nanostructures. Thus by tuning a subradiant plasmon mode to energies above the interband threshold, the radiative damping can be eliminated and all plasmons will decay into electron hole pairs. This tuning can be performed either by exploiting the unique geometrical tunability of metallic nanoparticles or by fabricating composite structures consisting of both noble metals and metals with very low energy interband thresholds or with strong intraband transitions such as transition metals. We believe that the unique tunability of plasmonic nanoparticles can offer a possibility of achieving state selective population of adsorbate resonances and thus in principle a path to optical control of chemical reactions on nanoparticle surfaces.

There are numerous other applications of plasmon induced hot-electrons at nanoparticle surfaces. For instance, in a suitable geometry with an applied voltage, it may be possible to directly harvest the hot electrons as currents and thus achieve a photovoltaic device. Hot electrons near the edges of sharp metallic tips may be useful in lithographic applications. Since the hot electrons have energies lower than the vacuum level, they can also be used to create negative ion states of molecules with positive affinities and to create exotic excited molecular states. Hot-electrons are also likely to be

very important in photocatalysts such as TiO_2 with numerous important applications in environmental, chemical and biological sciences. The fundamental mechanism for the catalytic activity of TiO_2 is the generation of holes in the valence band that migrate to the surface where they can participate in chemical reactions. In a recent study it was shown that the photocatalytic activity of TiO_2 can be increased by a factor of 7 by embedding MNP. This increase can be attributed either to a plasmonic enhancement of the electron-hole pair generation in the surrounding TiO_2 or to an efficient generation of hot-electrons in the MNP which transfer into the conduction band of TiO_2 and result in a compensative flow of electrons from the TiO_2 valence band into the nanoparticle (i.e. generation of holes) [87]. With a more efficient generation of hot-electrons in the MNP, the catalytic potential of the TiO_2 particle can thus be enhanced. Many other types of photocatalytic particles with similar possibilities for plasmon enhanced efficiencies have been developed.

When light hits the surface of gold or silver, it can excite collective oscillations of the conduction electrons called surface plasmons. The fundamental mode of the surface plasmons is similar to that of a quantum harmonic oscillator—a sea of electrons oscillates and creates alternating regions of higher electron density (that is relatively negatively charged) and lower electron density (that is relatively positively charged). Many quanta of the incoming light can be stored in the plasmonic oscillator, even when it is illuminated with dim light. In the tetragonal gold nanorods used by Mark knight, the plasmon resonance wavelengths are in the near-infrared, and shorter nanorods will have a shorter peak wavelength.

The light quanta stored in the plasmons can be re-emitted as light, but some of the plasmons can also decay into two charge carriers, an electron and a "hole." It has been known for some time that plasmon decay can create "hot" electrons that have high kinetic energy[29]. However, to create a photocurrent, the electron and hole must be separated [51]. And Extracted into n-type silicon, which has high conductivity for electrons. Normally, these hot electrons would still not have enough energy to enter the conduction band of silicon if they were starting their journey in the occupied molecular orbitals (valence band) of silicon—the energy gap is 1.1 electron volts. The electrons only need to clear a barrier set up at the metal-silicon interface (known as a Schottky barrier; in this case, a barrier of 0.5 electron volt is created by a thin layer of titanium metal used to adhere the gold nanorods). The most energetic fraction of the hot electrons either clears the Schottky barrier, or quantum-mechanically tunnel through it into the conduction band of silicon.

Quantum-mechanical tunneling depends not only on barrier height but also on its breadth. Tunneling is enhanced in this device because the barrier decreases as the electron moves into the silicon, an effect called conduction-band bending. Because the electrons have high kinetic energy, they need travel only a short distance beyond their point of generation before they become conduction electrons in silicon—too short a distance for them to lose energy through other relaxation processes. They then become trapped in the semiconductor by the barrier.

Plasmonic systems can be designed to cover much of the solar spectrum, so this approach suggests a photosensitization strategy, much like the one exploited by Grätzel

in dye-sensitized photovoltaics [88], but avoiding the problem of easily photodegradable organics.

Using Optical nanoantenna for converting photon energy in light to high energy electron can be used to overcome the catalytic activation barrier to derive catalytic reactions. In this chapter, we explore a fundamentally different mechanism of catalytic enhancement, achieved with plasmonic excitation. By monitoring the reaction (using mass spectroscopy), for both situation, with and without external light, we studied the role of hot electron to start a reaction. Using nanoantennas to produce hot electron in chemical reaction is more complicated than harvesting them with a Schottky barrier in photodetectors due to the difficulties of approaching the reactant molecules physically to the produced hot electron before it decays in to the electrons with lower energy in Auger recombination and multi exciton generation (MEG). In the next two subchapters we will explain more about these two processes to harvest hot electrons and our concern in each one.

4.2. Photodetection

Optical antennas are key elements in the conversion of light from free space to ultrasmall, nanometer-scale volumes. The intense light-focusing properties of these structures are due to surface plasmons, oscillations of free electrons in metals that couple to the incident light field. A wide range of applications (in sensing, subwavelength and nonlinear optics, and even novel medical therapies) have arisen for nanoantennas, exploiting the large local electromagnetic fields and intense heating they provide [16, 89-90]. Recent studies have investigated the use of plasmonic antennas to enhance the performance of photoactive devices, such as solar cells, light-emitting diodes, and photodetectors [91-95]. Typically, one or more antennas are placed on or close to the active region of a device, where the near field of the plasmon, the scattering cross section, and the tailored photon density of states may all act to modify and enhance device characteristics.

Another important property of optical antennas is their propensity for generating energetic or "hot" electron-hole pairs by plasmon decay [6, 28-29, 96-100]. Light not redirected by the antenna is absorbed, forming an energetic electron-hole pair. This process is an additional contribution to plasmon damping, broadening the intrinsic linewidth, and is typically considered deleterious to antenna performance. This process of hot electron generation has been shown to participate in photochemical reactions at noble metal nanoparticle surfaces [30-31, 101-103], but it has remained largely unexploited in solid-state devices.

We report an active optical antenna device that uses the hot electron-hole pairs arising from plasmon decay to directly generate a photocurrent, resulting in the detection of light (Figure 4.2.1). Mark Knight accomplished this by a nanoantenna fabricated on a semiconductor surface where a metal-semiconductor, or Schottky, barrier is formed at the antenna-semiconductor interface. When this type of antenna is photo-excited it generates electron-hole pairs [28, 96-98]and injects hot electrons into the semiconductor over the Schottky barrier, contributing to a detectable photocurrent (Figure 4.2.1A). In this configuration, photocurrent generation is no longer limited to photon energies above the band gap of the semiconductor, but rather to photon energies above the Schottky barrier height [104]. Therefore, this device is capable of detecting light well below the band gap of the semiconductor at room temperature and without a bias voltage.

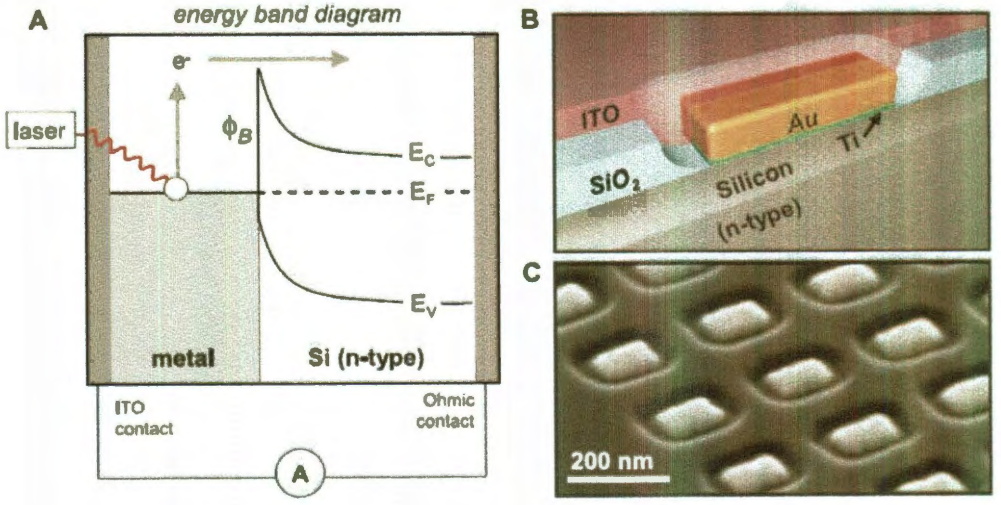

Figure 4.2.1. An optical antenna-diode for photodetection. (A) Band diagram for plasmonically driven internal photoemission over a nanoantenna-semiconductor Schottky barrier (ϕ_B). (B) Representation of a single Au resonant antenna on an n-type silicon substrate. (C) Scanning electron micrograph of a representative device array prior to ITO coating, imaged at a 65° tilt angle.

Our initial realization of active optical antenna-diode photodetection consists of an array of independent, rectangular gold nanorods (Figure 4.2.1A). Nanorods support both longitudinal and transverse plasmon resonances, with the frequency of these resonances determined by the nanorod geometry: Increasing the nanorod aspect ratio tunes the longitudinal resonance to respond at longer wavelengths [105]. The resonators studied here had heights and widths of 30 and 50 nm, respectively, and lengths ranging from 110 to 158 nm. Each device array consisted of 300 devices arranged in a 15 × 20 array with a 250-nm interantenna spacing in both the longitudinal and transverse directions, sufficient to ensure that near-field interantenna coupling is absent. The structure is surrounded by an insulating SiO_2 region (Figure 4.2.1C) and then electrically connected through a top transparent electrode of indium tin oxide (ITO).

The photocurrent obtained from these devices is determined directly by the antenna properties. The photocurrent shows a strong wavelength dependence resulting from the rod geometry, with maximum currents increasing in wavelength with increasing antenna length (Figure 4.2.2A). The spectral response directly follows the longitudinal dipole absorption resonance of the plasmon mode excited on the structure. The polarization dependence of the photocurrent also follows that of the nanoantennas, with a highly polarization-dependent response (Figure 4.2.2B, green points) obeying a $\cos^2 \theta$ angular dependence characteristic of a dipole antenna (gray line). For light polarized along the short (transverse) rod axis, we observe >90% attenuation of the photocurrent with respect to the longitudinal polarization. Incident power variation at a single wavelength results in a linear response of the photocurrent, which suggests that the

photocurrent is dominated by the conversion of single photons to single hot electrons over this range of incident light intensities (Figure 4.2.2C).

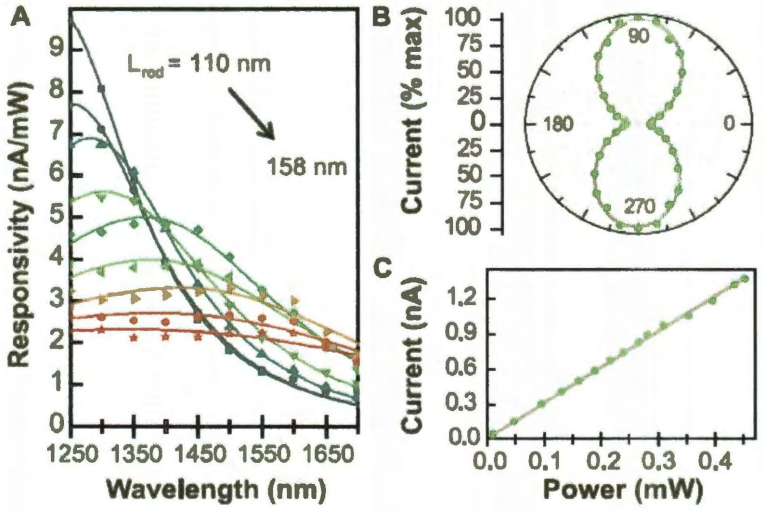

Figure 4.2.2. (A) Experimental photocurrent responsivity for nine different Au antenna lengths: 110, 116, 122, 128, 134, 140, 146, 152, and 158 nm (points). Solid lines: Equation 4.2.2 fit to the data for ϕ_B = 0.5 eV. All nanoantennas are 50 nm wide and 30 nm thick. (B) Polarization dependence of photocurrent for a 140 nm × 50 nm antenna excited at λ = 1500 nm (green points), exhibiting a $\cos^2\theta$ angular dependence (gray line). (C) Photocurrent for a representative antenna as a function of input power (green points).

The responsivity of this device can be understood by first considering a Schottky diode in the absence of a plasmon resonance, where the responsivity depends only on the energy-dependent internal photoemission probability. This quantum transmission probability η_i can be approximated by the modified Fowler theory [106], which describes

the number of "available" electrons in the system with sufficient energy to overcome the potential barrier:

$$\eta_i \approx C_F \frac{(h\nu - q\phi_B)^2}{h\nu}$$

Equation 4.2.1. Transmission probablity aproximation by modified Fowler theory.

Where C_F is the device-specific Fowler emission coefficient, $h\nu$ is the photon energy, and $q\phi_B$ is the Schottky barrier energy. Fitting the responsivity curve of a planar Schottky device with this equation allows one to extract the material-dependent Schottky barrier height for a given metal-semiconductor interface. When the Schottky barrier is formed by a plasmon resonant antenna rather than a continuous film, the device responsivity R will show a Fowler response modified by the plasmon absorption spectrum S:

$$R(\nu) = \eta_i S(\nu)$$

Equation 4.2.2. Fowler response modified by the plasmon absorption spectrum.

With this extended Fowler relation, we can extract the Schottky barrier height for devices with a known plasmon line shape. In general $S(\nu)$ depends on multiple factors, including the geometry, composition, and size of the plasmonic devices. In the quasi-static regime, where the plasmonic particles are significantly smaller than the wavelength of light, the optical response will be dipolar and will exhibit a Lorentzian line shape near the resonance frequency. Fitting the experimental responsivities (Figure 4.2.2A)

with Equation 4.2.2, using a Lorentzian line shape for $S(\nu)$, yields a Schottky barrier height of 0.50 eV. From this analysis we find that the barrier height is determined primarily by the 1-nm Ti adhesion layer and is consistent with Ti/Si Schottky barrier devices [107]. This low barrier height should permit a detection window covering the entire short-wave infrared spectral range (λ = 1.2 to 2.5 μm).

Conversely, with a known Schottky barrier height, the absorption spectrum of an antenna diode of arbitrary geometry can be extracted from the spectral dependence of the responsivity. For our system, the experimental absorption spectra extracted from the overall responsivity (Figure 4.2.2C) using a barrier height of 0.50 eV are shown in Figure 4.2.3A. These experimental spectra exhibit extremely close agreement with calculated absorption spectra (Figure 4.2.3B); both spectral sequences exhibit similar peak locations for nominally identical geometries, exhibiting a linear redshift with increasing aspect ratio, as is characteristic for nanorods. This agreement is notable given that the finite-difference time domain (FDTD) simulations (Figure 4.2.3B) included no adjustable parameters; all calculations were performed with experimental dimensions and literature values for the optical constants of materials (Si, SiO_2, Au, Ti, ITO). This agreement also shows that although the nanoantennas are configured in an array, their response is that of individual, independent nanoantennas and is consistent with the collected photocurrent being generated by hot carriers injected by each discrete nanoscale device.

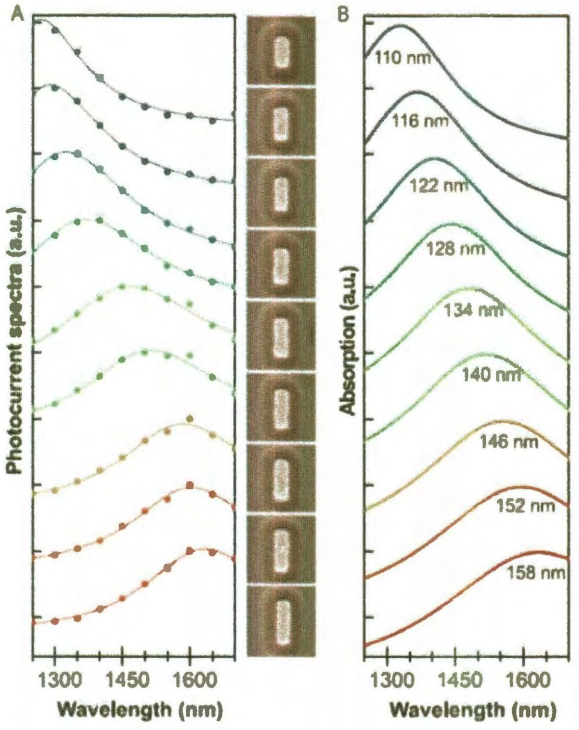

Figure 4.2.3. (A) Photocurrent spectra extracted from the responsivity spectra Figure 4.2.2A (points) fit with Lorentzian curves (solid lines). (B) Corresponding calculated absorption spectra.

When photocurrent measurements are performed on multiple antenna arrays, each with a different resonant frequency, these devices can function as tiny, on-chip spectrometers. This spectroscopic functionality is due to the relationship between photocurrent amplitude and the amplitude of the plasmon resonance at a given frequency. Each antenna array will generate a photocurrent maximum when driven on resonance, with decreasing photocurrent for antennas with a plasmon resonance detuned from the excitation frequency (Figure 4.2.4). The proportionality between photocurrent and relative nanorod resonance amplitudes, expressed in Equation 4.2.2, shows that at a fixed

frequency where η_i is nearly constant, the spectral amplitude is directly proportional to device responsivity. Responsivity curves collected using the nine different antenna lengths presented in Figure 4.2.3 are shown in Figure 4.2.4, which illustrates the remarkable agreement between experimental responsivity as a function of antenna resonant frequency and optical absorption amplitudes calculated using the FDTD method. This spectral sensitivity can be used to determine the wavelength of incident light.

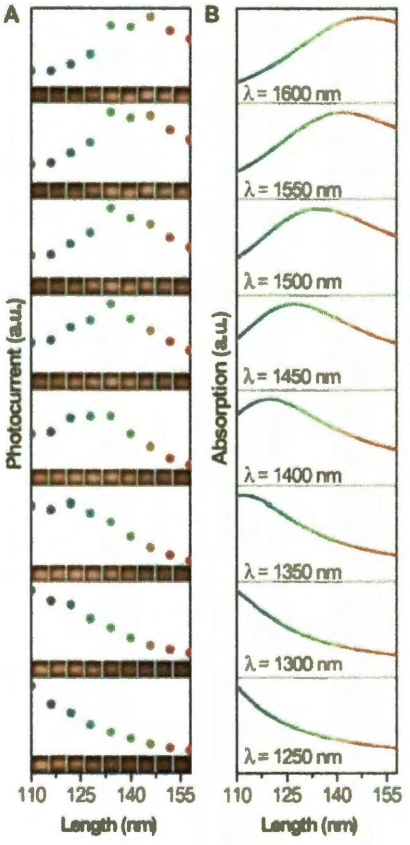

Figure 4.2.4. Sensing the wavelength of incident light. (A) Relative photocurrent amplitudes at fixed wavelengths for the nine resonator lengths in Figure 4.2.3. The color coding of the points is the same as in Figure 4.2.3. Insets: Raw photocurrent images (normalized) for each device array. (B) Calculated absorption amplitudes for devices that are nominally identical to the experimental system.

The overall quantum efficiency of these nanoantenna-diodes depends on the properties of their constituent materials and the specifics of their device geometry, how these factors affect hot electron generation, and the probability that the hot electrons generated will contribute to the photocurrent. Factors influencing the efficiency of hot electron production include the antenna geometry, the electronic structure of the metal(s) constituting the antenna, and the transmission efficiency of light through the uppermost ITO electrical contact layer. The efficiency of converting hot electrons to photocurrent is affected by the Schottky barrier height, the circuit resistance, and other device-specific parameters. For a device where these factors are known, Equation 4.2.2 permits the direct conversion of experimental photocurrent to absolute absorption cross section.

Although the devices presented here enable us to investigate hot electron generation by plasmonic antennas, further optimization can significantly increase their quantum efficiency (at present, 0.01% of photons absorbed by each nanoantenna are converted into photocurrent). The role of the titanium layer appears to be quite critical: Numerical simulations show that the 1-nm layer is responsible for producing nominally 33% of the hot electrons, which would increase to more than 50% for a 5-nm thickness. Further experimental studies have indicated that reducing extraneous Ti oxidation during the fabrication process, improving ohmic contacts, and increasing the conductivity of the uppermost ITO layer can collectively increase device efficiency by more than an order of magnitude. In addition, a reverse bias of 1 V increases the photocurrent by a factor of 20. Together, these improvements would boost the quantum yield to nearly 2% over the spectral range of the device.

4.3. Photochemical Reaction

With the emergence of simple ultrafast laser sources in the nineties, Surface Femto-Chemistry (SFC) became an intense research field of both fundamental and technological relevance. When a laser pulse is incident on a metal surface, it generates a distribution of electron-pairs of excitation energies equal to the energy of the incident photons. This highly non-thermal hot-electron distribution subsequently undergoes carrier multiplication through electron-electron scattering processes such as Auger transitions and result in a distribution of many lower energy electrons. After a timescale τ_{th}, the distribution of these secondary lower energy hot-electrons can be approximately modeled as a Fermi Dirac (FD) distribution characterized by a large effective electron temperature T_{el}. These lower energy electrons can interact efficiently with phonons. The subsequent equilibration with the lattice, which is characterized by a lattice temperature T_L occurs over a timescale τ_{ph}. The dynamics of this process can be well described using the so-called two temperature model where the T_{el} and T_L now become time dependent and eventually become equal. In typical experiments on metal surfaces τ_{th} has been found to vary between 100-500fs for transition metal surfaces to around 1ps for Au surfaces [108].The longer timescale τ_{ph} can extend to several picoseconds.

In their transient higher energy states, the hot-electrons can excite significant electronic or vibrational transitions in molecules adsorbed on the metal surfaces and thus catalyze chemical reactions. Since the original study of hot-electron induced oxidation of CO adsorbed on a Ruthenium surface [109], many such hot-electron induced studies have been published [110-111]. The basic mechanism is illustrated in Figure 4.3.1.

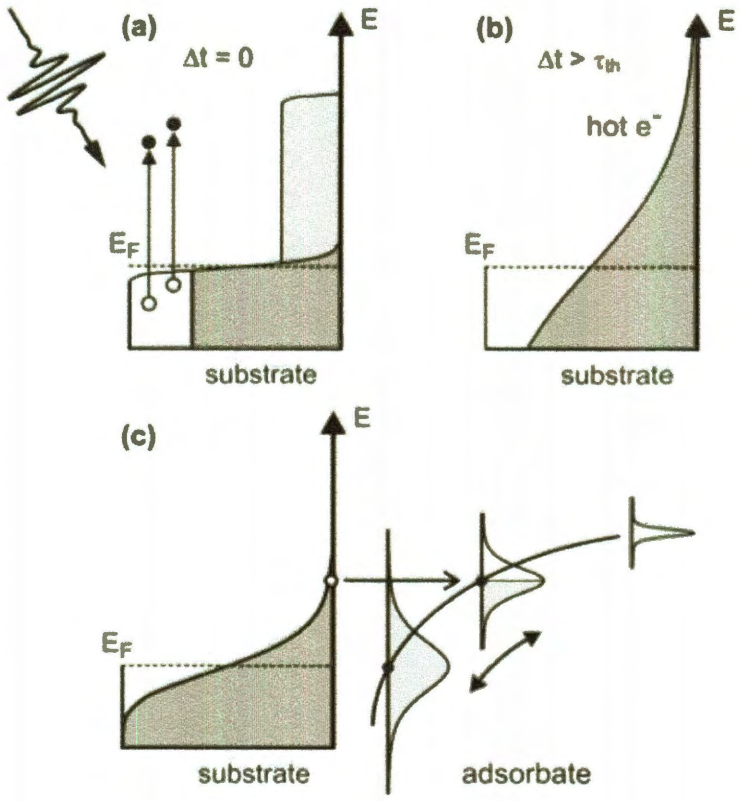

Figure 4.3.1. Schematic showing the dynamics of photoexcited hot-electrons on a metallic surface following a laser pulse. (a) Initial non-thermal hot electron distribution. (b) Initial high T_{el} Fermi Dirac distribution. (c) Intermediate $T_{el}(t)$ Fermi Dirac distribution for $\tau_{th}<t<\tau_{ph}$. Panel (c) also shows a schematic adsorbate resonance that may be populated by the hot electrons. If this state is antibonding with respect to a reaction coordinate and the hot electron distribution overlaps the resonance for sufficient amount of time, the hot electrons may induce a change of the reaction coordinate. From C. Frischkorn and M. Wolf, Chem. Rev. 106(2006)4207-4233

On extended metal surfaces, the timescale τ_{th} is too short for the initial non-thermal hot-electron distribution to have a significant effect on the adsorbate. The hot-

electron induced chemistry occurs after the high temperature FD electron distribution has formed. Although the initial effective hot-electron temperatures T_{el} can be several thousand Kelvin, adsorbate resonances near the vacuum level cannot be populated. In addition, since the FD distribution involves a continuous distribution of excited electrons ranging from the Fermi level to $k_B T_{el}$, all adsorbate resonances between the Fermi and vacuum level can be populated. Thus state-selective population of specific adsorbate resonances cannot be accomplished [112]. This conclusion is supported by many experimental studies showing that there is no significant wavelength dependence of many of the SFC phenomena. Narrow tunable hot electron distributions based on direct photoexcitations has been theoretically predicted in narrow Metal-Insulator-Metal (MIM) devices [113], but have only recently been fabricated [112].

On Metal Nano Particles (MNP), the lifetimes of the initially generated non-thermal hot-electrons can be much longer than on extended substrates because of the increased confinement and reduced electron-electron interactions [111]. Also the equilibration times with the lattice will be longer due to reduced electron-phonon coupling in nanostructures. For instance in a study of small Ag particles on graphite, τ_{th} was found to be around 2ps [114]. Such long lifetimes would allow for state-selective population of adsorbate resonances. Thus by populating specific antibonding adsorbate resonances, it may be possible to selectively induce desorption, dissociation, or translational motion of the adsorbates on the MNP surface.

While electron-hole pairs can be generated by direct excitation by light, the process is not very efficient. The probability for direct electron-hole pair excitation is proportional to the square of the local electric field. Thus it is possible to enhance the hot electron population by using metallic nanoparticles with appropriately tuned plasmon resonances. In addition and much more importantly, an excited plasmon can decay into an electron hole pair with a time constant τ_L. This Landau damping depend on the plasmon energy, size of particle, and the symmetry of the plasmon mode. Typical time scales for Landau damping of plasmon resonances of gold particles in the near IR range from τ_L =1 to 100fs.

In this section we will explore hot-electron generation in complex metallic nanostructures using computational electromagnetic modeling using the Finite-Difference Time-Domain and Finite Element Method and using our fully quantum mechanical TDLDA, time-dependent local-density approximation, method. The electron hole pair production during plasmon excitation can be calculated directly from the local electric fields and currents in a nanostructure following excitations. The rate depends on the imaginary part of the dielectric permittivity and is proportional to $g(r)(E(r))^2$, where E(r) is the local electric field at position r and g it the Landau damping rate. The Landau damping rate is proportional to the imaginary part of frequency dependent permittivity $Im[\varepsilon]$ and can also be calculated perturbatively. Depending on the symmetry of the plasmon mode, it is possible to increase or decrease the absorption. For instance in a metallic nanoshell, the bonding dipolar plasmon resonance have very small internal fields and therefore relatively poor electron hole pair production. However, the dipolar antibonding resonance induces a large electric field within the metallic shell and will

result in significant electron hole pair production. The same difference also applies for thin metallic films. The antibonding film plasmon with its large internal fields will result in significantly larger electron hole pair production than the lower energy bonding mode.

Among particularly promising structures for electron-hole pair production are dark plasmon modes, i.e. plasmon modes with reduced radiation damping. Examples of such modes are subradiant heptamer resonances or bonding dipolar ring/disk cavity modes. We have an established track record in modeling, tuning, and fabricating plasmonic nanostructures supporting plasmons of desired properties.

Heterogeneous catalysis is one of the most crucial processes involved in energy harvesting. Most of commercial heterogeneous catalytic reactions, however, run at high temperatures which degrade the performance and stability of catalysts. Hydrogen, the most abundant element in the universe, is the essential source of energy. Here we report photocatalytic dissociation of H_2 molecules on plasmonic nanostructures using visible light at room temperature. Light excites surface plasmons in the Au nanodisk dimers and these plasmons can nonradiatively decay into high energetic electrons called hot electrons as you can see in Figure 4.3.2A. In their transient higher energy states, these hot-electrons can populate the antibonding orbital of H_2 molecules adsorbed on the metal surfaces and thus trigger the H_2 molecule dissociation, Figure 4.3.2B. We show all optical control of the photocatalytic dissociation by tuning the light polarization as well as the resonance wavelength of the plasmonic nanostructures. We further demonstrate the high efficiency of our photocatalytic system by detecting the formation of HD molecules

from the individual dissociation of two isotopes, H_2 and D_2. This method will open a new pathway towards the application of low-cost and noninvasive catalysts and nanoreactors.

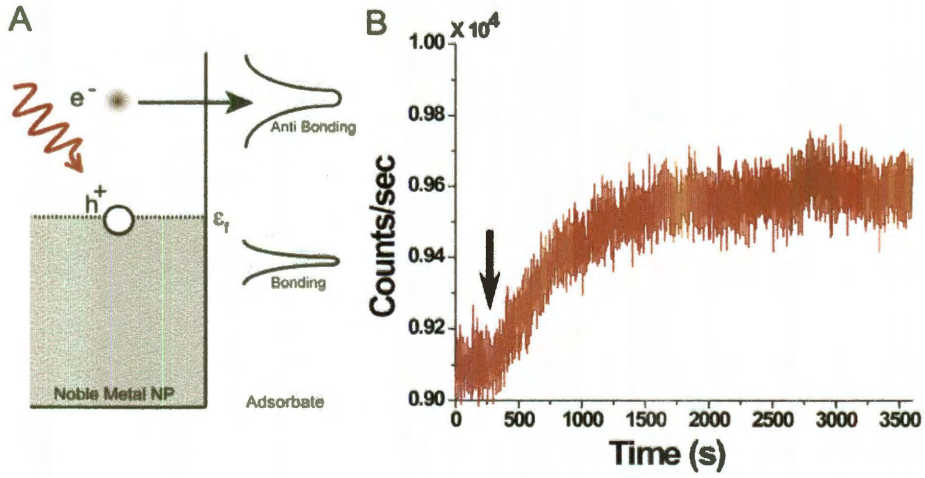

Figure 4.3.2. (A) Schematic showing the non-equilibrium population distribution of photo-excitated hot electron-hole pair on the surface of a noble metal nanoparticle. The highly energetic electrons rest above Fermi energy of the metal & can occupy anti-bonding states of adsorbed molecules to induce dissociation. (B) Real time detection of HD formation on the surface of plasmonic disk dimmers using quadrupole mass spectroscopy. First 10 sccm of H_2 and 10 sccm D_2 is flowed over the plasmonic Au-dimer arrays kept in a airtight chamber and HD formation is monitored in dark for 7 mins after which a supercontiinuum laser is irradiated on the sample with an of intensity of 8W/cm^2 (shown by the arrow). The laser is switched off after 45 mins. Clear evidence of evolution of HD is observed. Figure is done by Shaunak Mukherjee.

For real time detection of HD formation on the surface of plasmonic metallic nanoantenna Naomi Halas graduate student Shaunak Mukherjee built a sophisticated optical table in which gas pipelines carries H2, D2 and Ar gas to the sample chamber. Using optical lenses and beam splitter he achieved to focus the beam in to the chamber window on the sample inside the chamber. A valve has been installed on the other side of the chamber to let the combined gas blow through the sample and fellow out to the Quadrapole Mass Spectrometer as you can see in Figure 4.3.3.

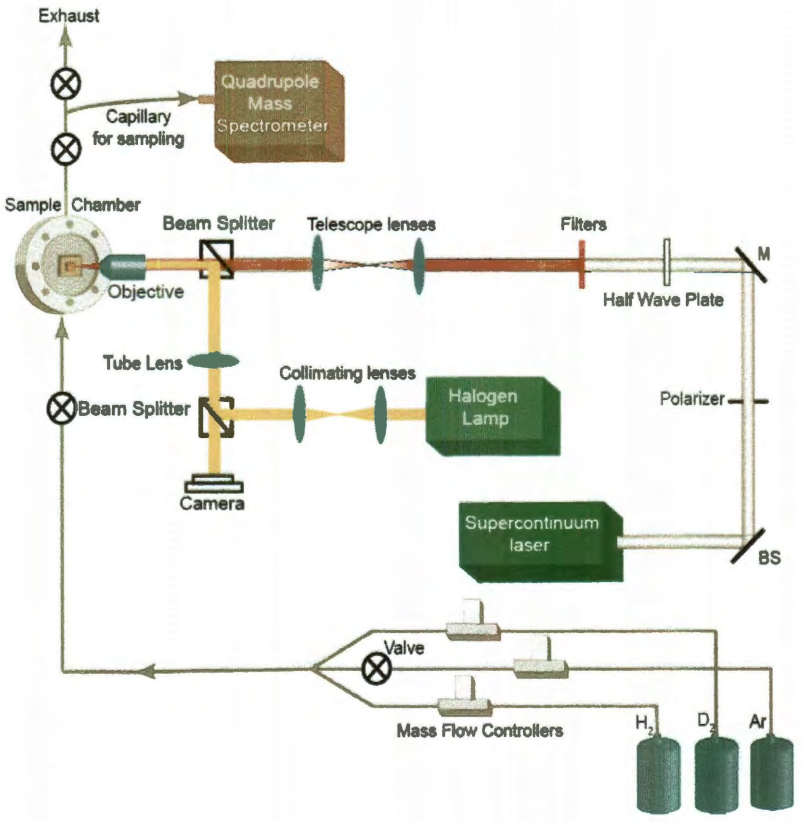

Figure 4.3.3. Experimental set up for photocatalytic dissociation of H_2 molecules on plasmonic nanostructures using visible light at room temperature.

Using simple plasmonic structure such as colloid is a good start for real time detection of HD formation on the surface of plasmonic structures. Even though using TiO2 in our plasmonic structures bring us some complexity to the process due to the mysterious behavior of Ti as a catalysis we used Au colloid and supported by TiO2. In Figure 4.3.4 the real time HD production is plotted while the illumination light is switched on and off.

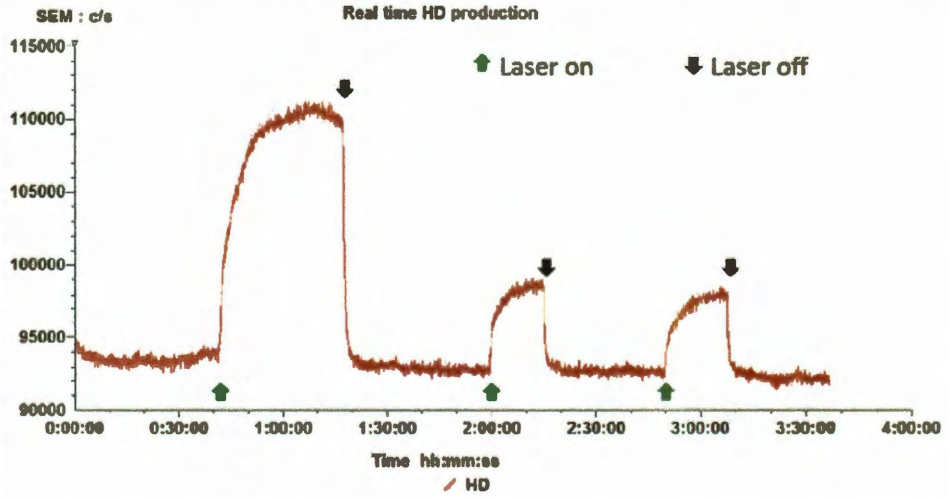

Figure 4.3.4. HD production for gold colloid supported with TiO2.

H2 and D2 gas are conducted in the sample chamber for 40 minutes before illuminating the sample with the white light to achieve a stable measurement from the mass spectrometer. By exciting the colloid particles by white light after 40 minutes, we observed a big raise in HD production monitor which support our prediction, and turning of the external light at 1 hour and 15 minutes is followed by an immediate drop in HD rate in our chamber. Repeating this experiment over and over confirm our results, however this time the production rate and changes are lower than the first result as you

see at time interval 2:00:00 to 2:20:00. This effect is due to burning our sample in the first step when we illuminate our laser in a highly focused beam to the sample. Although this result is a good start toward our mission, but it does not full fill our quest since the role of TiO2 in this reaction is not completely understand and using TiO2 as a support around gold colloid bring some doubt to the plasmonic effect in the outcome. Using pure gold nanostructure, which supports plasmons and are polarization dependent instead of Au/TiO2 colloid with a polarization symmetry help us to answer some of the doubt and concern about previous experiment.

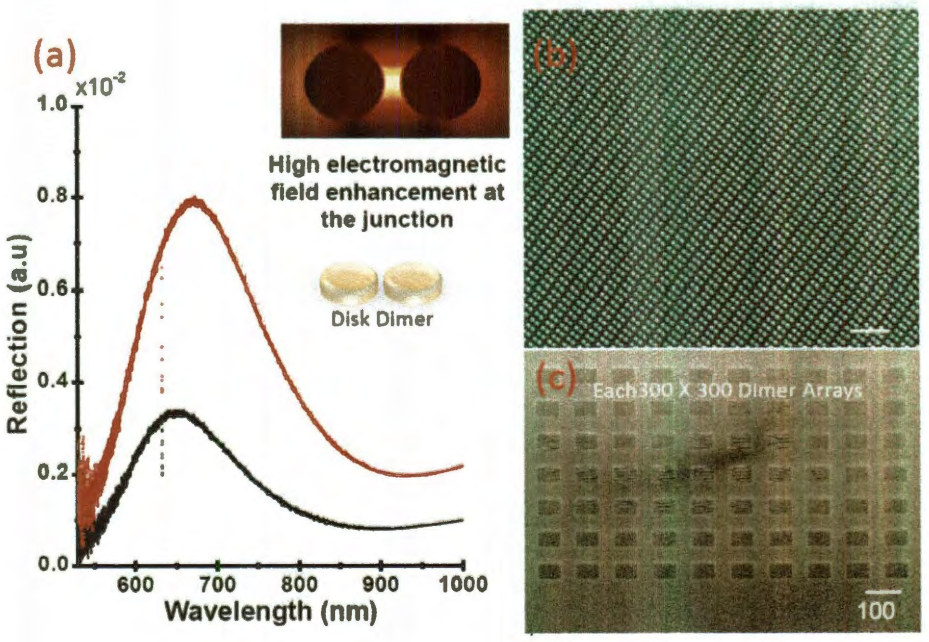

Figure 4.3.5. Dimer array nanostructured build with E-beam lithography and measured by Shaunak Murkherjee. (A) the plasmon resonance has been tuned to 600-700 nm wavelength. (B) SEM image of the array of dimers which has the same nominal size. (C)This arrays are the building blocks of the sample.

Using FDTD simulation for gold and Palladium disks dimer, we tuned disk dimer to provide the plasmon resonators at the visible range 600-800 nm wavelength to support polarization asymmetry plasmon as shown in Figure 4.3.5A. Using disk dimer as shown above has two benefit over our previous sample: (1) this structures has high electromagnetic field at the dimer gap which increase the chance of H2 and D2 gas molecule to dissociate with hot electron produced by plasmon and (2) by tunning our laser excitation at the plasmon resonance for axial polarization we would see a major polarization reliance to our HD production. Figure 4.3.5B shows an array of dimers which are building block of 300 × 300 arrays of dimers in the sample (Figure 4.3.5C).

Although using gold dimer to generate hot electron for HD formation requires that Hydrogen and Deuterium to approach gold surface and stick for dissociation process which involves reduction of hot electron from the surface to the Hydrogen antibonding Orbital, but gold has a very low surface tension for Hydrogen molecules. Keeping the advantages and disadvantages of gold dimer in our mind we decided to move to the other metals which has better surface-tension for Hydrogen surface chemistry such as Palladium and structured composed of mixture of gold and Palladium. These structured are designed and tuned to the excitation laser wavelength and Shaunak Murkherjee in Naomi Halas Lab is currently running experiment to measure the new sample HD production.

4.4. Conclusion

We have learned in this chapter that, when light hits the surface of the gold or silver nanoparticles it can excite collective oscillations of the conduction electrons called surface plasmons. This surface plasmon decay into the electron-hole pair with the excitation energy equal to the energy of the plasmon resonance. This high energy electron (hot electron) subsequently undergoes into the carrier multiplication through electron-electron scattering processes such as Auger transitions and result in a distribution of many lower energy electrons. After a time scale of 100-500 fs the distribution of these secondary lower energy hot electrons can be modeled as a Fermi-Dirac (FD) distribution with a high effective electron temperature. The low energy electrons eventually experience electron-phonon interaction and the plasmon energy will transfer to the lattice thermal vibration in about time interval of 1-10 ps.

By using tunable Nanorods to create plasmons at different wavelength, visible to Infrared, and fabricating these Nanorods like nanoantennas that harvest light photons and convert the resulting plasmonic energy into an electric current without the need for an applied bias voltage. The plasmon energy can be re-emitted as light, but some of the plasmon can decay into the hot electron, however to prevent hot electron energy to decay into the lattice vibrations the electron and holes need to be separated. Introducing a barrier such as Schottky barrier with lower energy than hot electrons will satisfy our purpose for separating electron and holes. The electrons only need to clear a barrier set up at the metal-silicon interface which has a barrier height of 0.5 ev. Because the electron have high kinetic energy, they need travel only a short distance beyond their point of

generation before they become conduction electrons in silicon, too short a distance for them to lose energy through other relaxation processes. Plasmonic systems can be designed to cover much of the solar spectrum, so this approach suggests a photosensitization strategy.

At the end of this chapter we reported photocatalytic dissociation of H2 molecules on plasmonic nanostructures using visible light at the room temperature. Light excites surface plasmons in the gold nanodisk dimers and these plasmons can decay to hot electrons. In their transient higher energy states, these hot-electrons can populate the antibonding orbital of H2 molecules adsorbed on the metal surfaces and thus trigger the H2 molecule dissociation. Experimentalist in Naomi Halas lab, Shaunak Murkherjee, is working on this project to show all the optical control of the photocatalytic dissociation by tuning light polarization as well as resonance wavelength of the plasmonic structures. The goal is to demonstrate the high efficiency of the photocatalytic system by detecting the formation of HD molecules from the individual dissociation of two isotopes, H2 and D2. This work will open a new pathway towards the application of low-cost and noninvasive catalysts.

Chapter 5

Lightning-Rod Effect

5.1. Introduction to lightning-rod effect

One of the applications of the Plasmonics, which attracted many scientists, is the development of substrates capable of providing hospitable environment to detect spectroscopic signals for molecules. The resonant excitation of plasmons in metallic nanostructures provides large field enhancements on the surfaces of metals, which induce dramatic increases in the detected spectroscopic signals for molecules adsorbed on their surfaces. The most popular SES among the scientist is surface enhanced raman scattering (SERS) since the electromagnetic enhancement factor is proportional to the fourth power

of the field at the molecule spot. In this chapter we are going to introduce another type of SES, Surface enhanced infrared absorption (SEIRA). Masatoshi Osawa used this method, in 2001 for the first time, to get 10-1000 times more infrared absorption for molecules on metal island films than the expected conventional measurements without the metal [55]. This method has been the center of attention for some scientist since then [13, 56-58, 115]. Even though the electromagnetic enhancement in SEIRA is only proportional to the square of the electromagnetic field, SEIRA is likely to play an increasingly important role in the field of chemical and biological sensing since it probes dipole-active vibrational modes, providing a complementary vibrational analysis of analyte molecules.

One of the reasons why SEIRA has received so much less attention than SERS has been the limitation in designing and fabricating nanostructures with reproducible tunable plasmon resonances across the broad infrared (IR) region of the spectrum utilized in this spectroscopy. The electromagnetic enhancement follows the same trend as resonant excitation plasmon which has a peak in the visible and UV regions of the spectrum. The primary purpose of this chapter is to design and built a single nanoantenna that has strong extinction spectra in NIR-MIR region of spectrum to enhance electromagnetic field large enough for detecting single molecule. We use micro meter size dimer antenna with 10-30 nm gap size to achieve high electric field at the gap caused by the "lightning-rod" effect, which occurs when metals act as perfect conductors and expel the electric field from the interior of the metals as shown in Figure 5.1.1.

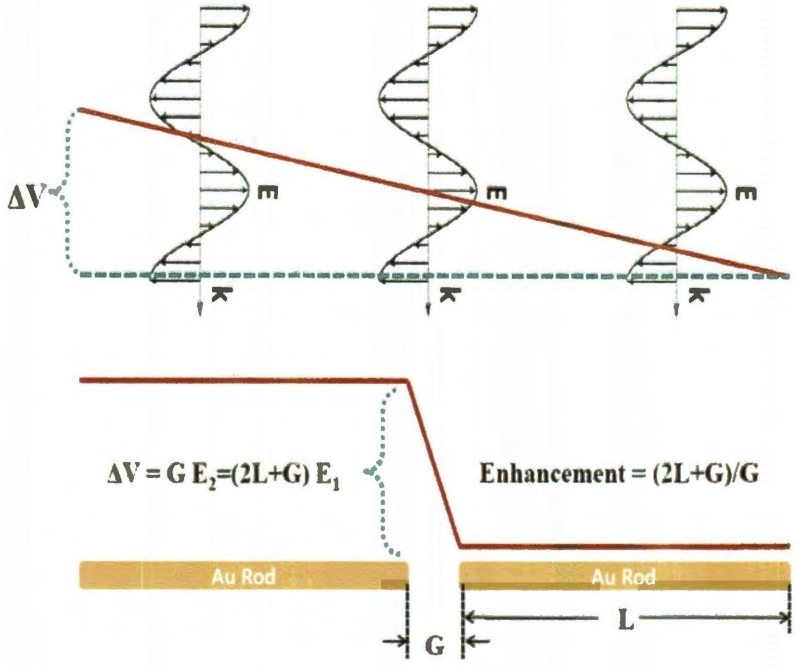

Figure 5.1.1. A micro meter dimer nanoantenna with gap 10-30 nm expels the electric field from interorr metal arms into the gap.

In Figure 5.1.1 we schematically illustrate that how the electric field will be expelled in the gap. Modeling gold rods as the perfect conductors result in the constant potential in the metal rods, however the potential difference between two ends of the dimer arms is $\Delta V = (2L + G)E_1$ where E_1 is excitation plane wave electric field. Hence the potential difference between two sides of the gap is equal to the potential difference at the ends of the rods$\Delta V = GE_2$. Using these two equations we will get the enhancement factor $\eta = E_2/E_1 = (2L + G)/G$.

5.2. Experimental and theoretical approach

The optical and electromagnetic properties of micrometer rod dimer arrays on the SiO2 substrate has been studied by Lisa Brown in the Naomi Halas Lab before and after etching SiO2 layer with HF as shown Figure 5.2.1 (A, B). FTIR spectra for these antenna shows some pronounced deep which are formed due to the interactions of the charge oscillation in the rod antennas and phonon in the Silicon substrate. Etching SiO2 layer reduces this effect but unfortunately it doesn't get rid of it Figure 5.2.1C. To avoid the phonon scattering we considered the other possible substrate such as BaF2 and ZnSe and tuned the spectra to the MIR range.

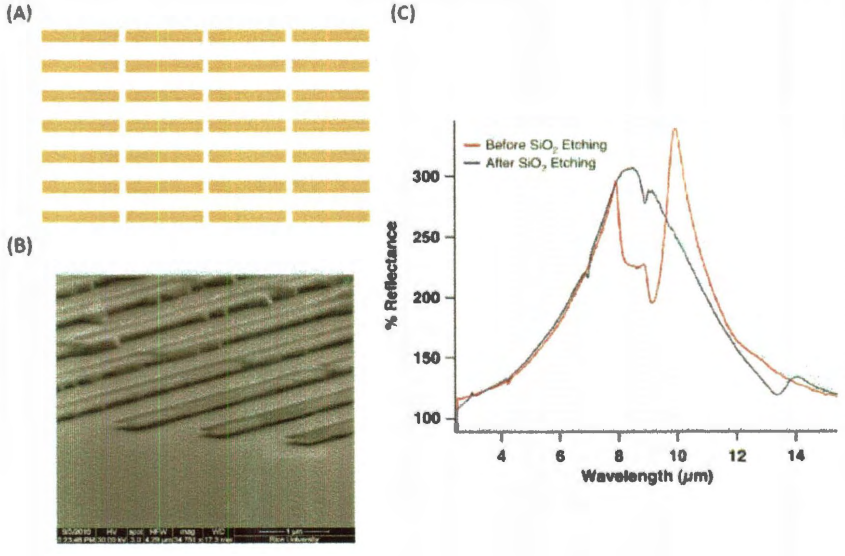

Figure 5.2.1. (A) Gold rod arrays has been fabricated to achieve the lightning-rod effect in MIR range. (B) STEM image of the structure has been shown after HF etching of SiO2. (C) Etching SiO2 layer reduces phono scattering but it won't remove it.

We used Finite Difference Time Domain (FDTD) simulation to design the proper antenna arrays with enough Electromagnetic field enhancement and tuned plasmon resonance to do SEIRA measurement for Hemoglobin molecules. Here in Figure 5.2.2A it has been shown that how the enhancement factor is related to the gap size for the rods with length of 500 nm, width of 60 nm and Thickness of 30 nm. Since we used an array therefore $\eta = (L + G)/G$ which is about 26 for rods of 500 nm Length and 20 nm Gap, however it is calculated as 15 for blue curve in Figure 5.2.2A. This discrepancy is due to the assumption we made earlier about the pure conductive behavior of gold rod at this wavelength. Figure 5.2.2B shows the same investigation for the lightning rod dependency on the length of the rod. It is clear that by increasing the length enhancement factor increases and the plasmon resonance mode redshifts.

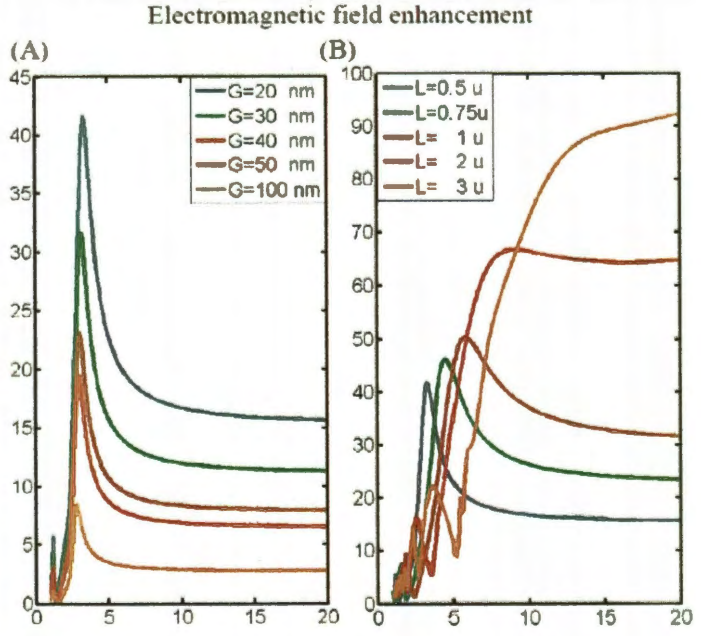

Figure 5.2.2. FDTD simulations results for different rod arrays with different gap sizes (A) and different length (B). Width and thickness of these rods are 60 and 30 nm respectively.

To achieve our initial goal, which would be SEIRA detection for single hemoglobin molecule on single antenna, Lisa Brown moved on to the next geometry, Tetramer antennas. In this geometry we use four rods in a cross position with a sharp arrow head. This geometry doesn't increase the molecule signal for polarized light, although it has a strong effect on unpolarized light. Using this antenna and using some FTIR techniques helped us to detect a clear signal for hemoglobin molecules from two antennas. Hemoglobin molecules can be modeled as an artificial sphere nanoparticle with Lorentzian dielectric function:

$$\varepsilon(\omega) = \varepsilon_b + \frac{f}{\omega_0^2 - \omega^2 - i\Gamma\omega}$$

Equation 5.2.1. The effective dielectric permittivity used to modeled Hemoglobin molecule as a lorentzian oscillator. ε_b is the background dielectric permittivity, ω_0 is the molecule vibrational mode, Γ is the linewidth and f is the oscillator strength.

Using this model for hemoglobin molecules it has been shown by Ke Zhao that the molecules contribute to the SEIRA spectra measurement by introducing a Fano shape deep in the transmission spectra if and only if they are located in the antenna gap. Unfortunately since we haven't published our result I am obligated not to show the experimental results and avoid further explanation.

5.3. Conclusion

Using the FDTD we have analyzed the electromagnetic properties of Nanorod antenna arrays and tetramer antenna. We introduced lightning rod effect in metallic nanostructure and have shown the relation between the geometry properties and the electromagnetic field enhancement. An analysis of the electromagnetic field enhancements in the rod array structure reveals large field enhancements in the rod junctions In MIR region of spectrum. The field enhancements peak is associated with the charged oscillation in the rod. The field enhancements induced in the MIR is not caused by excitations of plasmons but is a consequence of metallic screening, that is, the lightning-rod effect. At long wavelengths, metals behave like perfect equipotential conductors and all the field enhancements result from the drop of the potentials across the junctions between individual nanoparticles. In this limit, the field enhancements depend only on the geometrical structure of the substrate. Our observation that the field enhancement in the MIR does not depend sensitively on wavelength is another advantage for SEIRA where the measurements need to be performed over an extended spectral region.

Our initial investigations indicate that such a substrate should be composed of high aspect ratio antennas, large rods and small gap. Using analytic model for hemoglobin molecule we have shown that the SEIRA signals come from the molecules vibrational in the gap. The field enhancement is also more constant and homogeneous compared to the plasmon resonances in the visible and near IR, therefore the common magnification of the infrared signal has the advantage of preserving the information on

the relative weight of the absorption peaks. Moreover, because the nature of the enhancement in the far-infrared is connected with the exclusion of the field from the conductor-like material, the trends for optimizing the enhancement can be extrapolated to Terahertz frequency regions, thus having a great potential for SEIRA in this relatively unexplored spectral range. The concepts shown in this chapter could lead to a new paradigm in the design of efficient substrates for far-infrared (SEIRA) spectroscopies.

Chapter 6

Conclusion

In this thesis, we have theoretically and experimentally investigate the optical properties of plasmon resonances in metallic nanostructures. In chapter 2 we have been exploring the destructive coupling between superradiant mode, with high radiative dipole mode, and subradiant mode, without radiative dipole. This interference which appears as a transparency dip in the scattering spectra is called Fano resonance. Two nanostructure has been introduced with pronounce Fano resonance in detail, Fanoshell with build in Fano resonance and different arrangement of disk clusters such as Heptamer. The coupling between bright and dark mode in Fano resonance has been assessed with near-field measurements to reconfirm our hypothesis.

We studied the near-field properties of Fano resonance plasmonic clusters by examining both their dark field scattering and their SERS response. Lack of radiation at the Fano transparency window causes the storage of photons as near-field enhancement in the cluster hot spots. The effect of the enhancement on the SERS measurement has

been studied. We used Raman-active molecule *p*-MA molecule and Carbon dot for SERS measurement to show that the enhancement are greatest when the pump laser and stokes mode of interest are at the Fano dip. Further we look into LSPR sensitivities for plasmonic structure with Fano resonance and we measured a FOM of 5.7, the highest LSPR figure of merit reported so far for a single nanostructure.

A simple harmonic oscillator model can be used to understand the nature of plasmonic Fano resonance. Using simple harmonic oscillator gave us a limited capability to model complicated Fano resonances therefore we improved our model by including the scattering term in the equation of motion. We split plasmon damping to the intrinsic and radiative damping. This model has been used to simulate the Fano resonances induced in the Fanoshell structures and Cathodoluminescence spectroscopy results. No Fano resonance feature appeared under localized electron-beam excitation, but rather two independent noneigen modes appear, one associate with the central particle and the other with the outer ring of particles.

In chapter 4 we moved on from scattering properties of the plasmons in the nanoantennas to their absorption specifications and explained that the collective oscillations of the conduction electrons can decay into the electron-hole pair with the excitation energy equal to the energy of the plasmon resonance, which is called hot electrons. We used tunable Nanorods to harvest light photon and convert the resulting plasmonic energy into a hot electron-hole pair. Using a Schottky barrier to separate the electrons and holes we were able to generate current without the need for an applied bias voltage. The electrons only need to clear a barrier set up at the metal-silicon interface which has a barrier height of 0.5 eV. This was a proof that the plasmonics systems can be

used for photosensitization purposes. In addition of using Schottky barrier to harvest hot electron and produce an electric current, we reported photocatalytic dissociation of H2 molecules on the plasmonic structures using visible light at the room temperature. The hot electrons in their transient higher energy states can populate the antibonding orbital of H2 molecules adsorbed on the metal surfaces and thus trigger the H2 molecule dissociation. This method is a new pathway towards the application of low cost catalysts.

One of the applications of Plasmonics is the development of substrates capable of providing appropriate environment to do spectroscopy measurement for molecules. In chapter 5, we shared the same dream and take it to the next level. Using FDTD simulation we design suitable substrate for SEIRA measurement on the single molecule. High electric field enhancement required for SEIRA spectroscopy is induced by lightning rod effect. At long wavelengths, metals behave like perfect equipotential conductors and all the field be expelled from inside the metal in to the gap. This phenomenon assists us to achieve enhancement up to 100 in MIR range of spectrum that is independent of wavelength. In view of the fact that the SEIRA signal is proportional to the square of the electromagnetic field, we are able to increase our molecule signal up to10^4. We used analytic model for hemoglobin molecule to show that the SEIRA signals are coming from the molecules vibrational mode in the antenna's gap. This technique allows us to detect the vibrational mode of molecules such as hemoglobin in the real time and study their changes when the molecule is exposed to the Oxygen and Carbon dioxide as the hemoglobin is breathing in and out.

References

1. Ashcroft, N.W. and N.D. Mermin, *Solid State Physics*. 1976: Holt Rinehart and Winston, New York.
2. Ritchie, R.H., *Plasma Losses by Fast Electrons in Thin Films.* Physical Review, 1957. **106**(5): p. 874-881.
3. Powell, C.J. and J.B. Swan, *Origin of the Characteristic Electron Energy Losses in Aluminum.* Physical Review, 1959. **115**(4): p. 869-875.
4. Powell, C.J. and J.B. Swan, *Origin of the Characteristic Electron Energy Losses in Magnesium.* Physical Review, 1959. **116**(1): p. 81-83.
5. G. Mie, Ann. Phys, 1908. **25**(377).
6. Kreibig, U.V., M, *Optical Properties of metal clusters*. 1995: Springer Berlin.
7. Kelly, K.L., et al., J. Phys. Chem. B, 2002. **107**(3): p. 668.
8. Jain, P.K. and M.A. El-Sayed, Chem. Phys. Lett., 2010. **487**: p. 153.
9. Maier, S.A. and H.A. Atwater, *Plasmonics: Localization and guiding of electromagnetic energy in metal/dielectric structures.* Journal of Applied Physics, 2005. **98**(1): p. 011101-10.
10. Maier, S.A., *Plasmonics: Fundamentals and Applications*. 1 ed. 2007: (Springer, New York, NY.
11. Lee, S.J., et al., J. Phys. Chem. C, 2007. **111**(49): p. 17985.
12. Banholzer, M.J., et al., Chem. Soc. Rev., 2008. **37**(5): p. 885.
13. Le, F., et al., *Metallic Nanoparticle Arrays: A Common Substrate for Both Surface-Enhanced Raman Scattering and Surface-Enhanced Infrared Absorption.* ACS Nano, 2008. **2**(4): p. 707-718.
14. Nakayama, K., K. Tanabe, and H.A. Atwater, *Plasmonic nanoparticle enhanced light absorption in GaAs solar cells.* Applied Physics Letters, 2008. **93**(12): p. 121904-3.
15. Lal, S., S.E. Clare, and N.J. Halas, Acc. Chem. Res., 2008. **41**(12): p. 1842.
16. Lal, S., S. Link, and N.J. Halas, *Nano-optics from sensing to waveguiding.* Nat Photon, 2007. **1**(11): p. 641-648.
17. Mie, G., *Beiträge zur Optik trüber Medien, speziell kolloidaler Metallösungen.* Annalen der Physik, 1908. **330**(3): p. 377-445.
18. Sönnichsen, C., et al., *Drastic Reduction of Plasmon Damping in Gold Nanorods.* Physical Review Letters, 2002. **88**(7): p. 077402.
19. Aizpurua, J., et al., *Optical Properties of Gold Nanorings.* Physical Review Letters, 2003. **90**(5): p. 057401.
20. Hao, F., et al., *Shedding light on dark plasmons in gold nanorings.* Chemical Physics Letters, 2008. **458**(4–6): p. 262-266.
21. Wang, H., et al., Proc. Natl. Acad. Sci. U.S.A., 2006. **103**(29): p. 10856.
22. Pandian Senthil, K., et al., *High-yield synthesis and optical response of gold nanostars.* Nanotechnology, 2008. **19**(1): p. 015606.
23. Sherry, L.J., et al., *Localized Surface Plasmon Resonance Spectroscopy of Single Silver Nanocubes.* Nano Letters, 2005. **5**(10): p. 2034-2038.
24. Bergman, D.J. and M.I. Stockman, Phys. Rev. Lett., 2003. **90**(2): p. 027402.

25. Kokkinakis, T. and K. Alexopoulos, *Observation of Radiative Decay of Surface Plasmons in Small Silver Particles.* Physical Review Letters, 1972. **28**(25): p. 1632-1634.
26. Link, S. and M.A. El-Sayed, *Shape and size dependence of radiative, non-radiative and photothermal properties of gold nanocrystals.* International Reviews in Physical Chemistry, 2000. **19**(3): p. 409-453.
27. Meier, M. and A. Wokaun, *Enhanced fields on large metal particles: dynamic depolarization.* Opt. Lett., 1983. **8**(11): p. 581-583.
28. Hofmann, J. and W. Steinmann, *Plasma Resonance in the Photoemission of Silver.* physica status solidi (b), 1968. **30**(1): p. K53-K56.
29. Shalaev, V.M., et al., *Light-induced kinetic effects in solids.* Physical Review B, 1996. **53**(17): p. 11388-11402.
30. Redmond, P.L. and L.E. Brus, *"Hot Electron" Photo-Charging and Electrochemical Discharge Kinetics of Silver Nanocrystals.* The Journal of Physical Chemistry C, 2007. **111**(40): p. 14849-14854.
31. Brus, L., *Noble Metal Nanocrystals: Plasmon Electron Transfer Photochemistry and Single-Molecule Raman Spectroscopy.* Accounts of Chemical Research, 2008. **41**(12): p. 1742-1749.
32. Prodan, E., et al., Science, 2003. **302**: p. 419.
33. Hao, F., et al., *Enhanced tunability and linewidth sharpening of plasmon resonances in hybridized metallic ring/disk nanocavities.* Physical Review B, 2007. **76**(24): p. 245417.
34. Hao, F., et al., Nano Lett., 2008. **8**(11): p. 3983.
35. Enkrich, C., et al., *Magnetic Metamaterials at Telecommunication and Visible Frequencies.* Physical Review Letters, 2005. **95**(20): p. 203901.
36. Liu, N., et al., *Plasmon Hybridization in Stacked Cut-Wire Metamaterials.* Advanced Materials, 2007. **19**(21): p. 3628-3632.
37. Christ, A., et al., *Symmetry Breaking in a Plasmonic Metamaterial at Optical Wavelength.* Nano Letters, 2008. **8**(8): p. 2171-2175.
38. Liu, N., et al., *Plasmonic Building Blocks for Magnetic Molecules in Three-Dimensional Optical Metamaterials.* Advanced Materials, 2008. **20**(20): p. 3859-3865.
39. Shegai, T., et al., *Managing light polarization via plasmon–molecule interactions within an asymmetric metal nanoparticle trimer.* Proceedings of the National Academy of Sciences, 2008. **105**(43): p. 16448-16453.
40. Hao, F., et al., *Tunability of Subradiant Dipolar and Fano-Type Plasmon Resonances in Metallic Ring/Disk Cavities: Implications for Nanoscale Optical Sensing.* ACS Nano, 2009. **3**(3): p. 643-652.
41. Verellen, N., et al., *Fano Resonances in Individual Coherent Plasmonic Nanocavities.* Nano Letters, 2009. **9**(4): p. 1663-1667.
42. Pakizeh, T., et al., *Intrinsic Fano Interference of Localized Plasmons in Pd Nanoparticles.* Nano Letters, 2009. **9**(2): p. 882-886.
43. Li, Z., et al., *Multiple-Particle Nanoantennas for Enormous Enhancement and Polarization Control of Light Emission.* ACS Nano, 2009. **3**(3): p. 637-642.
44. Zhang, S., et al., Phys. Rev. Lett., 2008. **101**: p. 047401.

45. Liu, N., et al., Nat. Mater., 2009. **8**(9): p. 758.
46. Lassiter, J.B., et al., *Fano Resonances in Plasmonic Nanoclusters: Geometrical and Chemical Tunability.* Nano Letters, 2010. **10**(8): p. 3184-3189.
47. Lassiter, J.B., et al., *Designing and Deconstructing the Fano Lineshape in Plasmonic Nanoclusters.* Nano Letters, 2011.
48. Mukherjee, S., et al., *Fanoshells: Nanoparticles with Built-in Fano Resonances.* Nano Letters, 2010. **10**(7): p. 2694-2701.
49. Brown, L.V., et al., ACS Nano, 2010. **4**: p. 819.
50. Aeschlimann, M., M. Bauer, and S. Pawlik, *Competing nonradiative channels for hot electron induced surface photochemistry.* Chemical Physics, 1996. **205**(1–2): p. 127-141.
51. Knight, M.W., et al., *Photodetection with Active Optical Antennas.* Science, 2011. **332**(6030): p. 702-704.
52. Johansson, P., H. Xu, and M. Käll, *Surface-enhanced Raman scattering and fluorescence near metal nanoparticles.* Physical Review B, 2005. **72**(3): p. 035427.
53. Gibson, J.W. and B.R. Johnson, *Density-matrix calculation of surface-enhanced Raman scattering for p-mercaptoaniline on silver nanoshells.* The Journal of Chemical Physics, 2006. **124**(6): p. 064701-12.
54. Goude, Z.E. and P.T. Leung, *Surface enhanced Raman scattering from metallic nanoshells with nonlocal dielectric response.* Solid State Communications, 2007. **143**(8–9): p. 416-420.
55. Osawa, M., *Surface-Enhanced Infrared Absorption Near-Field Optics and Surface Plasmon Polaritons*, S. Kawata, Editor. 2001, Springer Berlin / Heidelberg. p. 163-187.
56. Jensen, T.R., et al., *Surface-Enhanced Infrared Spectroscopy: A Comparison of Metal Island Films with Discrete and Nondiscrete Surface Plasmons.* Applied Spectroscopy, 2000. **54**(3): p. 371-377.
57. Goutev, N. and M. Futamata, *Attenuated Total Reflection Surface-Enhanced Infrared Absorption Spectroscopy of Carboxyl Terminated Self-Assembled Monolayers on Gold.* Applied Spectroscopy, 2003. **57**(5): p. 506-513.
58. Carrasco, E.A., et al., *Study of the Interaction of Pollutant Nitro Polycyclic Aromatic Hydrocarbons with Different Metallic Surfaces by Surface-Enhanced Vibrational Spectroscopy (SERS and SEIR).* The Journal of Physical Chemistry A, 2003. **107**(45): p. 9611-9619.
59. Zheludev, N.I., et al., *Lasing spaser.* Nat Photon, 2008. **2**(6): p. 351-354.
60. Fedotov, V.A., et al., *Sharp Trapped-Mode Resonances in Planar Metamaterials with a Broken Structural Symmetry.* Physical Review Letters, 2007. **99**(14): p. 147401.
61. Brown, L.V., et al., *Heterodimers: Plasmonic Properties of Mismatched Nanoparticle Pairs.* ACS Nano, 2010. **4**(2): p. 819-832.
62. Sonnefraud, Y., et al., *Experimental Realization of Subradiant, Superradiant, and Fano Resonances in Ring/Disk Plasmonic Nanocavities.* ACS Nano, 2010. **4**(3): p. 1664-1670.

63. Alzar, C.L.G., M.A.G. Martinez, and P. Nussenzveig, Am. J. Phys, 2002. **70**(1): p. 37.
64. Shvets, G. and J.S. Wurtele, *Transparency of Magnetized Plasma at the Cyclotron Frequency.* Physical Review Letters, 2002. **89**(11): p. 115003.
65. Bardhan, R., et al., J. Phys. Chem. C, 2010. **114**(16): p. 7378.
66. Hu, Y., S.J. Noelck, and R.A. Drezek, ACS Nano, 2010. **4**: p. 1521.
67. Radloff, C. and N.J. Halas, Nano Lett., 2004. **4**: p. 1323.
68. Johnson, P.B. and R.W. Christy, Phys. Rev. B, 1972. **6**: p. 4370.
69. Knight, M.W., et al., Nano Lett., 2009. **9**(5): p. 2188.
70. Pena-Rodriguez, O. and U. Pal, J. Phys. Chem. C., 2010. **114**: p. 4414.
71. Chen, C.Y., et al., Opt. Express, 2009. **17**(17): p. 15372.
72. Chiam, S.Y., et al., Phys. Rev. B, 2009. **80**(15): p. 153103.
73. Noginov, M.A., et al., Nature, 2009. **460**(7259): p. 1110.
74. Fan, J.A., et al., Science, 2010. **328**(5982): p. 1135.
75. Mirin, N.A., K. Bao, and P. Nordlander, J. Phys. Chem. A, 2009. **113**(16): p. 4028.
76. Alonso-Gonzalez, P., et al., *Real-Space Mapping of Fano Interference in Plasmonic Metamolecules.* Nano Letters, 2011. **11**(9): p. 3922-3926.
77. Liu, N., et al., Nano Lett., 2010. **10**(4): p. 1103.
78. Jonsson, M.P., et al., Biointerphases, 2008. **3**(3): p. FD30.
79. Vo-Dinh, T., et al., J. Phys. Chem. C, 2010. **114**(16): p. 7480.
80. Mayer, K.N., et al., Nanotechnology, 2010. **21**: p. 255503.
81. El-Kashef, H., Physica B, 2000. **279**: p. 295.
82. Bao, K., H. Sobhani, and P. Nordlander, *Plasmon hybridization for real metals.* Chinese Science Bulletin, 2010. **55**: p. 2629-2634.
83. García de Abajo, F.J., *Optical excitations in electron microscopy.* Reviews of Modern Physics, 2010. **82**(1): p. 209-275.
84. Yamamoto, N., K. Araya, and F.J. García de Abajo, *Photon emission from silver particles induced by a high-energy electron beam.* Physical Review B, 2001. **64**(20): p. 205419.
85. Vesseur, E.J.R., et al., *Direct Observation of Plasmonic Modes in Au Nanowires Using High-Resolution Cathodoluminescence Spectroscopy.* Nano Letters, 2007. **7**(9): p. 2843-2846.
86. Kuttge, M., et al., *Local density of states, spectrum, and far-field interference of surface plasmon polaritons probed by cathodoluminescence.* Physical Review B, 2009. **79**(11): p. 113405.
87. Tian, Y. and T. Tatsuma, *Mechanisms and Applications of Plasmon-Induced Charge Separation at TiO2 Films Loaded with Gold Nanoparticles.* Journal of the American Chemical Society, 2005. **127**(20): p. 7632-7637.
88. O'Regan, B. and M. Gratzel, *A low-cost, high-efficiency solar cell based on dye-sensitized colloidal TiO2 films.* Nature, 1991. **353**(6346): p. 737-740.
89. Mühlschlegel, P., et al., *Resonant Optical Antennas.* Science, 2005. **308**(5728): p. 1607-1609.

90. Gobin, A.M., et al., *Near-Infrared Resonant Nanoshells for Combined Optical Imaging and Photothermal Cancer Therapy.* Nano Letters, 2007. **7**(7): p. 1929-1934.
91. Atwater, H.A. and A. Polman, *Plasmonics for improved photovoltaic devices.* Nat Mater, 2010. **9**(3): p. 205-213.
92. Ishi, T., et al., *Si nano-photodiode with a surface plasmon antenna.* Japanese Journal of Applied Physics Part 2-Letters & Express Letters, 2005. **44**(12-15): p. L364-L366.
93. Yu, N., et al., *Small-divergence semiconductor lasers by plasmonic collimation.* Nat Photon, 2008. **2**(9): p. 564-570.
94. Westphalen, M., et al., *Metal cluster enhanced organic solar cells.* Solar Energy Materials and Solar Cells, 2000. **61**(1): p. 97-105.
95. Tang, L., et al., *Nanometre-scale germanium photodetector enhanced by a near-infrared dipole antenna.* Nat Photon, 2008. **2**(4): p. 226-229.
96. Endriz, J.G. and W.E. Spicer, *Surface-Plasmon-One-Electron Decay and its Observation in Photoemission.* Physical Review Letters, 1970. **24**(2): p. 64-68.
97. Inagaki, T., K. Kagami, and E.T. Arakawa, *Photoacoustic observation of nonradiative decay of surface plasmons in silver.* Physical Review B, 1981. **24**(6): p. 3644-3646.
98. Inagaki, T., K. Kagami, and E.T. Arakawa, *PHOTO-ACOUSTIC STUDY OF SURFACE-PLASMONS IN METALS.* Applied Optics, 1982. **21**(5): p. 949-954.
99. Lehmann, J., et al., *Surface plasmon dynamics in silver nanoparticles studied by femtosecond time-resolved photoemission.* Physical Review Letters, 2000. **85**(14): p. 2921-2924.
100. Stuckless, J.T. and M. Moskovits, *Enhanced two-photon photoemission from coldly deposited silver films.* Physical Review B, 1989. **40**(14): p. 9997-9998.
101. Jin, R., et al., *Photoinduced Conversion of Silver Nanospheres to Nanoprisms.* Science, 2001. **294**(5548): p. 1901-1903.
102. Jin, R., et al., *Controlling anisotropic nanoparticle growth through plasmon excitation.* Nature, 2003. **425**(6957): p. 487-490.
103. Wu, X., et al., *Plasmon Induced Photovoltage and Charge Separation in Citrate-Stabilized Gold Nanoparticles.* The Journal of Physical Chemistry C, 2010. **114**(30): p. 12896-12899.
104. Scales, C. and P. Berini, *Thin-Film Schottky Barrier Photodetector Models.* Quantum Electronics, IEEE Journal of, 2010. **46**(5): p. 633-643.
105. Pérez-Juste, J., et al., *Gold nanorods: Synthesis, characterization and applications.* Coordination Chemistry Reviews, 2005. **249**(17–18): p. 1870-1901.
106. Fowler, R.H., *The analysis of photoelectric sensitivity curves for clean metals at various temperatures.* Physical Review, 1931. **38**(1): p. 45-56.
107. A.M, C., *Titanium-silicon Schottky barrier diodes.* Solid-State Electronics, 1970. **13**(4): p. 403-414.
108. Lisowski, M., et al., *Ultra-fast dynamics of electron thermalization, cooling and transport effects in Ru(001).* Applied Physics A: Materials Science & Processing, 2004. **78**(2): p. 165-176.

109. Bonn, M., et al., *Phonon- Versus Electron-Mediated Desorption and Oxidation of CO on Ru(0001).* Science, 1999. **285**(5430): p. 1042-1045.
110. Christian, F., *Ultrafast reaction dynamics of the associative hydrogen desorption from Ru(001).* Journal of Physics: Condensed Matter, 2008. **20**(31): p. 313002.
111. Watanabe, K., et al., *Photochemistry on Metal Nanoparticles.* Chemical Reviews, 2006. **106**(10): p. 4301-4320.
112. Gavnholt, J., et al., *Hot-electron-assisted femtochemistry at surfaces: A time-dependent density functional theory approach.* Physical Review B, 2009. **79**(19): p. 195405.
113. Gadzuk, J.W., *Resonance-Assisted Hot Electron Femtochemistry at Surfaces.* Physical Review Letters, 1996. **76**(22): p. 4234-4237.
114. Ertel, K., et al., *Time-resolved two-photon photoemission spectroscopy of HOPG and Ag nanoparticles on HOPG.* Applied Physics B: Lasers and Optics, 1999. **68**(3): p. 439-445.
115. Kundu, J., et al., *Surface enhanced infrared absorption (SEIRA) spectroscopy on nanoshell aggregate substrates.* Chemical Physics Letters, 2008. **452**(1–3): p. 115-119.